
Electronic Thesis and Dissertation Repository

8-8-2023 10:30 AM

Assessing the Sensitivity of Cerebral Blood Flow and Oxygenation to High Intracranial Pressure with Near-Infrared Light

Sule Karagulleoglu Kunduraci, *Western University*

Supervisor: Diop, Mamadou, *The University of Western Ontario*

A thesis submitted in partial fulfillment of the requirements for the Master of Science degree in Medical Biophysics

© Sule Karagulleoglu Kunduraci 2023

Follow this and additional works at: <https://ir.lib.uwo.ca/etd>



Part of the [Medical Biophysics Commons](#)

Recommended Citation

Karagulleoglu Kunduraci, Sule, "Assessing the Sensitivity of Cerebral Blood Flow and Oxygenation to High Intracranial Pressure with Near-Infrared Light" (2023). *Electronic Thesis and Dissertation Repository*. 9523.

<https://ir.lib.uwo.ca/etd/9523>

This Dissertation/Thesis is brought to you for free and open access by Scholarship@Western. It has been accepted for inclusion in Electronic Thesis and Dissertation Repository by an authorized administrator of Scholarship@Western. For more information, please contact wlsadmin@uwo.ca.

Abstract

Premature birth is associated with increased susceptibility to cerebral injuries because of the compounded effects of underdeveloped cerebral vascular and unstable hemodynamics. Notably, premature infants are highly vulnerable to intraventricular hemorrhage, which often leads to hydrocephalus and subsequently to high intracranial pressure (ICP). Current monitoring methods such as ultrasonography can only detect injuries that have already occurred, highlighting the need for prognostic tools. We hypothesize that concomitant measures of cerebral blood flow (CBF), blood oxygenation, and oxygen metabolism will be sensitive to high ICP. To test this hypothesis, experiments were conducted in a piglet model of high ICP using a noninvasive optical device that combines hyperspectral near-infrared spectroscopy and diffuse correlation spectroscopy. Measurements were acquired in nine piglets. Increases in ICP were associated with increases in deoxyhemoglobin and decreases in oxyhemoglobin, cerebral oxygenation, CBF, and cerebral perfusion pressure. These results demonstrated that optical measurements of CBF and cerebral oxygenation are sensitive to high ICP. The findings underscore the potential of optical techniques for non-invasive neuromonitoring in neonatal care, especially in the detection of compromised cerebral hemodynamics resulting from elevated ICP in cases of hydrocephalus.

Keywords

Optical neuromonitoring, Near-infrared spectroscopy, Diffuse correlation spectroscopy, Intraventricular hemorrhage, Hydrocephalus, High-intracranial pressure, Cerebral perfusion pressure, Cerebral blood flow, Cerebral oxygenation, Cerebral metabolism

Summary for Lay Audience

Premature neonates are highly susceptible to brain injuries because their brains are still in a critical developmental stage. Injuries such as bleeding in the cerebral ventricles can lead to hydrocephalus, which can adversely affect cerebral blood flow and metabolism. Hydrocephalus is an abnormal accumulation of cerebrospinal fluid in the brain that can cause high intracranial pressure (ICP; pressure inside the brain) and additional brain injuries. Current neuromonitoring techniques, such as ultrasonography, can only detect injuries that have already occurred. However, recent advances in biomedical optics have provided new tools that can non-invasively monitor the brain in real time.

In this study, we used a hybrid optical device that combines two optical techniques, near-infrared spectroscopy (NIRS) and diffuse correlation spectroscopy (DCS), to measure the effects of increased ICP on cerebral metabolism and blood flow in newborn piglets, to mimic what happens in neonates. This optical device can measure cerebral blood flow, deoxygenated hemoglobin (hemoglobin without oxygen), oxygenated hemoglobin (hemoglobin with oxygen), and cytochrome c oxidase (an enzyme involved in cellular energy production).

The measurements reveal that increases in ICP results in an increase in the concentration of deoxygenated hemoglobin and a decrease in the concentration of oxygenated hemoglobin, suggesting a reduction in the brain's oxygen supply. The patterns in these alterations correlated with changes in cerebral perfusion pressure, which controls the direction of blood flow to the brain. Additionally, the study showed that during ICP changes, there were strong relationships between changes in hemoglobin, oxygenation, cerebral blood flow, and cerebral perfusion pressure.

In conclusion, this study demonstrates that noninvasive optical measures of cerebral oxygenation and cerebral blood flow are sensitive to high intracranial pressure. This study additionally shows the noninvasive optical device can provide real-time detection of hemodynamic parameters that are involved in neonatal brain injury.

Co-Authorship Statement

The present study is an edited version of a proceeding paper entitled "Sensitivity of Cerebral Blood Flow and Oxygenation to High-Intracranial Pressure," which was published in the SPIE Proceedings Volume 12376-66, Optical Tomography and Spectroscopy of Tissue XV. This proceeding article was presented at the SPIE Photonic West conference in 2023 by Sule Karagulleoglu-Kunduraci and Mamadou Diop. Sule Karagulleoglu-Kunduraci was the first author and the speaker at the conference for this published proceeding, and the remaining co-author is Mamadou Diop. A version of this study was presented as a poster with same title at the Imaging Network Ontario conference and as a presentation in the London Imaging Discover Day conference in 2023. This published proceeding and poster featured preliminary findings of the study.

Sule Karagulleoglu-Kunduraci undertook the tasks of data collection, data analysis, and manuscript drafting. Mamadou Diop adapted and re-built the hybrid CW *h*-NIRS/DCS system and provided the NIRS and DCS data analysis codes. The animal surgery necessary to conduct the animal experiments was performed by Jane Sykes and Hannah Jago. Mamadou Diop offered guidance and oversight throughout the entire process of the study, from its inception to its completion. Additionally, Mamadou Diop secured funding for all aspects of the project, took charge of developing the study concept, designing the study, interpreting the data, and editing the manuscript. Co-author, Mamadou Diop reviewed, edited, and approved the manuscript.

Acknowledgments

I would like to begin by expressing my gratitude to my supervisor, Dr. Mamadou Diop, for his endless support, mentorship, patience and understanding since my arrival in Canada. Foremost, I would like to thank him for persistently maintaining faith in my abilities, even when I experienced a loss of self-confidence throughout the entirety of this study. Additionally, I am thankful his constructive encouragement, which played a pivotal role in facilitating the successful completion of this study. I also thank him for always being open to conversation and discussion, for guiding me from the beginning to the end of this study.

I would like to thank my advisory committee, Dr. Charles McKenzie and Dr. Sandrine de Ribaupierre, for their guidance and valuable suggestions throughout my work. I would like to acknowledge and thank Jane Sykes, Hannah Jago, Laura Morrison, Lise Desjardins and Jennifer Hadway for their invaluable help with the animal experiments.

Upon my arrival in Canada, I found myself devoid of any acquaintances or social connections. Thank you to my lab-mates (friends) for helping me get used to and adapt to Canada, London and Western University, for checking my presentations without getting tired and giving suggestions that allow me to get better. I also thank them for our shopping trips, our Halloween and Christmas celebrations, where we can have fun together, watching reality shows together, our chat-filled lunches, and being there for me whenever I need advice on anything.

I would like to special thank my lovely husband for his endless love, patience, and support during this process, for not leaving me alone in my academic journey, for comforting me whenever I felt under stress during this study, for listening to all my presentations without getting tired. I would like to thank my dear parents for always encouraging me to learn and develop as a child, and for their endless support even from miles away.

Prior to concluding, I would like to express my gratitude by initiating a substantial digression. In 1929, Mustafa Kemal Atatürk, the esteemed founder of the Republic of Turkey, enacted legislation pertaining to the provision of scholarships for Turkish students to pursue postgraduate education in foreign countries. I came to Canada by awarded the scholarship program initiated by this law, which was enacted many years ago, and completed this study.

For this reason, I would like to respectfully commemorate my great mentor, Mustafa Kemal Atatürk, who supported my education even in his absence with this vision he envisioned.

Finally, this study was funded by Western University, Schulich School of Medicine and Dentistry, and the Department of Medical Biophysics, Lawson Health Research Institute, and the Natural Sciences and Engineering Research Council of Canada (NSERC), Canadian Institutes of Health Research (CIHR). I am also supported by a scholarship of the Republic of Turkey Ministry of National Education.

Table of Contents

Abstract.....	ii
Summary for Lay Audience.....	iii
Co-Authorship Statement.....	iv
Acknowledgments.....	v
Table of Contents.....	vii
List of Tables.....	ix
List of Figures.....	x
List of Appendices.....	xii
List of Abbreviations.....	xv
Chapter 1.....	1
1 Introduction.....	1
1.1 Prevalence of Preterm Brain Injury.....	1
1.2 Intraventricular Hemorrhage.....	2
1.3 Post-Hemorrhagic Hydrocephalus.....	4
1.4 High Intracranial Pressure.....	4
1.5 Physiology of Brain Injuries in Preterm Infants.....	5
1.5.1 Cerebral Perfusion Pressure.....	5
1.5.2 Cerebral Oxygenation and Cerebral Blood Flow.....	6
1.6 Monitoring of Post-Hemorrhagic Hydrocephalus.....	7
1.7 Near-Infrared Spectroscopy (NIRS).....	10
<i>Principles of NIRS</i>	12
1.8 Measuring Cerebral Blood Flow with NIR light.....	14
<i>Principles of DCS</i>	15
1.9 Hybrid Optical Instruments.....	17

1.10	Research Objective	19
1.11	References	20
Chapter 2		28
2	Assessing the Sensitivity of Cerebral Blood Flow and Oxygenation to High Intracranial Pressure with Near-Infrared Light	28
2.1	Introduction	28
2.2	Methods	31
2.2.1	Instrumentation	31
2.2.2	Animal Model	33
2.2.3	Data Processing	36
2.3	Results	40
2.4	Discussion	51
2.5	References	59
Chapter 3		64
3	Conclusions	64
3.1	Research Objectives	64
3.2	Summary of Chapter 2: Assessing the Sensitivity of Cerebral Blood Flow and Oxygenation to High Intracranial Pressure with Near-Infrared Light	66
3.3	Limitations and Future Directions	67
3.4	Conclusion	69
3.5	References	71
Appendices		73
Curriculum Vitae		84

List of Tables

Table 1: Demographic and Group Assignment (Neonatal Piglets)	40
Table 2: Baseline values for all parameters	44
Table 3: Results of the linear regression and Pearson correlation for mean changes in CBF and CPP are presented. Linear regression: $y = ax + b$, a is mean slopes across all the runs in one piglet, b is mean intercepts and R^2 (R-squared) is the coefficient of determination. " r " represents the Pearson correlation coefficient.	50

List of Figures

Figure 1: Severe intraventricular hemorrhage. Cranial ultrasounds at postnatal ages (a) 1 day, and (b) 4 days from a 28-week gestation neonate with grade IV-IVH (In panels a and b, white arrows sign the IVH in the GM, it is filling and distending the right lateral ventricle, respectively.)¹⁵. 3

Figure 2: Absorption spectra of both water (blue), oxygenated hemoglobin (red), deoxygenated hemoglobin (orange), and cytochrome-c-oxidase (oxCCO) (green) in the near infrared (NIR) range (650-900nm)..... 10

Figure 3: (a) Schematic of the hybrid CW *h*-NIRS/DCS system and (b) 3D-probe holder’s geometry. In panel (a), the red lines represent the CW *h*-NIRS signal path, the black lines represent the path of the DCS signal, the black dotted line represent the light propagation prior shutter, and the black dashed lines represent the electronic connections of the CW *h*-NIRS and DCS to the laptop computer. In panel (b), the “S” denotes the source probes, and the “D” denotes the detection probes. 33

Figure 4: Schematic of the experimental setup for the neonatal piglet, showing the placement of the hybrid CW *h*-NIRS/DCS probes and locations of the ICP catheter and the saline infusion in the ventricles. (a) Illustration of a piglet in prone position. (b) A closed-up drawing of the placement of optical probes and catheters on the piglet’s head. (Image adapted from ³⁸) 35

Figure 5: Average changes in tissue chromophores and blood flow without ICP changes for all piglets in the control group ($n=2$, *Control Group: C1-C2*) and the experimental group ($n=7$, *Experimental Group: E1-E7*). The blue lines represent changes in HbO₂ concentrations, the red lines represent changes in Hb concentrations, the green lines represent changes in oxCCO and the orange lines represent percentage changes in CBFi. The solid lines are the mean across the group and the shaded areas represent standard derivations. Note that all concentrations are expressed in μM 41

Figure 6: (A) Time dependent changes in ΔHb , ΔHbO_2 and ΔoxCCO with ΔICP from one piglet in the experimental group (E1) for the two runs. The orange lines represent ΔHbO_2 , the blue lines represent ΔHb , the green lines represent ΔoxCCO in μM , and the dark red lines

represent ΔICP in mmHg. In panel (A), the grey box illustrates the baseline ICP period, the yellow box illustrates the increased ICP period, and the green box illustrates the decreased ICP period. (B) and (C) Time-dependent changes in ΔCBF_i and StO_2 with changes in CPP (ΔCPP) from same piglet (E1) for two runs in (%), respectively. 42

Figure 7: Correlation plots of (a) ΔHb versus ΔCPP , (b) ΔHbO_2 versus ΔCPP , (c) changes in StO_2 versus ΔCPP , (d) ΔCBF_i versus ΔCPP for one piglet (E1) for three runs. The dashed lines represent the best fit of regression line, the solid green lines represent mean fitted linear line for first and second run ($p < 0.05$, $R^2 > 0.91 \pm 0.04$). 45

Figure 8: Correlation plots of (a) ΔHb versus ΔCPP , (b) ΔHbO_2 versus ΔCPP , (c) Changes in StO_2 versus ΔCPP , (d) ΔCBF_i versus ΔCPP for one piglet (E3) for three runs. The filled scatter dots represent the clusters' data points for the delayed response for HbO_2 and StO_2 . The dashed lines represent the regression line, the solid green lines represent mean of the fitted linear lines for all there runs ($p < 0.001$, $R^2 > 0.9 \pm 0.01$). 46

Figure 9: Correlation plot of the relationship between changes in mean CBF and CPP changes during ICP alterations for all piglets in the experimental group (Experimental group: E1, E2, E3, E4, E5, E6 and E7). The dashed lines represent the results of linear regression. 49

List of Appendices

Appendix A: (A) Time dependent changes in ΔHb , ΔHbO_2 and ΔoxCCO with ΔICP from second piglet in the experimental group (E2) for the two runs. The orange lines represent ΔHbO_2 , the blue lines represent ΔHb , the green lines represent ΔoxCCO in μM , and the dark red lines represent ΔICP in mmHg. In panel (A), the grey box illustrates the baseline ICP period, the yellow box illustrates the increased ICP period, and the green box illustrates the decreased ICP period. (B) and (C) Time-dependent changes in ΔCBFi and StO_2 with changes in CPP (ΔCPP) from same piglet (E2) for two runs in (%), respectively. 73

Appendix B: (A) Time dependent changes in ΔHb , ΔHbO_2 and ΔoxCCO with ΔICP from third piglet in the experimental group (E3) for the three runs. The orange lines represent ΔHbO_2 , the blue lines represent ΔHb , the green lines represent ΔoxCCO in μM , and the dark red lines represent ΔICP in mmHg. In panel (A), the grey box illustrates the baseline ICP period, the yellow box illustrates the increased ICP period, and the green box illustrates the decreased ICP period. (B) and (C) Time-dependent changes in ΔCBFi and StO_2 with changes in CPP (ΔCPP) from same piglet (E3) for three runs in (%), respectively. 74

Appendix C: (A) Time dependent changes in ΔHb , ΔHbO_2 and ΔoxCCO with ΔICP from fourth piglet in the experimental group (E4) for the three runs. The orange lines represent ΔHbO_2 , the blue lines represent ΔHb , the green lines represent ΔoxCCO in μM , and the dark red lines represent ΔICP in mmHg. In panel (A), the grey box illustrates the baseline ICP period, the yellow box illustrates the increased ICP period, and the green box illustrates the decreased ICP period. (B) and (C) Time-dependent changes in ΔCBFi and StO_2 with changes in CPP (ΔCPP) from same piglet (E4) for three runs in (%), respectively. 75

Appendix D: (A) Time dependent changes in ΔHb , ΔHbO_2 and ΔoxCCO with ΔICP from fifth piglet in the experimental group (E5) for the two runs. The orange lines represent ΔHbO_2 , the blue lines represent ΔHb , the green lines represent ΔoxCCO in μM , and the dark red lines represent ΔICP in mmHg. In panel (A), the grey box illustrates the baseline ICP period, the yellow box illustrates the increased ICP period, and the green box illustrates the decreased ICP period. (B) and (C) Time-dependent changes in ΔCBFi and StO_2 with changes in CPP (ΔCPP) from same piglet (E5) for two runs in (%), respectively. 76

Appendix E: (A) Time dependent changes in ΔHb , ΔHbO_2 and ΔoxCCO with ΔICP from sixth piglet in the experimental group (E6) for the two runs. The orange lines represent ΔHbO_2 , the blue lines represent ΔHb , the green lines represent ΔoxCCO in μM , and the dark red lines represent ΔICP in mmHg. In panel (A), the grey box illustrates the baseline ICP period, the yellow box illustrates the increased ICP period, and the green box illustrates the decreased ICP period. (B) and (C) Time-dependent changes in ΔCBFi and StO_2 with changes in CPP (ΔCPP) from same piglet (E6) for two runs in (%), respectively. 77

Appendix F: (A) Time dependent changes in ΔHb , ΔHbO_2 and ΔoxCCO with ΔICP from seventh piglet in the experimental group (E7) for the two runs. The orange lines represent ΔHbO_2 , the blue lines represent ΔHb , the green lines represent ΔoxCCO in μM , and the dark red lines represent ΔICP in mmHg. In panel (A), the grey box illustrates the baseline ICP period, the yellow box illustrates the increased ICP period, and the green box illustrates the decreased ICP period. (B) and (C) Time-dependent changes in ΔCBFi and StO_2 with changes in CPP (ΔCPP) from same piglet (E7) for two runs in (%), respectively. 78

Appendix G: Correlation plots of (a) ΔHb vs ΔCPP , (b) ΔHbO_2 vs ΔCPP , (c) StO_2 vs ΔCPP , (d) ΔCBFi vs ΔCPP for second piglet (E2) mean values for all runs; indicates significant correlations for ΔHb and ΔCBFi and significant correlations with delaying for ΔHbO_2 and StO_2 . The filled scatter dots represent the delaying clusters' data points. The dashed lines represent the regression line, the solid green lines represent mean fitted linear line for all runs (**$p < 0.05$, $R^2 > 0.90 \pm 0.06$**). 79

Appendix H: Correlation plots of (a) ΔHb vs ΔCPP , (b) ΔHbO_2 vs ΔCPP , (c) StO_2 vs ΔCPP , (d) ΔCBFi vs ΔCPP for fourth piglet (E4) mean values for all runs; indicates significant correlations for ΔHb and ΔCBFi and significant correlations with delaying for ΔHbO_2 and StO_2 . The filled scatter dots represent the delaying clusters' data points. The dashed lines represent the regression line, the solid green lines represent mean fitted linear line for all runs (**$p < 0.05$, $R^2 > 0.85 \pm 0.09$**). 80

Appendix I: Correlation plots of (a) ΔHb vs ΔCPP , (b) ΔHbO_2 vs ΔCPP , (c) ΔStO_2 vs ΔCPP , (d) ΔCBFi vs ΔCPP for fifth piglet (E5) mean values for all runs; indicates significant correlations for ΔHb and ΔCBFi and significant correlations with delaying for ΔHbO_2 and StO_2 . The filled scatter dots represent the delaying clusters' data points. The dashed lines

represent the regression line, the solid green lines represent mean fitted linear line for all runs ($p < 0.05$, $R^2 > 0.87 \pm 0.09$). 81

Appendix J: Correlation plots of ΔHb vs ΔCPP , ΔHbO_2 vs ΔCPP , StO_2 vs ΔCPP , $\Delta CBFi$ vs ΔCPP for seventh piglet (E6) mean values for all runs: ΔHb vs ΔCPP , ΔHbO_2 vs ΔCPP , StO_2 vs ΔCPP , $\Delta CBFi$ vs ΔCPP for sixth piglet (E6) mean value for all runs. The dashed lines represent the best fit of regression line, the solid green lines represent mean fitted linear line for all runs ($p < 0.05$, $R^2 > 0.88 \pm 0.02$). 82

Appendix K: Correlation plots of ΔHb vs ΔCPP , ΔHbO_2 vs ΔCPP , StO_2 vs ΔCPP , $\Delta CBFi$ vs ΔCPP for seventh piglet (E7) mean values for all runs; indicates significant correlations for ΔHb , StO_2 and $\Delta CBFi$, and significant correlations with delaying for ΔHbO_2 . The filled scatter dots represent the delaying clusters' data points. The dashed lines represent the regression line, the solid green lines represent mean fitted linear line for all runs ($p < 0.05$, $R^2 > 0.90 \pm 0.02$). 83

List of Abbreviations

ABP	Arterial blood pressure
ANOVA	Analysis of variance
ANCOVA	Analysis of covariance
BFi	Blood flow index
CBF	Cerebral blood flow
CBFi	Cerebral blood flow index
CCO	Cytochrome c oxidase
CMRO ₂	Cerebral metabolic rate of oxygen
CPP	Cerebral perfusion pressure
CSF	Cerebrospinal fluid
CT	Computed tomography
cUS	Cranial ultrasonography
CW	Continuous wave
DCS	Diffuse correlation spectroscopy
DCE	Dynamic contrast enhanced
DOS	Diffuse optical spectroscopy
DPF	Differential pathlength factor
FD	Frequency-domain
GA	Gestational age
GM	Germinal matrix

Hb	Deoxyhemoglobin
HbO ₂	Oxyhemoglobin
h-NIRS	Hyperspectral near-infrared spectroscopy
ICG	Indocyanine green
ICP	Intracranial pressure
IVH	Intraventricular hemorrhage
MAP	Mean arterial pressure
MRI	Magnetic resonance imaging
NICU	Neonatal intensive care unit
NIR	Near infrared
NIRS	Near infrared spectroscopy
oxCCO	Oxidation state of cytochrome c oxidase
PET	Positron emission tomography
PHH	Post-hemorrhagic hydrocephalus
SDD	Source-detector distance
StO ₂	Tissue oxygen saturation
TCD	Transcranial doppler
tHb	Total hemoglobin
TR	Time-resolved
VLBW	Very low birth weight

WF

Water fraction

Chapter 1

1 Introduction

This chapter explains the motivation for this work presented in the thesis and also provides background on brain injury in preterm infants such as intraventricular hemorrhage, the causes of these injuries, and one of their consequences—hydrocephalus, the monitoring of hydrocephalus, and an overview of the theory and technology of the optical techniques used in the thesis for neonatal neuromonitoring.

1.1 Prevalence of Preterm Brain Injury

Based on the United Nations, the global annual birth rate stands at around 140 million, with an estimated 15 million of these births classified as premature¹. Preterm infants have a heightened risk of acute and chronic brain injury. The highest risk of encephalopathy occurs between 23 and 32 weeks of gestational age (GA)². Studies indicate that roughly 21% of preterm infants born before 37 weeks GA have abnormal brain images, such as intraventricular hemorrhage (IVH) or parenchymal lesions, as detected by cranial ultrasound³. Such abnormalities are associated with long-term consequences, including cognitive and behavioral deficits, cerebral palsy, and hydrocephalus^{4,5}.

Hydrocephalus involves the abnormal buildup of fluid in the brain, leading to increased pressure within the ventricles. This pressure can result in brain injuries, which might further contribute to conditions like cerebral palsy⁶. Despite advancements in healthcare improving survival rates for preterm infants with brain injuries, many of these infants grapple with neurodevelopmental disabilities. This situation presents not only emotional challenges but also imposes a heavy financial strain on families. Direct costs include frequent medical visits, equipment, therapies, medications, and surgeries. Indirect costs, such as lost income from caregiving duties or home modifications, further heighten the financial strain. Beyond individual families, the broader healthcare system is also heavily

impacted by the economic implications of treating and supporting infants with neurodevelopmental disabilities.

In Canada, associated conditions such as hydrocephalus, cerebral palsy, and other disabilities impose a significant financial burden on the healthcare system. It's estimated that these conditions cost more than \$8 billion annually, covering expenses like hospitalizations, outpatient visits, medications, therapies, assistive devices, and support services⁷. The total also encapsulates long-term costs for educational support, rehabilitation, social services, and community resources required for individuals with neurodevelopmental disabilities.

In summary, preterm brain injury has broad implications, affecting many infants and exerting a considerable toll on families, society, and the healthcare system globally. The associated costs to the healthcare system, including direct medical expenses, highlight the need for continued research and improved monitoring techniques to mitigate the long-term consequences of preterm brain injury on both individuals and society.

1.2 Intraventricular Hemorrhage

Premature infants with extremely low birth weights face an elevated risk of experiencing intraventricular hemorrhage (IVH) primarily due to the inherent hemodynamic instabilities and impaired cerebral autoregulation observed in their brains⁸. Globally, IVH occurs in 20 to 40% of infants with a birth weight less than 1500 grams, qualifying as very low birth weight (VLBW)⁹. Although the occurrence of IVH in VLBW infants declined from around 40 to 50% in the early 1980s to about 20% in the late 1980s¹⁰, it has since stabilized at an estimated 15%¹¹. Thus, IVH continues to be a significant concern for neonatal intensive care units (NICUs) worldwide.

The primary cause of neonatal IVH is the delicate blood vessels within the germinal matrix (GM) interacting with swift hemodynamic fluctuations. The GM, being highly vascularized and metabolically active, is responsible for the proliferation of future neuronal and glial cells. This periventricular zone exhibits selective susceptibility to hemorrhage in

neonates born prematurely, predominantly within the initial 48-hour lifespan. In the event of severe hemorrhage in the GM, blood can inundate the cerebral ventricle¹¹. In preterm infants, more than 90% of IVH usually develop within 72 hours after birth, with cardiovascular instability playing a significant role, especially during the intrauterine to extrauterine transition¹². Papile et al. established a classification system consisting of four grades to categorize IVH based on the severity and anatomical location of the hemorrhage, employing computed tomography (CT) scans for assessment purposes¹³. In accordance with the classification proposed by Papile et al., IVH confined to the GM is categorized as grade I. Grade II refers to the occurrence of hemorrhage extending into the lateral ventricles, without the simultaneous enlargement of the ventricles. Grade III is assigned to ventricular hemorrhage in isolation, while grade IV is specifically designated for parenchymal hemorrhage¹⁴.

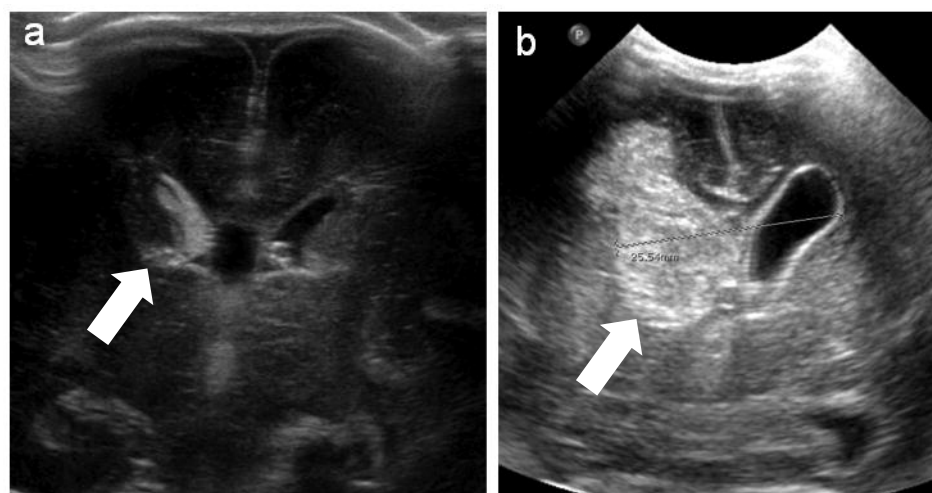


Figure 1: Severe intraventricular hemorrhage. Cranial ultrasounds at postnatal ages (a) 1 day, and (b) 4 days from a 28-week gestation neonate with grade IV-IVH (In panels a and b, white arrows sign the IVH in the GM, it is filling and distending the right lateral ventricle, respectively.)¹⁵.

IVH triggers an inflammatory response obstructing cerebral spinal fluid (CSF) drainage¹⁶. This leads to increased intracranial pressure (ICP) and can result in post-hemorrhagic

hydrocephalus (PHH), a condition where CSF accumulates abnormally within the brain¹⁷. Premature infants with grade III-IV IVH are especially prone to developing PHH, which further increases the risks of complications like cerebral palsy and hydrocephalus^{11,18}.

1.3 Post-Hemorrhagic Hydrocephalus

Hydrocephalus arises from the abnormal accumulation of CSF within the brain's ventricles. These ventricles are cavities that circulate and cushion both the brain and spinal cord. When there's a disruption in CSF flow or absorption, it results in fluid buildup, leading to enlarged ventricles that exert pressure on adjacent brain tissue¹⁹. There are multiple causes of hydrocephalus, with IVH and infections, such as meningitis, being significant contributors. Infection-triggered inflammatory processes can block CSF pathways and impair structures vital for its absorption²⁰. One form of hydrocephalus caused by IVH is known as post-hemorrhagic hydrocephalus (PHH). This occurs when bleeding within the ventricles disrupts the normal flow of CSF and hinders its absorption, leading to the accumulation of fluid²¹. PHH is a common neuropathological condition in pediatric neurosurgery, often resulting in compromised cognitive outcomes^{22,23}. The resultant cognitive deficits can be attributed to damages like periventricular white matter injury and hypoxic-ischemic brain tissue damage, stemming from elevated ICP²⁴.

1.4 High Intracranial Pressure

Effective management of PHH pivots on controlling ICP. As CSF pathways are obstructed, ICP rises, compressing the brain tissue near the ventricles and affecting cerebral metabolism²⁵ by disrupting cerebral blood flow (CBF)²⁶. This increased ICP not only risks brain damage but also diminishes cerebral perfusion pressure (CPP)²⁷ by narrowing the pressure gradient between arterial blood pressure and ICP²⁸. Given its paramount importance, understanding the cerebral hemodynamic response to heightened ICP needs more exploration.

Given the impact of high ICP on critical brain parameters such as cerebral oxygenation, CPP, and CBF, it is essential to explore these parameters that govern premature infant brain injuries. The delicate nature of a premature infant's brain renders it uniquely vulnerable to various forms of injury, which in turn significantly affects cerebral physiology. Understanding the intricacies of cerebral oxygenation, CPP, and CBF is crucial for comprehending the pathophysiology of brain injuries in premature infants.

1.5 Physiology of Brain Injuries in Preterm Infants

The delicate nature of a premature infant's brain makes it uniquely susceptible to various forms of injury, significantly affecting cerebral physiology. This physiology, which is crucial to understanding the pathophysiology of premature infant brain injuries, encompasses several components including cerebral perfusion pressure, cerebral oxygenation, and cerebral blood flow.

1.5.1 Cerebral Perfusion Pressure

Cerebral perfusion pressure (CPP) refers to the overall pressure difference that facilitates the delivery of oxygen to the cerebral tissue. It is determined by subtracting the ICP from the mean arterial pressure (MAP), measured in millimeters of mercury (mmHg). Sustaining an optimal CPP is of utmost importance in the management of individuals with intracranial conditions, such as traumatic brain injury and PHH²⁸. CPP is a critical determinant of brain tissue perfusion and oxygenation, making it central to the maintenance of brain homeostasis. Abnormalities in CPP, which typically ranges between 60 and 80 mmHg, can result in significant brain injury. Under normal circumstances, the ICP ranges between 5 and 10 mmHg²⁸, therefore exerting less influence on CPP compared to MAP, which usually lies between 70 to 110 mmHg, in normal clinical scenarios. Direct measurement of ICP is typically performed through intracranial pressure transduction. From a physiological perspective, ICP is governed by intracranial compliance, which represents the relationship between volume within the intracranial compartment, including CSF, brain tissue, and

arterial and venous blood volumes, and the corresponding ICP levels. Given the fixed and unyielding nature of the cranial cavity, an augmentation in intracranial volume and a decline in intracranial compliance will trigger an increase in ICP²⁸. According to recent studies, the cerebrovascular response to a prolonged reduction in cerebral perfusion pressure resulting from a decrease in mean arterial pressure or an elevation in intracranial pressure exhibits significant physiological distinctions. In a study conducted by Bragin et al., the cerebral hemodynamic response to sustained decrements of CPP was measured. The study involved a duration of 30 minutes at each level of ICP^{29,30}. The findings revealed that when ICP increased, leading to a decrease in CPP, the threshold for autoregulation was observed to be around 30 mmHg for CPP. Conversely, when the decrease in CPP was induced by a decrease in MAP, the lower limit of autoregulation was approximately 50mmHg²⁶.

1.5.2 Cerebral Oxygenation and Cerebral Blood Flow

Cerebral metabolism and oxygenation play vital roles in sustaining brain function and development in premature infants. Disruptions in metabolic processes and oxygen supply can lead to adverse neurological outcomes. While various factors contribute to brain injury during the perinatal period, disturbances in CBF are thought to be of considerable significance. The cerebral vascular system, which is not fully developed in premature infants, along with several complications related to premature birth, including impaired cardiac and pulmonary function, can impede the circulation of blood and the delivery of oxygen. These factors contribute to the development of injuries in the neonatal brain. Moreover, it is plausible that alterations in brain tissue metabolism may manifest prior to the emergence of structural abnormalities associated with the injury⁸. Changes in CBF can therefore substantially impact a premature infant's brain health and developmental trajectory.

As mentioned above, IVH triggers an inflammatory reaction, which subsequently initiates fibrosis and obstructs the drainage of CSF⁸. The presence of this obstruction has the potential to cause the buildup of CSF, leading to an increase in ICP and the initiation of

PHH. The increase in ICP associated with PHH can perturb cerebral hemodynamics and metabolism. Elevated ICP may lead to changes in CBF dynamics within the brain, potentially impacting cerebral perfusion and oxygenation. These alterations in cerebral hemodynamics and metabolism underscore the critical importance of monitoring and managing ICP in the context of IVH and PHH to mitigate the potential detrimental effects on brain health.

1.6 Monitoring of Post-Hemorrhagic Hydrocephalus

Effective management of PHH is crucial for minimizing potential complications and optimizing outcomes in affected individuals. Management of premature infants with PHH begins with the critical step of monitoring development of PHH in the vulnerable preterm brain³¹. This initial monitoring sets the foundation for ongoing management, which primarily revolves around temporary measures aimed at reducing ICP³². This monitoring allows for the early identification of potential complications, such as progressive ventricular dilation or elevated ICP, and facilitates the implementation of appropriate interventions. Regular monitoring of hydrocephalus also provides valuable data for clinicians to evaluate the response to treatment, track disease progression, and optimize long-term management plans³³. Thus, the meticulous monitoring of IVH and PHH serves as a critical cornerstone in the comprehensive management approach for premature infants, enabling timely interventions, minimizing the risk of complications, and ultimately improving outcomes for this vulnerable population.

In the realm of hydrocephalus monitoring and diagnosing, various devices and imaging systems such as cranial ultrasonography (cUS)³⁴, computed tomography (CT)³⁵, and magnetic resonance imaging (MRI)³⁵ offer valuable insights into ventricular size, CSF dynamics, and potential complications.

Cranial Ultrasonography

For diagnosing cerebral lesions in preterm infants, cranial ultrasonography (cUS) is the most widely available and routinely utilized imaging technique¹⁶. Of all the various forms

of cerebral hemorrhages, IVH stands out as the most commonly occurring and readily identifiable pathology observed through cUS in preterm infants. Its incidence remains consistently high over time. In preterm infants, IVH is frequently detected within the initial days after birth, with approximately 50% of cases identified on the first day and 90% within the first four days⁹. Around a quarter to half of individuals affected by IVH show no clinical symptoms, and the condition is detected through routine screening cUS. Ultrasonography has demonstrated significant utility in the consecutive evaluation of ventricular dilation in cases involving IVHs or surgical interventions, despite its limited level of detail and resolution which typically render it unsuitable for primary diagnostic purposes^{19,36}.

Ultrasound imaging is an invaluable modality utilized for the diagnosis and monitoring of cerebral injury in preterm infants, however, it is not without significant limitations. Initially, it should be noted that cUS is limited in its ability to offer uninterrupted observation of cerebral activity, as it solely captures a solitary momentary representation of its state. Furthermore, the structural damage observed by cUS represents brain injury that has already occurred, limiting its ability to provide real-time insights into ongoing changes or predict future complications. Therefore, while cUS serves as an important initial screening modality, additional imaging techniques are often necessary to complement the information obtained from ultrasound to offer a more comprehensive understanding of the evolving pathophysiology of brain injuries in preterm infants.

Computed Tomography and Magnetic Resonance Imaging

Both magnetic resonance imaging (MRI) and computed tomography (CT) can produce high-resolution images, which enable precise visualization for the purpose of accurately diagnosing brain injury in preterm infants. However, similar to ultrasound, these imaging techniques have their limitations. MRI scans are costly, and MRI and CT typically require the transfer of the infant to the radiology department, making them less accessible³⁷. On the other hand, CT uses X-ray radiation to create detailed images of the body. However, it is important to be cautious of the harmful effects of X-ray radiation exposure, such as the induction of cancer. In the United States, it is estimated that 1.5-2.0% of all cancers are attributable to radiation from CT scans³⁸. Additionally, the timing of imaging is crucial, as

any identified damage is often irreversible at the point of imaging. Therefore, clinical decision-making focuses on managing the existing injury and implementing measures to prevent further damage. Notwithstanding these constraints, MRI and CT hold crucial significance in the thorough evaluation of brain injury in premature infants, allowing for accurate diagnosis and guiding the implementation of suitable treatment approaches²⁰.

Other Neuromonitoring Techniques

Recent research has focused on investigating physiological precursors of brain injury in preterm infants, with particular attention given to measuring CBF as a potential marker of damage. Over the years, a variety of approaches and technologies have been employed to assess CBF, reflecting the evolving understanding of its role in brain injury. In 1983, Volpe et al. conducted an initial study utilizing positron emission tomography (PET) and oxygen-15 labelled water as a radiotracer to evaluate CBF in preterm infants diagnosed with IVH³⁹. However, the most important limitation was using radiation in PET. Since then, further studies have utilized various imaging techniques, including transcranial Doppler ultrasound (TCD)^{37,40}, to explore CBF alterations associated with different types of brain injury in preterm infants. While continuous monitoring of CBF via TCD is feasible, the substantial equipment size and the necessity of placing the transducer in immediate proximity to the region of interest render this approach unwieldy and impracticable for longitudinal assessments. Monitoring cerebral metabolism in conjunction with CBF can provide a more holistic understanding of the physiological state of the brain and help identify potential injury or pathological processes that may require intervention⁴¹. Methods available for monitoring cerebral metabolism in newborns are relatively limited, particularly when considering techniques that involve radiation exposure. This highlights the need for prognostic techniques to identify indicators of brain injury.

1.7 Near-Infrared Spectroscopy (NIRS)

Near-infrared spectroscopy (NIRS) is an optical method that is non-invasive and used to quantify the concentrations of chromophores, which are light-absorbing molecules, within living tissue. The assessment and correlation of light absorption with the concentration of chromophores in living organisms can be achieved by utilizing non-ionizing light in the near-infrared spectral range to examine tissue⁴². NIRS employs the distinct absorption characteristics of chromophores to quantify their concentrations within tissues. Over the past few decades, NIRS has been extensively employed to monitor regional alterations in cerebral hemodynamics caused by changes in blood oxygenation. Moreover, NIRS enables direct assessment of cerebral metabolism by monitoring alterations in the absorption of cytochrome c oxidase (oxCCO) which is a biomarker known for its high sensitivity to changes in cerebral metabolism⁴³. The concentrations of oxyhemoglobin (HbO₂), deoxyhemoglobin (Hb), and oxCCO can be distinguished thanks to differences in their near-infrared absorption spectra (*Figure 2*). In 1977, Frans F. Jobsis began creating a device based on the NIRS principle. F. F. Jobsis was the first to use a quantitative method to quantify oxygen saturation (StO₂) and CBF⁴⁴.

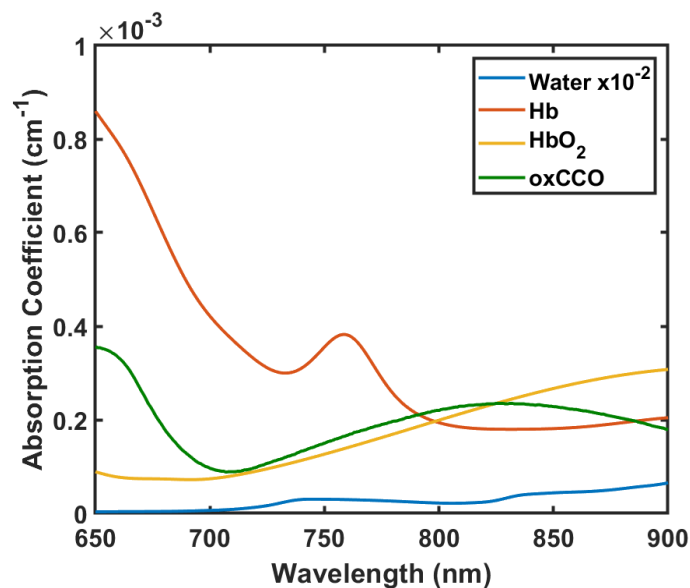


Figure 2: Absorption spectra of both water (blue), oxygenated hemoglobin (red), deoxygenated hemoglobin (orange), and cytochrome-c-oxidase (oxCCO) (green) in the near infrared (NIR) range (650-900nm).

The distinct spectral attributes of hemoglobin enable continuous tracking of the concentration levels of its two states - oxygenated and deoxygenated - through the measurement of near-Infrared (NIR) light absorption across a variety of wavelengths within the NIR spectral range. At wavelengths of 650–900 nm, light absorption occurs by water, lipids, and cytochrome c oxidase in the brain. The two substances that exhibit the lowest absorption of light at the previously mentioned wavelengths are oxy-hemoglobin (HbO₂) and deoxy-hemoglobin (Hb). As a result, NIRS uses 650–900 nm wavelengths, which have relatively low absorption in tissues and allow deeper penetration into brain tissue. As near-infrared light passes through the skull and brain layers, its intensity diminishes due to the combined effects of light scattering and absorption. Hemodynamic alterations in the active cerebral cortex are the principal cause of differences in the absorption spectra⁴⁵.

Reflectance probes are used in *in vivo* NIRS equipment to quantify scattered light re-emitted at a distance of 10–50 mm from where the light enters the tissue. The separation between the source and detector has an impact on the depth to which light can penetrate and the distance it can travel within the tissue, also known as the optical path length. The photons that are detected encounter multiple scattering events, leading to an optical path length that surpasses the distance between the probes. This path length is influenced by the scattering and absorption properties of the tissue and is generally not known. In the context of NIRS tissue spectrometers, it is imperative to address the influence of an uncertain and variable optical path length on the recorded light attenuation signal. This correction is necessary to establish a reliable connection between the detected light signals and accurate measurements of hemoglobin or tissue chromophores⁴⁶. The computation of tissue oxygen saturation (StO₂) can be achieved through the utilization of the subsequent formula:

$$StO_2 = \frac{[HbO_2]}{[HbO_2]+[Hb]} \quad (1.1)$$

The upcoming section will elucidate the analytical basis of NIRS and the underlying principles that govern the conversion of light absorption into quantifiable chromophore concentrations.

Principles of NIRS

Two fundamental interactions between light and tissue will attenuate the light intensity incidents on tissue: absorption and scattering. When the incident light's frequency matches the energy needed to raise the molecule to a higher energy state, the photon is absorbed. In accordance with the Lambert-Beer law⁴⁷, which is rooted in fundamental physical principles, the reduction in the intensity of light passing through a tissue sample is directly proportional to both the path length of the light and the absorption coefficient of the chromophore present. As stated earlier, Jobsis used the Beer-Lambert Law to apply the known spectra of hemoglobin and cytochrome c oxidase to demonstrate that variations in the spectrum recorded throughout the head may be attributed to variations in chromophore concentration⁴⁴. In animals the 'total signal' could be calculated by manipulating the inspired oxygen content; however, quantification of the changes was not achievable due to the lack of knowledge of the path length of the light in the tissues^{44,48}.

The modified Beer-Lambert Law is frequently utilized to convert changes in light attenuations into changes in chromophore concentrations. This modified version takes into account factors such as the differential path length factor (DPF), which accounts for effects such as the scattering of light in tissues^{49,50}. By incorporating DPF and other relevant parameters, the relationship between light attenuation and chromophore concentration can be determined⁴⁷. Furthermore, advanced data analysis techniques, such as spectral fitting algorithms and multichannel measurements, are often utilized to extract quantitative information about chromophore concentrations. These techniques involve modeling the optical properties of tissues, such as scattering and absorption coefficients, to enable robust estimation of chromophore concentrations. It is worth noting that the conversion of light attenuations to chromophore concentrations is a complex process that requires careful calibration and validation. Calibration is typically performed using tissue-mimicking phantoms with known chromophore concentrations, while validation involves comparing the measured concentrations with gold standard techniques, such as blood gas analysis or

invasive monitoring methods⁴⁴. By leveraging the principles of the Beer-Lambert Law and employing sophisticated data analysis techniques, researchers can reliably interpret changes in light attenuations as meaningful variations in chromophore concentrations. This provides valuable insights into the hemodynamic and metabolic processes occurring in the brain, paving the way for a deeper understanding of cerebral physiology and pathology.

Although three primary NIRS techniques have been devised, which includes continuous-wave hyperspectral (CW), time-domain (TD), and frequency-domain (FD) NIRS, a comprehensive examination of these methods falls beyond the scope of this thesis⁵¹. In this thesis, we used a continuous-wave, hyperspectral NIRS (CW *h*-NIRS) device. In CW *h*-NIRS, alterations in tissue oxygenation, HbO₂, and Hb are assessed by quantifying light attenuation across multiple wavelengths. By employing a model of light propagation in tissue, the measured light intensity values can be used to estimate the chromophore concentrations⁵². One approach for determining chromophore concentrations utilizing broadband NIRS relies on the implementation of the modified Beer-Lambert law or second derivative spectra⁵³. This approach has been tailored for dynamic contrast enhanced (DCE) NIRS to assess CBF⁵⁴. However, the absence of noticeable features in the 2nd derivative spectrum of oxyhemoglobin impedes the calculation of tissue oxygen saturation. The methodology utilized in this thesis draws inspiration from Diop's 2015 study, where an innovative approach for evaluating chromophore concentrations was introduced. This approach employed in this study involved the utilization of an analytical model of light propagation in tissue, to analyze both the first and second derivatives spectra, offering an alternative method for assessing chromophore concentrations^{55,56}. The diffusion approximation is a commonly used model for describing light propagation in biological tissues and it is a mathematical model that approximates light propagation in tissues by assuming that the scattering of light is dominant over absorption and that the scattering is isotropic⁵⁷. In this approach, a solution to the diffusion approximation is derived, for the appropriate geometry (e.g., semi-infinite medium) and boundary conditions, and expressed in terms the tissue absorption coefficient (μ_a), and reduced scattering coefficient (μ_s')⁵⁸. Note that μ_s' can be represented using a model of Mie scattering⁵⁹:

$$\mu'_s = A \left(\frac{\lambda}{800} \right)^{-a} \quad (1.2)$$

where A is the μ'_s value at $\lambda = 800$ nm and a represents the scattering power. Further, μ_a is defined as the linear combination of the contribution of HbO₂, Hb, and water to the absorption:

$$\mu_a(\lambda) = [HbO_2] \cdot \varepsilon_{HbO}(\lambda) + [Hb] \cdot \varepsilon_{Hb}(\lambda) + WF \cdot \varepsilon_{H_2O}(\lambda) \quad (1.3)$$

where $\varepsilon(\lambda)$ is the extinction coefficient of Hb and HbO₂, and WF represents the tissue water fraction⁶⁰. HbO₂ and Hb are quantified from μ_a and the concentrations of oxygenated and deoxygenated hemoglobin can be used to estimate tissue oxygen saturation (StO₂)⁶¹.

1.8 Measuring Cerebral Blood Flow with NIR light

The majority of functional cerebral measurements using diffuse optics in both research and clinical settings have predominantly employed NIRS or diffuse optical spectroscopy (DOS)^{63,64}. The NIRS/DOS techniques are commonly utilized for the assessment of tissue concentration dynamics of oxy and deoxyhemoglobin. By employing techniques such as NIRS/DOS, it becomes feasible to obtain information about CBF by incorporating a flow tracer, such as a short intake of 100% oxygen or the administration of a contrast agent. Diffuse correlation spectroscopy (DCS) is another non-invasive technique that utilizes the temporal variations of light intensity to quantify changes in CBF⁶². The method was introduced by Boas et al. in 1995⁶⁶. DCS operates on physical principles that share similarities with those underlying NIRS/DOS techniques, particularly with respect to light transport. It possesses similar benefits to NIRS/DOS, including non-invasiveness, the ability to penetrate deep tissues (~1 cm), exceptional time-resolution, and the potential for continuous bedside monitoring⁶². However, DCS stands apart from NIRS/DOS as it offers a distinct and direct means of quantifying changes in cerebral blood flow by leveraging the statistical characteristics of multiple scattered light^{62,65}.

The technique of DCS enables blood flow monitoring with high temporal resolution. This is accomplished by capturing and analyzing temporal intensity fluctuations in coherent light, which are then processed to generate an autocorrelation function. Higher flow rates result in a reduction of coherence, thereby causing a rapid decline in autocorrelation. The connection between blood flow and a blood flow index (BFI) can be established through this association, as reported in various studies^{66,67}. DCS measurements are frequently transformed into a BFI, a relative measurement of blood flow that is derived by calculating the changes in the diffusion coefficient in relation to a baseline period⁶⁸.

DCS has found utility in diverse clinical scenarios beyond cerebral studies, including malignancies and peripheral arterial disease. Within a relatively short period of time, DCS has undergone extensive validation *in vivo*⁶⁵. This validation includes studies comparing DCS with techniques such as laser Doppler flowmetry (LDF) in rat cerebral and muscular tissues⁶⁹, color Doppler ultrasound (CDU) and transcranial Doppler ultrasound (TCD) in murine tumors, as well as in neonatal and adult cerebral tissues^{40,70}. Additionally, DCS has been compared with phase-encoded velocity mapping MRI in neonatal cerebral tissue⁶⁴, and arterial-spin labeled MRI (ASL-MRI) in human muscular tissue during ischemia, as well as in rat, neonatal, and adult cerebral tissues^{69,71}, with Xenon-CT in injured adult brain⁷², with indocyanine green (ICG) tracers⁶⁷, and fluorescent microsphere CBF tracers⁷³ in piglet cerebral tissue, neonates⁷⁴, as well as in contrast to clinical and pre-clinical predictions predicated on previous endeavors with alternative technological measures of tissue physiology^{62,65}.

Principles of DCS

DCS employs speckle correlation techniques to evaluate blood flow in tissues. By detecting the temporal changes in intensity of coherent NIR light scattered by moving particles in tissue, specifically red blood cells, DCS can assess the blood flow. These temporal fluctuations are quantified by calculating the normalized intensity temporal autocorrelation function at various delay periods, i.e., $g_2(\tau) \equiv \langle I(t) I(t + \tau) \rangle / \langle I(t) \rangle^2$, where $I(t)$ represents the intensity of the detected light at time t and the angular brackets, $\langle \rangle$, denote time-averages⁴⁷. The rate of decay observed in the measured intensity autocorrelation function is indicative of tissue blood flow.

The correlation diffusion equation, represented by $G_1(\tau) \equiv \langle E^*(t) \cdot E(t + \tau) \rangle$, serves as a useful model for studying the transport of the electric field autocorrelation function $(E(t))^{75,76}$. This equation can be analytically solved for specific tissue geometries of interest⁶². CBF can be calculated by applying the Siegert relation to fit the solution for the normalized electric field autocorrelation function, $g_1(\tau) = G_1(\tau)/G_1(\tau = 0)$, to the measured (normalized) intensity autocorrelation function⁴⁷, $g_2(\tau) = 1 + \beta|g_1(\tau)|^2$. The constant β , primarily determined by the experimental collection optics, plays a crucial role in this calculation. The time-varying changes in μ_a , when used in conjunction with the baseline μ_s' to fit the dynamic data, gives the correlation factor (β) and BFi^{67,77}.

The fundamental scenario of point illumination and point detection on the surface of semi-infinite homogeneous tissue involves solving the correlation diffusion equation. This tissue is characterized by an absorption coefficient μ_a , reduced scattering coefficient μ_s' , and tissue BFi⁶⁵.

$$G_1(\tau) = \frac{3}{4\pi\ell_{tr}} \left[\frac{\exp(-K(\tau)r_1)}{r_1} - \frac{\exp(-K(\tau)r_b)}{r_b} \right] \quad (1.4)$$

Here, $K(\tau) = [3\mu_a(\mu_a + \mu_s')(1 + 2\mu_s'k_0^2F\tau/\mu_a)]^{1/2}$, $r_1 = (\ell_{tr} + \rho^2)^{1/2}$, $r_b = [(2z_b + \ell_{tr})^2 + \rho^2]^{1/2}$, ρ represents the source-detector separation, and $\ell_{tr} = 1/(\mu_a + \mu_s')$. Furthermore, $z_b = 2\ell_{tr} (1 + R_{\text{eff}}) / (3(1 - R_{\text{eff}}))$, where R_{eff} is the effective reflection coefficient that is utilized to account for the discrepancy in the index of refraction between the tissue (n) and the non-scattering medium enclosing the tissue (n_{out}). In this geometry, a conventional strategy for blood flow monitoring with DCS is to use the Siegert relation to determine $g_1(\tau)$ from observations of $g_2(\tau)$ ⁶⁰. After that, a nonlinear minimization approach is used to fit the semi-infinite correlation diffusion solution to $g_1(\tau)$, yielding an estimate of the BFi⁷⁸. The observed intensity autocorrelation functions can be fitted to solutions of the correlation diffusion equation to estimate relative blood flow from DCS data. From the data, the best-fit determines a tissue BFi⁶⁸. Despite the fact that BFi does not use standard or absolute blood flow units, it is correlated to cerebral blood flow index (CBFi) and CBF⁷⁷. The solutions of the correlation transport equation share a formal similarity with the solutions for the light fluence rate⁷⁹. These solutions can be easily obtained for standard

geometries, such as infinite, semi-infinite, and layered configurations. The formulation of the inverse problem for diffusing correlation is also similar to that of the diffusing light fluence rate. In this study, the neonate piglet's skull was observed to have a relatively thin thickness, comparable to that of an infant's skull. Therefore, the tissue being examined was assumed to be a semi-infinite homogeneous medium.

DCS has various advantages over conventional CBF measurement methods. Unlike established clinical techniques including computed tomography (Xenon-CT) and positron emission tomography (PET), diffuse correlation spectroscopy (DCS) does not involve the use of ionizing radiation, ensuring the safety of the patient⁸⁰. Furthermore, unlike newer, safer procedures, DCS is very inexpensive, portable, and can be performed numerous times throughout a patient's hospital stay. In contrast to transcranial Doppler ultrasound, which primarily assesses blood flow in major vessels, DCS enables the detection of regional cortical microvascular flow at any location on the patient's head. The setup of DCS instrumentation is straightforward and only necessitates a single wavelength, which can be selected based on laser availability and cost⁸⁰. This stands in contrast to NIRS, which requires multiple wavelengths within the near-infrared tissue absorption range. Additionally, DCS measurements do not require the use of reference phantoms for quantification, unlike NIRS. Lastly, the combination of DCS and NIRS provides a more comprehensive assessment of brain health by simultaneously measuring tissue oxygenation, cerebral blood flow, and oxygen metabolism⁸⁰. In the context of DCS applications in human adults, there are several challenges that should be considered. One of the main challenges is the potential contamination of the optical signals by extracerebral tissue, particularly from the scalp. This can affect the accuracy and interpretation of the measurements obtained from DCS⁸¹.

1.9 Hybrid Optical Instruments

While NIRS and DCS have been used independently of each other, it is possible to measure cerebral metabolism with NIRS and CBF continuously with DCS. The integration of conventional NIRS and DCS within a single device opens up new possibilities for obtaining

comprehensive optical measurements of cerebral hemodynamics and cerebral metabolism. The combination of NIRS and DCS presents a promising avenue for advancing brain monitoring, as it provides for the simultaneous assessment of flow and oxygenation parameters, enabling the determination of the cerebral metabolic rate of oxygen ($CMRO_2$)⁸. The DCS and NIRS combination instruments discussed in this thesis are called hybrid optical instruments. The initial introduction of hybrid DCS-NIRS/DOS technology for cerebral monitoring in rats occurred in 2001, and later extended to the adult brain in 2004^{69,82}. In another study, hybrid NIRS and DCS instruments were used to monitor critically ill acute ischemic stroke patients⁸³. The combination of DCS and NIRS have been noted to be useful for continuous and simultaneously in vivo monitoring of brain and skeletal muscle microcirculation in rats⁸⁴. In fact, the hybrid instrument has been demonstrated experimentally in several contexts, e.g., in piglets⁸⁵, in humans, and premature neonates^{74,80}. A combined dual optical technique that includes frequency-domain diffuse optical spectroscopy (FD-DOS) and diffuse correlation spectroscopy (DCS) has been utilized to obtain noninvasive indices of cerebral blood flow (CBF) and oxygen extraction fraction (OEF)²⁴. The use of NIRS and DCS combination in brain studies allows for the calculation of cerebral blood flow ($CBF=BF_i$) and cerebral metabolic rate of oxygen extraction ($CMRO_2$) using data from both NIRS/DOS and DCS⁸⁶. In a neonatal animal model, the combination of two near-infrared techniques, namely DCS and TR-NIRS, has demonstrated the ability to measure changes in absolute $CMRO_2$ ⁸⁵.

In the case of DCS and NIRS combination, a significant limitation arises from the crosstalk between the two systems operating in the same wavelength range. Previous studies have attempted to address this limitation by employing a multiplexing approach using mechanical shutters. This approach ensures that only one system transmits and receives light at a time, although it does not enable a truly simultaneous measurement⁸⁰. The integration of NIRS and DCS in a single device presents a unique opportunity to conduct comprehensive optical measurements of cerebral hemodynamics and metabolism. This combined approach enables the detection of post-hemorrhagic hydrocephalus caused by IVH before any brain injury becomes apparent.

1.10 Research Objective

The increasing utilization of hybrid optical monitoring systems that combine near-infrared spectroscopy (NIRS) and diffuse correlation spectroscopy (DCS) presents valuable opportunities for acquiring insights into normal physiological processes and pathological conditions. The optimal use of these optical techniques is of paramount importance for early detection of hydrocephalus, which can lead to the development of subsequent brain injury. Moreover, employing hybrid optical devices that simultaneously monitor multiple parameters, such as blood flow, metabolism, and oxygenation, holds promise for early detection of brain damage prior to its occurrence. As discussed earlier, hydrocephalus can result in elevated intracranial pressure (ICP), leading to decreased cerebral blood flow. This reduction in blood flow has implications for cerebral metabolism and oxygenation.

The study presented in this thesis focused on investigating the impact of elevated ICP on cerebral blood flow, cerebral metabolism, and oxygenation using a hybrid optical device (CW *h*-NIRS/DCS). It is *hypothesized* that optical measures of cerebral blood flow (CBF) and oxygenation are sensitive to elevated ICP. Specifically, the main aim of this study was to test this hypothesis in a neonatal piglet model of elevated ICP.

The following were the specific aims of this project:

1. Demonstrate the impact of elevated ICP on CBF and cerebral oxygenation.
2. Investigate the correlation between CPP, CBF and tissue saturation during ICP alterations.

1.11 References

1. Cannavò L, Rulli I, Falsaperla R, Corsello G, Gitto E. Ventilation, oxidative stress and risk of brain injury in preterm newborn. *Ital J Pediatr.* 2020;46(1):1-5. doi:10.1186/S13052-020-00852-1/METRICS
2. Bassan H, Limperopoulos C, Visconti K, et al. Neurodevelopmental outcome in survivors of periventricular hemorrhagic infarction. *Pediatrics.* 2007;120(4):785-792. doi:10.1542/PEDS.2007-0211
3. Neuroprotection from acute brain injury in preterm infants | Canadian Paediatric Society. Accessed June 8, 2023. <https://cps.ca/en/documents/position/neuroprotection>
4. Horbar JD, Badger GJ, Carpenter JH, et al. Trends in mortality and morbidity for very low birth weight infants, 1991-1999. *Pediatrics.* 2002;110(1 Pt 1):143-151. doi:10.1542/PEDS.110.1.143
5. Volpe JJ. Brain injury in premature infants: a complex amalgam of destructive and developmental disturbances. *Lancet Neurol.* 2009;8(1):110-124. doi:10.1016/S1474-4422(08)70294-1
6. Albright AL, Ferson S, Carlos S. Occult hydrocephalus in children with cerebral palsy. *Neurosurgery.* 2005;56(1):93-96. doi:10.1227/01.NEU.0000144779.32401.A2
7. Shah PS, McDonald SD, Barrett J, et al. The Canadian Preterm Birth Network: a study protocol for improving outcomes for preterm infants and their families. *CMAJ Open.* 2018;6(1):E44. doi:10.9778/CMAJO.20170128
8. Rajaram A, Bale G, Kewin M, et al. Simultaneous monitoring of cerebral perfusion and cytochrome c oxidase by combining broadband near-infrared spectroscopy and diffuse correlation spectroscopy. *Biomed Opt Express.* 2018;9(6):2588. doi:10.1364/BOE.9.002588
9. Deger J, Goethe EA, LoPresti MA, Lam S. Intraventricular Hemorrhage in Premature Infants: A Historical Review. *World Neurosurg.* 2021;153:21-25. doi:10.1016/J.WNEU.2021.06.043
10. Klinger G, Osovsky M, Boyko V, et al. Risk factors associated with post-hemorrhagic hydrocephalus among very low birth weight infants of 24-28 weeks gestation. *J Perinatol.* 2016;36(7):557-563. doi:10.1038/JP.2016.18
11. Ballabh P. Intraventricular Hemorrhage in Premature Infants: Mechanism of Disease. *Pediatr Res.* 2010;67(1):1. doi:10.1203/PDR.0B013E3181C1B176
12. Ishiguro A. Perfusion monitoring and intraventricular hemorrhage in preterm infants. *Pediatr Int.* 2017;59(7):759-763. doi:10.1111/PED.13317
13. Papile LA, Burstein J, Burstein R, Koffler H. Incidence and evolution of subependymal and intraventricular hemorrhage: A study of infants with birth weights less than 1,500 gm. *J Pediatr.* 1978;92(4):529-534. doi:10.1016/S0022-3476(78)80282-0

14. Egesa WI, Odoch S, Odong RJ, et al. Germinal Matrix-Intraventricular Hemorrhage: A Tale of Preterm Infants. *Int J Pediatr*. 2021;2021. doi:10.1155/2021/6622598
15. Ment LR, Ådén U, Lin A, et al. Gene-environment interactions in severe intraventricular hemorrhage of preterm neonates. *Pediatr Res*. 2014;75(0):241. doi:10.1038/PR.2013.195
16. Bassan H. Intracranial hemorrhage in the preterm infant: understanding it, preventing it. *Clin Perinatol*. 2009;36(4):737-762. doi:10.1016/J.CLP.2009.07.014
17. Cherian S, Whitelaw A, Thoresen M, Love S. The pathogenesis of neonatal post-hemorrhagic hydrocephalus. *Brain Pathol*. 2004;14(3):305-311. doi:10.1111/J.1750-3639.2004.TB00069.X
18. Murphy BP, Inder TE, Rooks V, et al. Posthaemorrhagic ventricular dilatation in the premature infant: natural history and predictors of outcome. *Arch Dis Child Fetal Neonatal Ed*. 2002;87(1). doi:10.1136/FN.87.1.F37
19. Wright Z, Larrew TW, Eskandari R. Pediatric Hydrocephalus: Current State of Diagnosis and Treatment. *Pediatr Rev*. 2016;37(11):478-488. doi:10.1542/PIR.2015-0134
20. Kumaria A, Toliás CM. Post-traumatic hydrocephalus: unknown knowns and known unknowns. *Br J Neurosurg*. 2022;36(3):295-297. doi:10.1080/02688697.2022.2028723
21. Mazzola CA, Choudhri AF, Auguste KI, et al. Pediatric hydrocephalus: Systematic literature review and evidence-based guidelines. Part 2: Management of posthemorrhagic hydrocephalus in premature infants. *J Neurosurg Pediatr*. 2014;14:8-23. doi:10.3171/2014.7.PEDS14322
22. Cherian S, Whitelaw A, Thoresen M, Love S. The pathogenesis of neonatal post-hemorrhagic hydrocephalus. *Brain Pathol*. 2004;14(3):305-311. doi:10.1111/J.1750-3639.2004.TB00069.X
23. Lindquist B, Persson EK, Uvebrant P, Carlsson G. Learning, memory and executive functions in children with hydrocephalus. *Acta Paediatr*. 2008;97(5):596-601. doi:10.1111/J.1651-2227.2008.00747.X
24. Flanders TM, Lang SS, Ko TS, et al. Optical Detection of Intracranial Pressure and Perfusion Changes in Neonates With Hydrocephalus. *Journal of Pediatrics*. 2021;236:54-61.e1. doi:10.1016/J.JPEDI.2021.05.024
25. Robinson S. Neonatal posthemorrhagic hydrocephalus from prematurity: pathophysiology and current treatment concepts. *J Neurosurg Pediatr*. 2012;9(3):242-258. doi:10.3171/2011.12.PEDS11136
26. Donnelly J, Czosnyka M, Harland S, et al. Cerebral haemodynamics during experimental intracranial hypertension. *Journal of Cerebral Blood Flow and Metabolism*. 2017;37(2):694-705. doi:10.1177/0271678X16639060

27. Miller JD, Stanek A, Langfitt TW. Concepts of cerebral perfusion pressure and vascular compression during intracranial hypertension. *Prog Brain Res.* 1972;35(C):411-432. doi:10.1016/S0079-6123(08)60102-8
28. Mount CA, Das JM. Cerebral Perfusion Pressure. *StatPearls.* Published online April 5, 2022. Accessed June 2, 2023. <https://www.ncbi.nlm.nih.gov/books/NBK537271/>
29. Bragin DE, Statom GL, Yonas H, Dai X, Nemoto EM. Critical Cerebral Perfusion Pressure at High Intracranial Pressure Measured by Induced Cerebrovascular and Intracranial Pressure Reactivity. *Crit Care Med.* 2014;42(12):2582. doi:10.1097/CCM.0000000000000655
30. Bragin DE, Bush RC, Müller WS, Nemoto EM. High intracranial pressure effects on cerebral cortical microvascular flow in rats. *J Neurotrauma.* 2011;28(5):775-785. doi:10.1089/NEU.2010.1692
31. Ellenbogen JR, Waqar M, Pettorini B. Management of post-haemorrhagic hydrocephalus in premature infants. *Journal of Clinical Neuroscience.* 2016;31:30-34. doi:10.1016/J.JOCN.2016.02.026
32. Robinson S. Neonatal posthemorrhagic hydrocephalus from prematurity: pathophysiology and current treatment concepts: A review. *J Neurosurg Pediatr.* 2012;9(3):242-258. doi:10.3171/2011.12.PEDS11136
33. El-Dib M, Limbrick DD, Inder T, et al. Management of Post-hemorrhagic Ventricular Dilatation in the Preterm Infant. *J Pediatr.* 2020;226:16. doi:10.1016/J.JPEDS.2020.07.079
34. Li F, Shi Y, Liu G, Nie C. Ultrasonic Diagnosis and Management of Posthemorrhagic Ventricular Dilatation in Premature Infants: A Narrative Review. *Journal of Clinical Medicine* 2022, Vol 11, Page 7468. 2022;11(24):7468. doi:10.3390/JCM11247468
35. Mazzola CA, Choudhri AF, Auguste KI, et al. Pediatric hydrocephalus: systematic literature review and evidence-based guidelines. Part 2: Management of posthemorrhagic hydrocephalus in premature infants. *J Neurosurg Pediatr.* 2014;14(Supplement_1):8-23. doi:10.3171/2014.7.PEDS14322)
36. Javadpour M, Mallucci C, Brodbelt A, Golash A, May P. The impact of endoscopic third ventriculostomy on the management of newly diagnosed hydrocephalus in infants. *Pediatr Neurosurg.* 2001;35(3):131-135. doi:10.1159/000050406
37. Ferriero DM. Neonatal brain injury. *N Engl J Med.* 2004;351(19):1985-1995. doi:10.1056/NEJMRA041996
38. Shi HM, Sun ZC, Ju FH. Recommendations for reducing exposure to medical X-ray irradiation (Review). *Medicine International.* 2022;2(4):1-7. doi:10.3892/MI.2022.47
39. Volpe JJ, Herscovitch P, Perlman JM, Raichle ME. Positron emission tomography in the newborn: extensive impairment of regional cerebral blood flow with intraventricular hemorrhage and hemorrhagic intracerebral involvement - PubMed.

- Pediatr*. 1983;72. Accessed June 8, 2023. <https://pubmed.ncbi.nlm.nih.gov/6605514/>
40. Buckley EM, Cook NM, Durduran T, et al. Cerebral hemodynamics in preterm infants during positional intervention measured with diffuse correlation spectroscopy and transcranial Doppler ultrasound. *Opt Express*. 2009;17(15):12571. doi:10.1364/OE.17.012571
 41. Boas DA, Franceschini MA. Haemoglobin oxygen saturation as a biomarker: the problem and a solution. *Philos Trans A Math Phys Eng Sci*. 2011;369(1955):4407. doi:10.1098/RSTA.2011.0250
 42. Rajaram A. NNeMo (Neonatal NeuroMonitor) - a hybrid optical system to characterize perfusion and metabolism in the newborn brain. Electronic Thesis and Dissertation Repository. Published online March 16, 2021. Accessed June 18, 2023. <https://ir.lib.uwo.ca/etd/7677>
 43. Bale G, Elwell CE, Tachtsidis I. From Jöbsis to the present day: a review of clinical near-infrared spectroscopy measurements of cerebral cytochrome-c-oxidase. *J Biomed Opt*. 2016;21(9):091307. doi:10.1117/1.JBO.21.9.091307
 44. Jöbsis FF. Noninvasive, infrared monitoring of cerebral and myocardial oxygen sufficiency and circulatory parameters. *Science*. 1977;198(4323):1264-1266. doi:10.1126/SCIENCE.929199
 45. Systems HBSS and, 2015 undefined. Basic principle and practical implementation of near-infrared spectroscopy (NIRS). Springer. Accessed May 28, 2023. https://link.springer.com/chapter/10.1007/978-3-319-14711-6_12
 46. Myers DE, Anderson LD, Seifert RP, et al. Noninvasive method for measuring local hemoglobin oxygen saturation in tissue using wide gap second derivative near-infrared spectroscopy. *J Biomed Opt*. 2005;10(3):034017. doi:10.1117/1.1925250
 47. Baker WB, Parthasarathy AB, Busch DR, Mesquita RC, Greenberg JH, Yodh AG. Modified Beer-Lambert law for blood flow. *Biomed Opt Express*. 2014;5(11):4053. doi:10.1364/BOE.5.004053
 48. Wray S, Cope M, Delpy DT, Wyatt JS, Reynolds EOR. Characterization of the near infrared absorption spectra of cytochrome aa₃ and haemoglobin for the non-invasive monitoring of cerebral oxygenation. *Biochimica et Biophysica Acta (BBA) - Bioenergetics*. 1988;933(1):184-192. doi:10.1016/0005-2728(88)90069-2
 49. Duncan A, Meek JH, Clemence M, et al. Optical pathlength measurements on adult head, calf and forearm and the head of the newborn infant using phase resolved optical spectroscopy. *Phys Med Biol*. 1995;40(2):295-304. doi:10.1088/0031-9155/40/2/007
 50. Essenpreis M, Arridge SR, Delpy DT, Elwell CE, Cope M, Zee P van der. Spectral dependence of temporal point spread functions in human tissues. *Applied Optics*, Vol 32, Issue 4, pp 418-425. 1993;32(4):418-425. doi:10.1364/AO.32.000418

51. Delpy DT, Cope M. Quantification in tissue near-infrared spectroscopy. *Philosophical Transactions of the Royal Society B: Biological Sciences*. 1997;352(1354):649. doi:10.1098/RSTB.1997.0046
52. Strangman G, Franceschini MA, Boas DA. Factors affecting the accuracy of near-infrared spectroscopy concentration calculations for focal changes in oxygenation parameters. *Neuroimage*. 2003;18(4):865-879. doi:10.1016/S1053-8119(03)00021-1
53. Brown DW, Picot PA, Naeini JG, Springett R, Delpy DT, Lee TY. Quantitative near infrared spectroscopy measurement of cerebral hemodynamics in newborn piglets. *Pediatr Res*. 2002;51(5):564-570. doi:10.1203/00006450-200205000-00004
54. Tichauer KM, Hadway JA, Lee TY, Lawrence KS. Measurement of cerebral oxidative metabolism with near-infrared spectroscopy: a validation study. *J Cereb Blood Flow Metab*. 2006;26(5):722-730. doi:10.1038/SJ.JCBFM.9600230
55. Kishimoto J, Lee DSC, Diop M, Toronov V, Lawrence K St. Development of a combined broadband near-infrared and diffusion correlation system for monitoring cerebral blood flow and oxidative metabolism in preterm infants. *Biomedical Optics Express*, Vol 6, Issue 10, pp 3907-3918. 2015;6(10):3907-3918. doi:10.1364/BOE.6.003907
56. Yeganeh HZ, Toronov V, Elliott JT, Diop M, Lee TY, Lawrence K St. Broadband continuous-wave technique to measure baseline values and changes in the tissue chromophore concentrations. *Biomed Opt Express*. 2012;3(11):2761. doi:10.1364/BOE.3.002761
57. Gratton E, Franceschini MA, Fantini S. Semi-infinite-geometry boundary problem for light migration in highly scattering media: a frequency-domain study in the diffusion approximation. *JOSA B*, Vol 11, Issue 10, pp 2128-2138. 1994;11(10):2128-2138. doi:10.1364/JOSAB.11.002128
58. Gratton E, Franceschini MA, Fantini S. Semi-infinite-geometry boundary problem for light migration in highly scattering media: a frequency-domain study in the diffusion approximation. *JOSA B*, Vol 11, Issue 10, pp 2128-2138. 1994;11(10):2128-2138. doi:10.1364/JOSAB.11.002128
59. Jacques SL. Optical properties of biological tissues: a review. *Phys Med Biol*. 2013;58(11). doi:10.1088/0031-9155/58/11/R37
60. Mawdsley L. Using Hyperspectral Near-Infrared Spectroscopy and Diffuse Correlation Spectroscopy to Monitor the Effects of Phenylephrine in the Microcirculation. *Electronic Thesis and Dissertation Repository*. Published online September 28, 2021. Accessed June 18, 2023. <https://ir.lib.uwo.ca/etd/8294>
61. McLachlan P. Quantification of Cerebral Blood Flow and Oxidative Metabolism in Infants with Post-Hemorrhagic Ventricular Dilatation. *Electronic Thesis and Dissertation Repository*. Published online May 25, 2017. Accessed June 18, 2023. <https://ir.lib.uwo.ca/etd/4596>

62. Zhang MJ, Zhao CY, Xiong JN, et al. Diffuse optics for tissue monitoring and tomography. *Reports on Progress in Physics*. 2010;73(7):076701. doi:10.1088/0034-4885/73/7/076701
63. Ferrari M, Quaresima V. A brief review on the history of human functional near-infrared spectroscopy (fNIRS) development and fields of application. *Neuroimage*. 2012;63(2):921-935. doi:10.1016/J.NEUROIMAGE.2012.03.049
64. Ferrari M, Quaresima V. Near Infrared Brain and Muscle Oximetry: From the Discovery to Current Applications. <http://dx.doi.org/101255/jnirs973>. 2012;20(1):1-14. doi:10.1255/JNIRS.973
65. Mesquita RC, Durduran T, Yu G, et al. Direct measurement of tissue blood flow and metabolism with diffuse optics. *Philos Trans A Math Phys Eng Sci*. 2011;369(1955):4390. doi:10.1098/RSTA.2011.0232
66. Boas DA, Campbell LE, Yodh AG. Scattering and Imaging with Diffusing Temporal Field Correlations. *Phys Rev Lett*. 1995;75(9):1855-1858. doi:10.1103/PHYSREVLETT.75.1855
67. Diop M, Verdecchia K, Lee TY, Lawrence KS. Calibration of diffuse correlation spectroscopy with a time-resolved near-infrared technique to yield absolute cerebral blood flow measurements. *Biomed Opt Express*. 2011;2(7):2068. doi:10.1364/BOE.2.002068
68. Durduran T, Yodh AG. Diffuse correlation spectroscopy for non-invasive, microvascular cerebral blood flow measurement. *Neuroimage*. 2014;85(0 1):51. doi:10.1016/J.NEUROIMAGE.2013.06.017
69. Durduran T, Yu G, Burnett MG, et al. Diffuse optical measurement of blood flow, blood oxygenation, and metabolism in a human brain during sensorimotor cortex activation. *Opt Lett*. 2004;29(15):1766. doi:10.1364/OL.29.001766
70. Y S, K G, G Y. Diffuse Correlation Spectroscopy (DCS) for Assessment of Tissue Blood Flow in Skeletal Muscle: Recent Progress. *Anat Physiol*. 2013;3(2). doi:10.4172/2161-0940.1000128
71. Durduran T, Zhou C, Edlow BL, et al. Transcranial Optical Monitoring of Cerebrovascular Hemodynamics in Acute Stroke Patients. *Opt Express*. 2009;17(5):3884. doi:10.1364/OE.17.003884
72. Kim MN, Durduran T, Frangos S, et al. Noninvasive measurement of cerebral blood flow and blood oxygenation using near-infrared and diffuse correlation spectroscopies in critically brain-injured adults. *Neurocrit Care*. 2010;12(2):173-180. doi:10.1007/S12028-009-9305-X
73. Durduran T, Kim MN, Buckley EM, et al. Diffuse Optical Monitoring of Cerebral Oxygen Metabolism at the Bed-Side in Cerebrovascular Disorders. *Frontiers in Optics 2008/Laser Science XXIV/Plasmonics and Metamaterials/Optical Fabrication and Testing (2008)*, paper FTuD2. Published online October 19, 2008:FTuD2. doi:10.1364/FIO.2008.FTUD2

74. Rajaram A, Yip LCM, Milej D, et al. Perfusion and Metabolic Neuromonitoring during Ventricular Taps in Infants with Post-Hemorrhagic Ventricular Dilatation. *Brain Sci.* 2020;10(7):1-13. doi:10.3390/BRAINSCI10070452
75. Yu G. Near-infrared diffuse correlation spectroscopy in cancer diagnosis and therapy monitoring. *J Biomed Opt.* 2012;17(1):010901. doi:10.1117/1.JBO.17.1.010901
76. Yodh AG, Boas DA. Spatially varying dynamical properties of turbid media probed with diffusing temporal light correlation. *JOSA A*, Vol 14, Issue 1, pp 192-215. 1997;14(1):192-215. doi:10.1364/JOSAA.14.000192
77. Lemieux PA, Durian DJ. Investigating non-Gaussian scattering processes by using nth -order intensity correlation functions. *JOSA A*, Vol 16, Issue 7, pp 1651-1664. 1999;16(7):1651-1664. doi:10.1364/JOSAA.16.001651
78. Baker WB, Parthasarathy AB, Busch DR, Mesquita RC, Greenberg JH, Yodh AG. Modified Beer-Lambert law for blood flow. *Biomed Opt Express.* 2014;5(11):4053. doi:10.1364/BOE.5.004053
79. Durduran T, Choe R, Baker WB, Yodh AG. Diffuse optics for tissue monitoring and tomography. *Reports on Progress in Physics.* 2010;73(7). doi:10.1088/0034-4885/73/7/076701
80. Buckley EM, Parthasarathy AB, Grant PE, Yodh AG, Franceschini MA. Diffuse correlation spectroscopy for measurement of cerebral blood flow: future prospects. *Neurophotonics.* 2014;1(1):011009. doi:10.1117/1.NPH.1.1.011009
81. Shoemaker LN, Milej D, Mistry J, St. Lawrence K. Using depth-enhanced diffuse correlation spectroscopy and near-infrared spectroscopy to isolate cerebral hemodynamics during transient hypotension. <https://doi.org/10.1117/1NPh102025013>. 2023;10(2):025013. doi:10.1117/1.NPH.10.2.025013
82. Cheung C, Culver JP, Takahashi K, Greenberg JH, Yodh AG. In vivo cerebrovascular measurement combining diffuse near-infrared absorption and correlation spectroscopies. *Phys Med Biol.* 2001;46(8):2053-2065. doi:10.1088/0031-9155/46/8/302
83. Yu G, Durduran T, Zhou C, Cheng R, Yodh AG. Near-infrared diffuse correlation spectroscopy for assessment of tissue blood flow. *Handbook of Biomedical Optics*. Published online April 19, 2016:195-216. doi:10.1201/B10951-14/NEAR-INFRARED-DIFFUSE-CORRELATION-SPECTROSCOPY-ASSESSMENT-TISSUE-BLOOD-FLOW-GUOQIANG-YU-TURGUT-DURDURAN-CHAO-ZHOU-RAN-CHENG-ARJUN-YODH
84. Mawdsley L. Using Hyperspectral Near-Infrared Spectroscopy and Diffuse Correlation Spectroscopy to Monitor the Effects of Phenylephrine in the Microcirculation. *Electronic Thesis and Dissertation Repository*. Published online September 28, 2021. Accessed June 2, 2023. <https://ir.lib.uwo.ca/etd/8294>
85. Verdecchia Mamadou Diop Ting-Yim Lee Keith St Lawrence K, Verdecchia K, Diop M, Lee TY, St Lawrence K. Quantifying the cerebral metabolic rate of oxygen

by combining diffuse correlation spectroscopy and time-resolved near-infrared spectroscopy. <https://doi.org/10.1117/1.JBO.18.2.027007>. 2013;18(2):027007. doi:10.1117/1.JBO.18.2.027007

86. Mesquita RC, Durduran T, Yu G, et al. Direct measurement of tissue blood flow and metabolism with diffuse optics. *Philos Trans A Math Phys Eng Sci.* 2011;369(1955):4390. doi:10.1098/RSTA.2011.0232

Chapter 2

2 Assessing the Sensitivity of Cerebral Blood Flow and Oxygenation to High Intracranial Pressure with Near-Infrared Light

This chapter features unpublished work in preparation for submission to a peer review journal by Sule Karagulleoglu-Kunduraci and Mamadou Diop.

2.1 Introduction

Premature birth, which occurs before the completion of 37 weeks of gestation, affects 8% of Canadian infants¹. Findings from both preclinical and clinical studies have shown that the underdevelopment of the cerebral vascular system, exacerbated by the complications associated with premature birth such as hemodynamic instabilities, predisposes these infants to cerebral injuries². The germinal matrix, a highly vascularized area, is especially at risk due to fluctuations in CBF associated with prematurity³. In particular, infants born prematurely with very low birth weights (VLBW, < 1500 g) are highly vulnerable to intraventricular hemorrhage (IVH), a condition characterized by bleeding into the cerebral ventricles. The prevalence of IVH is elevated in this demographic due to the susceptibility of the premature brain to hemodynamic instabilities and poor cerebral autoregulation⁴. Hemodynamic instabilities in premature infants pose challenges to adequate cerebral blood flow and oxygenation, leading to high risk of IVH³. Notably, rupture of the delicate germinal matrix, causing subsequent IVH, is attributed to a combination of various intrinsic and extrinsic hemodynamic factors⁵. IVH, which typically manifests within the first 72 hours of life in 15-20% of premature VLBW infants, often progresses to hydrocephalus—an abnormal build-up of cerebral spinal fluid (CSF) in the brain—resulting in high intracranial pressure (ICP) and potential brain injuries⁶.

Hydrocephalus is the most common neuropathology managed in pediatric neurosurgery and has far-reaching implications on cerebral health⁷. Hydrocephalus is a common complication in higher-grade IVH cases (Grade III and IV), where over 50% of the lateral ventricles are filled with blood^{8,9}. When there is an obstruction in the CSF pathways, ICP rises, exerting compressive forces on the surrounding brain tissue adjacent to the

ventricles¹⁰. This increase in ICP can impede cerebral metabolism by compromising CBF and its associated delivery of oxygen to the brain¹¹. High ICP can have compensatory effects on mean arterial pressure (MAP) and cerebral perfusion pressure (CPP). CPP, referring to the pressure gradient responsible for driving blood flow to the brain, is calculated by subtracting ICP from MAP^{12,13}. When MAP decreases, compensatory vasodilation occurs, leading to an increase in cerebral blood volume and subsequently increasing ICP. The relationship between ICP and CPP is crucial in understanding cerebral autoregulation. Elevated ICP can result in a reduction in CPP, potentially impairing cerebral autoregulation^{14,15}. While monitoring ICP is important, CPP is considered a superior marker for monitoring high ICP. Nevertheless, current management of hydrocephalus primarily involves active regulation of ICP. The management of hydrocephalus typically involves vigilance for potential complications linked to IVH and mitigating systemic factors that could exacerbate the condition in neonates². Magnetic resonance imaging (MRI) and computed tomography (CT) are imaging techniques that offer high-resolution visualizations, enabling the diagnosis of preterm brain injury¹⁶. However, it is evident that using MR and CT technologies for regular brain monitoring is not practical since they necessitate transporting unstable preterm infants to the radiology department. Instead, cranial ultrasonography (cUS), a non-invasive imaging technique, is routinely used to detect hydrocephalus¹⁷. Nevertheless, cUS primarily identifies and evaluates damage that has already occurred, limiting its use as a prognostic tool. Thus, there is currently a need for tools that can identify potential indicators prior to brain injury.

Biomedical optics has seen significant advancements in recent years providing cost-effective alternatives for brain monitoring and enabling early detection of hemodynamic and metabolic events that could lead to brain injury^{4-6,18-20}. These optical techniques provide non-invasive and real-time assessments, enabling continuous monitoring of crucial cerebral physiological parameters. Using the principles of light-tissue interaction, these approaches enable quantification of cerebral hemodynamics like blood flow and oxygenation, along with monitoring cerebral oxidative metabolism²¹⁻²³. Techniques such as continuous-wave hyperspectral near-infrared spectroscopy (CW *h*-NIRS), which employs a wide-spectrum light source and a spectrometer to measure variations in the concentrations of oxygenated and deoxygenated hemoglobin (HbO₂ and Hb, respectively)

and to obtain estimates of tissue blood oxygen saturation (StO₂), acting as potential precursor biomarkers for preterm brain injury²⁴. In addition to this, CW *h*-NIRS can measure cerebral metabolism directly by assessing alterations in the oxidation state of cytochrome c oxidase (oxCCO), a parameter closely related to cellular oxygen metabolism²⁵. Previous studies have demonstrated that changes in oxCCO measured by CW *h*-NIRS correlate with cerebral metabolic alterations following brain injury^{25,26}. Furthermore, diffuse correlation spectroscopy (DCS) is a promising perfusion technique that uses near-infrared (NIR) light to monitor CBF continuously by assessing dynamic light scatter from red blood cells²⁷. DCS has undergone validation through comparison with other perfusion techniques, such as dynamic contrast-enhanced NIRS²², Positron Emission Tomography with oxygen-15 (¹⁵O) labelled water²⁸, and arterial spin labelling MRI²⁹.

The combination of NIRS and DCS presents a promising development for improving cerebral monitoring capabilities, by concomitantly assessing cerebral hemoglobin concentration, blood oxygen saturation, blood flow, and metabolism, which together offer a more details picture of tissue health³⁰. In particular, integrating CW *h*-NIRS and DCS permits to study the influence of CBF variations on cerebral oxygen metabolism^{4,6}. This is particularly important since cerebral energy demands can be sustained even during CBF reductions through compensatory mechanisms involving increased oxygen extraction. Therefore, simultaneous monitoring of CBF and oxCCO through DCS and CW *h*-NIRS, respectively, could offer more complete picture of cerebral health⁵. Such concurrent measurements may provide valuable insights, especially in identifying potential high ICP, exceeding the information obtained from individual assessments of perfusion or oxygenation alone^{10,31-33}. This integrated approach enhances the capability to evaluate cerebral health and offers an avenue for more comprehensive monitoring of brain tissue^{4-6,34}. This methodology facilitates simultaneous monitoring of numerous hemodynamic parameters, offering unique insights into the dynamic interplay between oxygen delivery and metabolic functions within the brain.

The concurrent evaluation of cerebral blood flow and oxygen metabolism through the use of DCS and CW *h*-NIRS has the potential to serve as a valuable tool for neuro-monitoring in neonatal intensive care units, particularly for preterm infants. This study hypothesized

that optical measurements of CBF and oxygenation would exhibit sensitivity to elevated ICP. To test this hypothesis, experiments were conducted in a neonatal piglet model. The study aimed to establish a correlation between CBF, cerebral oxygenation, and ICP under conditions of increased ICP.

2.2 Methods

2.2.1 Instrumentation

Previous reports on hybrid CW *h*-NIRS/DCS systems have demonstrated simultaneous monitoring of cerebral blood flow, cerebral oxygen saturation, and metabolism in animal models as well as neonates in the NICU⁴⁻⁶. The system used in the current study (*Figure 3a*) is similar to the hybrid CW *h*-NIRS/DCS systems described in our previous reports^{4-6,18,34-37}. The light source of CW *h*-NIRS subsystem was a 20 W halogen lamp (Ocean Insight HL-2000, FL, USA), equipped with a shutter. The output of the light source was coupled to an optical fiber bundle (3.5 mm active diameter, 30- μ m core, 0.55 numerical aperture) to direct light to the piglet's head. Light diffusely reflected from the tissue was collected with an identical fiber bundle, positioned 28 mm from the emission probe. A second identical fiber bundle directed light from the shutter's output to the Ocean Insight spectrometer (QE6500, FL, USA). The DCS subsystem used a long coherence length, continuous-wave laser emitting at 785 nm (DL785-100s, CrystaLaser, NV), which was coupled to a 400- μ m diameter fiber (core = 400 μ m, numerical aperture = 0.22, Thorlabs, NJ, USA). A shutter (Thorlabs, NJ, USA) was placed between the laser and the multimode fiber to control the timing of the exposure of the tissue to the DCS light. Light that was diffusely reflected from the tissue was collected with a single-mode fiber (core = 4.4 μ m, numerical aperture = 0.13, Thorlabs) placed 25 mm from the DCS emission probe and coupled to a single photon counting module (SPCM, Laser Components, Germany). Fiber ends which collected light from tissue were inserted into a 3D printed probe holder that was specifically designed to be positioned on the scalp (*Figure 3b*).

Concurrent operation of the two subsystems could result in notable crosstalk, as the DCS laser has sufficient power to saturate the detector of the spectrometer. Moreover, the

autocorrelation curves obtained during the activation of CW *h*-NIRS light could be distorted by the incoherent light emitted by the broadband light source. To avoid the issue of crosstalk, a shutter-based multiplexing technique was employed to sequentially collect measurements from each subsystem in an alternating manner. The operation and timing of both subsystems were controlled by a TTL signal obtained from an in-house software developed in LabView. This software also controlled the CW *h*-NIRS and DCS light sources, and the shutter was located between the light sources and the piglet's head. *Figure 3* displays a schematic of the hybrid CW *h*-NIRS/DCS system, along with an example of 3D printed probe holder. The analysis of the CW *h*-NIRS and DCS measurements was conducted using a customized MATLAB script, as detailed in Section 2.2.3. This analysis enabled the determination of cerebral saturation, blood flow, and metabolism.

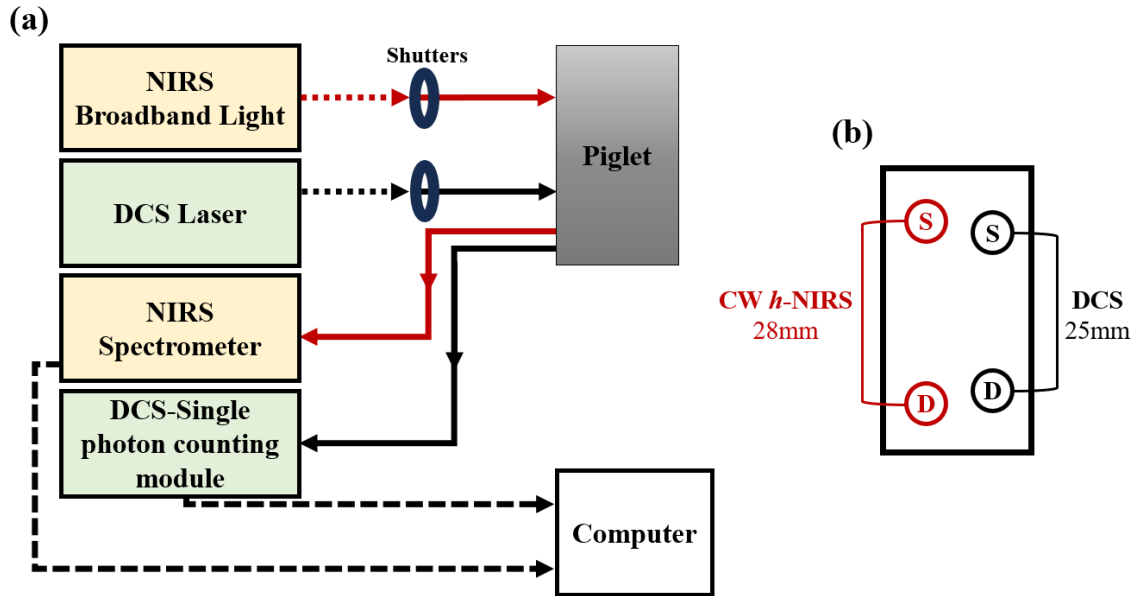


Figure 3: (a) Schematic of the hybrid CW *h*-NIRS/DCS system and (b) 3D-probe holder's geometry. In panel (a), the red lines represent the CW *h*-NIRS signal path, the black lines represent the path of the DCS signal, the black dotted line represent the light propagation prior shutter, and the black dashed lines represent the electronic connections of the CW *h*-NIRS and DCS to the laptop computer. In panel (b), the “S” denotes the source probes, and the “D” denotes the detection probes.

2.2.2 Animal Model

All animal experiments adhered to the Canadian Council on Animal Care guidelines and were approved by the Animal Use Subcommittee at Western University. Data were collected from neonatal piglets ($n=9$, 4 females, age= 3.17 ± 2.21 days (*mean \pm standard deviation*), weight= 2.06 ± 0.53 kg). Piglets were initially anesthetized with isoflurane (4–5% for induction, 1.5–3% for maintenance) and propofol (4–10 mg/kg/hr) during the preparatory surgery. A tracheotomy was carried out to gain control over the piglets' breathing rate, piglets were mechanically ventilated on an oxygen-medical air mixture and small incision was made between the tracheal rings and a tube was inserted and tied in place to prevent dislodging and air leakage. Catheters were inserted into a femoral artery

for vital signs monitoring (SurgiVet, Smiths Medical) and into ear veins for injections and for collecting blood samples for gas and glucose analyses. After the preparatory surgery, a low constant rate infusion of propofol was administered, and the isoflurane level was reduced to 0.5–1% to mitigate its potential for causing lower blood pressures.

Once preparatory surgery was completed, the piglets were placed in the prone position (*Figure 4a*). To measure intracranial pressure (ICP) and to inject saline directly into the ventricles, two small 1-2 mm diameter holes were surgically drilled into the skull. Before drilling, the piglet's head was shaved. Intraventricular catheters were cautiously inserted through these holes until cerebrospinal fluid (CSF) began to flow, which allowed for continuous ICP monitoring and saline infusion into the ventricle via a connected fluid pressure line. The SurgiVet datalogger was attached to the intraventricular catheter that was connected to the fluid pressure line for ICP monitoring. Data streams of ICP and arterial blood pressure (ABP) were recorded using the same SurgiVet Datalogger (Smiths Medical, MN, USA). Another intraventricular catheter was connected to a saline filled syringe pump to inject saline into the ventricle for increasing ICP. Thereafter, piglets were placed in the prone position (*Figure 4a*), and the CW *h*-NIRS and DCS probes were secured to the head, avoiding the sagittal sinus, using a 3D-printed probe holder (*Figure 4b*).

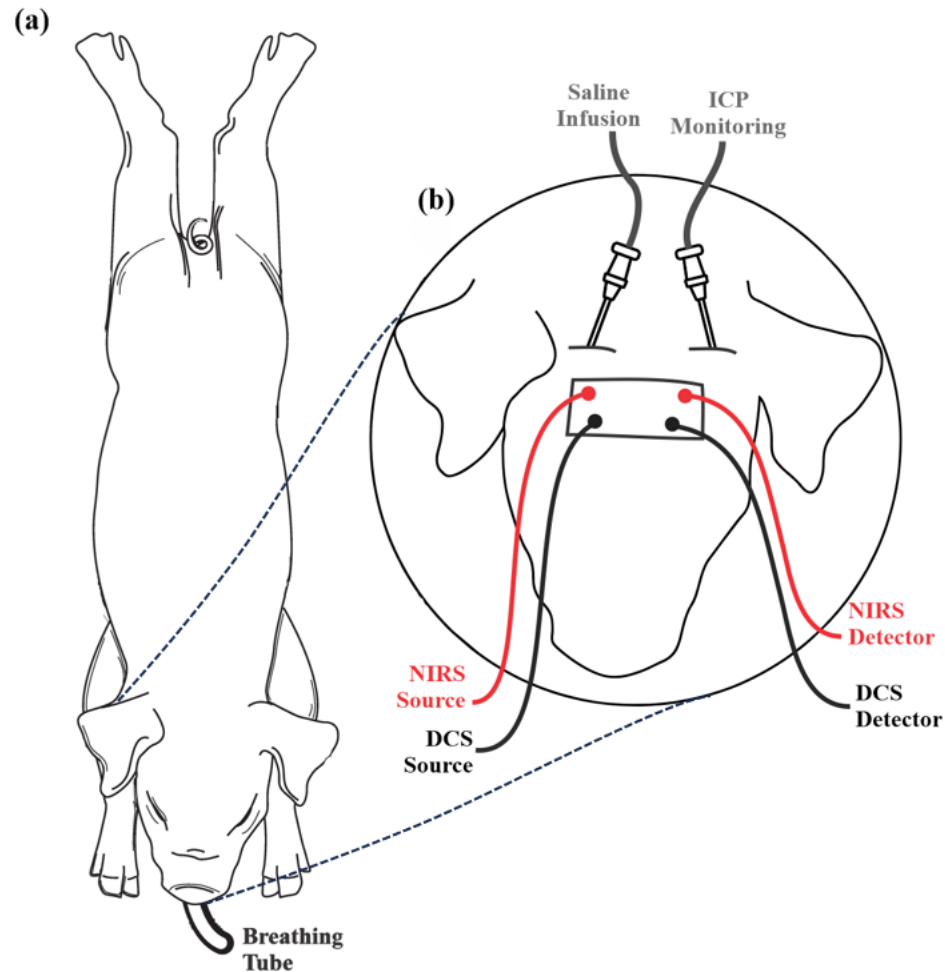


Figure 4: Schematic of the experimental setup for the neonatal piglet, showing the placement of the hybrid CW *h*-NIRS/DCS probes and locations of the ICP catheter and the saline infusion in the ventricles. (a) Illustration of a piglet in prone position. (b) A closed-up drawing of the placement of optical probes and catheters on the piglet's head. (Image adapted from ³⁸)

Prior to piglet neuromonitoring, a dark-noise spectrum was acquired with the probes of the CW *h*-NIRS subsystem on the piglet's head. For the control group, data were collected at a normal ICP level (9 ± 3 mmHg), which served as reference measurements without any ICP alterations. With the experimental group, baseline measurements were acquired for at least 5 minutes at the normal ICP level. Thereafter, the ICP was systematically increased in 5 mmHg increments by infusion of saline into the ventricle (at a rate of 0.2 ml/min) until it reached between 30-40 mmHg. Once the desired ICP range was reached, the saline infusion

was stopped, and the ICP was monitored until it returned to the baseline level. Throughout the procedure, measurements of cerebral blood oxygenation and CBF were continuously acquired with the CW *h*-NIRS and DCS system. The near-simultaneous collection of data was made possible by the use of the shutter multiplexing system. The duration of each ICP increase-decreased cycle varied depending on the response of the animal to the challenge but typically lasting around 1 hour.

2.2.3 Data Processing

2.2.3.1 Quantifying Tissue Chromophore Concentrations by CW *h*-NIRS

Prior to the initiation of each study, the spectrometer's wavelengths were calibrated using a neon light source. Following this, a reference spectrum was captured using a pinhole attenuator, to avoid saturating the detector, thereby accounting for the spectral shape of both the light source and the spectrometer. Additionally, a dark-noise spectrum was measured and subtracted from the reference signal. The baseline reflectance spectrum $R(\lambda)$ was calculated from the spectrum ($spectrum_{\lambda}$) measured on the piglet's head, the dark-noise spectrum ($dark_{\lambda}^1$) acquired on the piglet's head, the reference spectrum ($reference_{\lambda}$), and the dark-noise ($dark_{\lambda}^2$) measured during the acquisition of the reference spectrum, the reflectance spectrum, $R(\lambda)$, as follows described by Diop et al. in 2014^{35,39,40}:

$$R(\lambda) = \left(\frac{spectrum_{\lambda} - dark_{\lambda}^1}{reference_{\lambda} - dark_{\lambda}^2} \right) \quad (2.1)$$

The concentration of chromophores such as water, deoxygenated hemoglobin (Hb), and oxygenated hemoglobin (HbO₂) were calculated following the techniques outlined in our previous study¹⁸. Briefly, the first and second derivative of $R(\lambda)$ were fitted to the first and second derivatives of the solution to the diffusion approximation for semi-infinite homogeneous medium (i.e., the theoretical model)⁴¹. The derivatives refer to the spectral derivatives of the measured reflectance spectrum ($R(\lambda)$) and the theoretical model is a solution to the diffusion approximation for a semi-infinite homogeneous medium⁴¹. The

fitting of the first and second derivatives of $R(\lambda)$ to the first and second derivatives of the solution to the diffusion approximation for a semi-infinite homogeneous medium implies that the measured reflectance spectrum is compared to the theoretical model by analyzing their respective derivatives. This fitting process allows for the estimation of the optical parameters of the medium, such as the absorption coefficient and the reduced scattering coefficient. The reduced scattering (μ_s') and absorption (μ_a) coefficients are provided in equations (2.2) and (2.3)⁴², respectively.

$$\mu_s' = A \left(\frac{\lambda}{800} \right)^{-\alpha} \quad (2.2)$$

A denotes the μ_s' value at $\lambda=800$ nm, and α represents the scattering power. The absorption coefficient (μ_a) was defined as:

$$\mu_a(\lambda) = WF \cdot \varepsilon_{H_2O}(\lambda) + Hb^b(\lambda) \cdot \varepsilon_{Hb}(\lambda) + HbO_2^b \cdot \varepsilon_{HbO_2}(\lambda) \quad (2.3)$$

where $\varepsilon(\lambda)$ represent the extinction coefficient of the corresponding chromophores, Hb^b , and HbO_2^b are respectively the baseline concentrations of deoxyhemoglobin and oxyhemoglobin in μM , and WF represents the tissue water fraction. The determination of chromophore concentrations was carried out by implementing a two-step, multi-parameter fitting approach which involved fitting both the first and second derivatives of the observed reflectance. This method of evaluation was guided by the procedures developed by Diop in 2015¹⁸. In the initial baseline analysis, the influence of the oxidation state of cytochrome c oxidase (oxCCO) was not considered because the derivative spectra of oxCCO have more prominent features in the spectral range of the measurements (i.e., 560-950 nm), and its concentration is relatively low, compared to other chromophores¹⁸. Baseline tissue oxygen saturation (StO_2^b) was computed from the estimated hemoglobin concentrations:

$$StO_2^b = \frac{HbO_2^b}{Hb^b + HbO_2^b} \quad (2.4)$$

where the superscript b denotes baseline values.

2.2.3.2 Changes in oxidation state of cytochrome c oxidase

After establishing a baseline measurement period of at least five minutes, changes in concentrations of Hb, HbO₂, and oxCCO were computed utilizing a modified Beer-Lambert Law^{4,5}, which is based on the UCLn algorithm and represented in Equation 2.5²⁵. It's crucial to note that the analysis of oxCCO requires a specific narrowed range of wavelengths, distinct from those used for Hb and HbO₂ measurements.

$$\begin{bmatrix} \Delta HbO_2 \\ \Delta Hb \\ \Delta oxCCO \end{bmatrix} = \frac{1}{DPF \times \rho} \begin{bmatrix} \epsilon_{HbO_2}(\lambda_1) & \epsilon_{Hb}(\lambda_1) & \epsilon_{oxCCO}(\lambda_1) \\ \vdots & \vdots & \vdots \\ \epsilon_{HbO_2}(\lambda_n) & \epsilon_{Hb}(\lambda_n) & \epsilon_{oxCCO}(\lambda_n) \end{bmatrix}^{-1} \times \begin{bmatrix} \Delta A(\lambda_1) \\ \vdots \\ \Delta A(\lambda_n) \end{bmatrix} \quad (2.5)$$

In this equation, ΔHb , ΔHbO_2 and, $\Delta oxCCO$ denote the relative changes from baseline in oxy-hemoglobin, deoxy-hemoglobin, and the oxidation state of cytochrome c oxidase, respectively. DPF represents the differential pathlength, ρ is the source-detector distance and ΔA is the measured change in attenuation. DPF was determined to be 3.85, based on previous literature representing measurements in the piglet head⁴³⁻⁴⁵. The relative measures acquired by the modified Beer-Lambert approach were paired with the absolute baseline values from the derivative approach in section 2.2.3.1 to obtain the time dependent concentration of Hb, HbO₂, and total hemoglobin (tHb), and StO₂^{18,46}. Total hemoglobin (tHb) is the sum of Hb and HbO₂ and this measure provides valuable information about the overall blood volume in the brain.

2.2.3.3 Monitoring CBF

The cerebral blood flow index (CBFi) was estimated using the methods described by Diop (2011)³⁷. The DCS measurements was analyzed by first transforming the measured normalized intensity autocorrelation curves into electric field autocorrelation, following the Siegert relation^{6,37}:

$$g_2(\rho, \tau) = 1 + \beta \frac{|G_1(\rho, \tau)|^2}{\langle I(\rho, \tau) \rangle^2} \quad (2.6)$$

Here $g_2(\rho, \tau)$ refers the measured normalized intensity autocorrelation, β represents the coherence factor, $G_1(\rho, \tau)$ represents the electric field autocorrelation function, and

$\langle I(\rho, \tau) \rangle$ represents the averaged detected intensity. ρ corresponds to the source-detector distance and τ is the correlation time. The known values of $\rho=25\text{mm}$ and, μ_s' and μ_a at 785 nm that were obtained from the CW *h*-NIRS analysis and used to fit the experimental $G_1(\rho, \tau)$ curves to a theoretical model, based on the solution to the Correlation Diffusion Equation for a semi-infinite homogeneous medium^{4,35,37}. Note that time-dependent μ_a , along with the baseline μ_s' , were employed to fit the data³⁷. This approach permits estimation of the CBFi. Changes in CBF were computed using the changes in CBFi with the data normalized to mean baseline CBFi measurements³⁷.

2.2.3.4 Statistical Analysis

All data are presented as '*mean \pm standard deviation*', unless otherwise specified. Statistical analyses were conducted to identify correlation between cerebral blood flow, oxygenation, and ICP. Statistical significance was established at $p < 0.05$. Baseline measurements were computed by averaging the time course of changes in Hb, HbO₂, oxCCO, and CBFi across all piglets in the control group, as well as those in the experimental group during the baseline ICP (i.e., without any alterations in ICP).

For the experimental group, cerebral perfusion pressure (CPP), which represents the overall pressure difference facilitating oxygen delivery to brain tissue, was calculated by subtracting ICP from the measured mean arterial pressure (MAP). The MAP was determined from recorded arterial blood pressure. The time course of mean changes in CBFi, Hb, HbO₂, and StO₂ were calculated for each CPP level and compared with the measured changes in CPP using Pearson correlation. The impact of CPP on Hb, HbO₂, and StO₂ was determined using the Independent-Samples t-test. Both linear regression and Pearson correlation analyses were used to assess the association between Hb, HbO₂, StO₂, and CPP. The same approach was used to investigate the correlation between CBFi and CPP during ICP alterations.

To determine the relative changes in parameters such as Hb, HbO₂, oxCCO, StO₂, and CBFi during ICP alterations, Independent-Samples t-tests were employed. Additionally, a

one-way ANOVA was used to determine whether there are any statistically significant differences between the means of all the parameters (Hb, HbO₂, oxCCO, StO₂ and CBFi) during ICP alterations for each piglet in the experimental group.

Cluster analysis was conducted by organizing the data (Hb, HbO₂, StO₂ and, CBFi) into groups or clusters based on their close association, aiding in correlation calculations. Descriptive statistics techniques were used to explore differences between clusters. An independent-sample t-test was conducted to compare the means of two different clusters for the same experimental run. Post clustering, a One-Sample t-test was conducted to determine if the clusters deviated significantly from zero, while an analysis of covariance (ANCOVA) and F-test were used to examine if the clusters were significantly different from one another, thereby allowing for cluster identification.

2.3 Results

This was a prospective cohort study involving a total of nine newborn piglets, with seven ($n = 7$) animals in the experimental group and two controls. The main difference between the two groups is that ICP was not altered in the controls. *Table 1* provides an overview of the characteristics of the piglets, including sex and weight, along with the designation of whether they were assigned to the experimental or control group.

Table 1: Demographic and Group Assignment (Neonatal Piglets)

Piglet #	ID	Age (day)	Sex	Weight (kg)	Group
1	C1	5	Female	2	Control
2	C2	8	Female	3.2	Control
3	E1	3.5	Female	2.4	Experimental
4	E2	3	Female	2.2	Experimental
5	E3	1	Male	1.8	Experimental
6	E4	3	Male	2	Experimental
7	E5	2	Male	1.4	Experimental
8	E6	1	Male	1.5	Experimental
9	E7	2	Male	2	Experimental

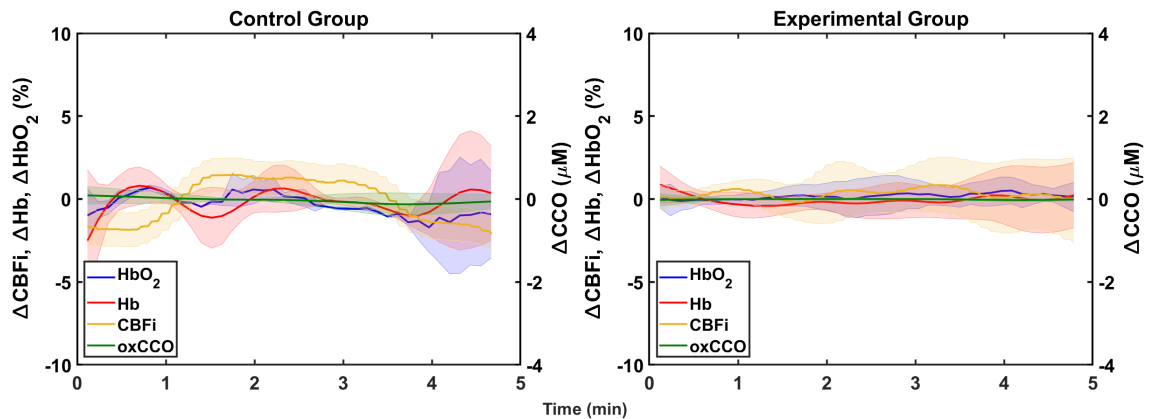


Figure 5: Average changes in tissue chromophores and blood flow without ICP changes for all piglets in the control group ($n=2$, **Control Group: C1-C2**) and the experimental group ($n=7$, **Experimental Group: E1-E7**). The blue lines represent changes in HbO_2 concentrations, the red lines represent changes in Hb concentrations, the green lines represent changes in oxCCO and the orange lines represent percentage changes in CBFi . The solid lines are the mean across the group and the shaded areas represent standard derivations. Note that all concentrations are expressed in μM .

Figure 5 presents the averaged time course of changes in Hb , HbO_2 , oxCCO and CBFi for all the piglets at the baseline ICP level. These measurements provide a baseline against which any subsequent changes in the experimental group can be compared. As anticipated, there were no significant changes in Hb , HbO_2 , oxCCO , and CBFi in any of the groups during the baseline measurements (i.e., at the baseline $\text{ICP}=9\pm 3$ mmHg).

Figure 6 displays the temporal changes in ΔHb , ΔHbO_2 , ΔoxCCO , cerebral blood flow index (ΔCBFi), tissue saturation (StO_2), and cerebral perfusion pressure (ΔCPP) during ICP alterations via direct saline infusion into the ventricle in one piglet for two experimental runs (i.e., two cycles of ICP increased and decreased). Similar data for the rest of the experimental group can be found in the Appendices. The data in Fig. 6 were collected with the CW *h*-NIRS subsystem and illustrate the cerebral hemodynamic responses to ICP changes.

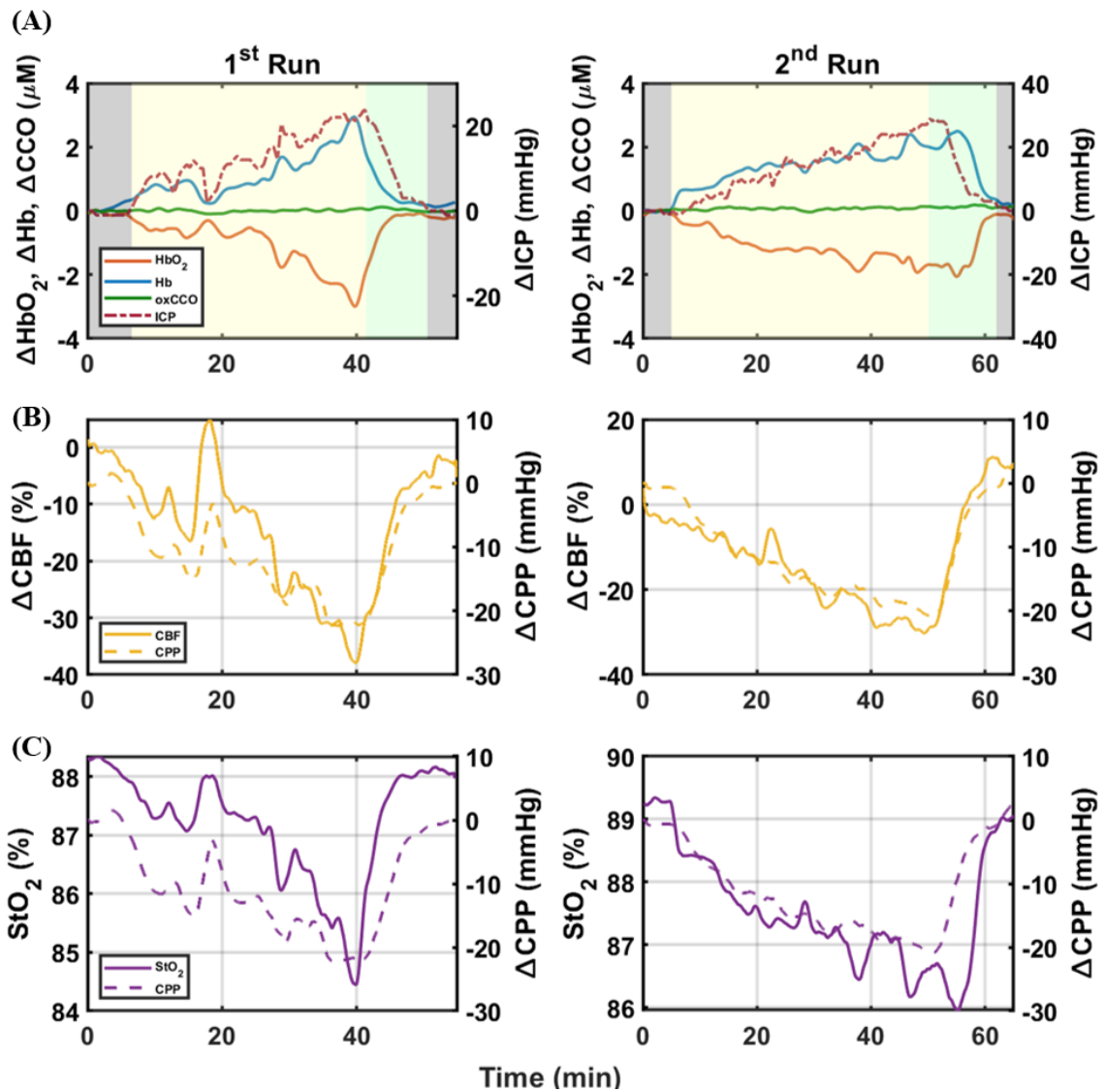


Figure 6: (A) Time dependent changes in ΔHb , ΔHbO_2 and ΔoxCCO with ΔICP from one piglet in the experimental group (E1) for the two runs. The orange lines represent ΔHbO_2 , the blue lines represent ΔHb , the green lines represent ΔoxCCO in μM , and the dark red lines represent ΔICP in mmHg. In panel (A), the grey box illustrates the baseline ICP period, the yellow box illustrates the increased ICP period, and the green box illustrates the decreased ICP period. (B) and (C) Time-dependent changes in ΔCBF and StO_2 with changes in CPP (ΔCPP) from same piglet (E1) for two runs in (%), respectively.

Initially, measurements were taken at the baseline ICP level for at least 5 minutes. Afterwards, the ICP was incrementally increased by an average of 5mmHg from the baseline through the infusion of saline. Once the intended ICP increase was accomplished, the saline infusion was maintained until the ICP level stabilized and the measurement was continued by waiting for at least 5 minutes after the ICP level stabilized. This process was repeated until the ICP increment was between 25-35 mmHg from the baseline. The duration in which the ICP was elevated from the baseline level to the above-mentioned increase of ICP was referred to as the increased ICP period. Once the specified ICP level was reached, the saline infusion was halted, and the ICP was monitored until it naturally returned to the baseline level. The time frame from when the ICP decreased from the highest level back to the baseline level was referred as the decreased ICP period.

It's crucial to mention that due to unexpected experimental challenges, including elevated mean arterial pressure (MAP) and heart rate towards the end of the increased ICP period, it was sometimes necessary to terminate the measurements prematurely in some piglets in the experimental group. This meant that these piglets did not fully complete the decreased ICP period or return to the baseline ICP before the measurements were stopped.

Figure 6A shows that increasing ICP is accompanied by corresponding increases in Hb and decreases in HbO₂. These changes are notable during both runs (i.e., cycles of increased/decreased ICP). In contrast, changes in ICP do not significantly impact oxCCO levels, which remain relatively stable throughout the experiment. It is noteworthy that this pattern was observable in all piglets in the experimental group (see Appendix A-F). A multiple regression analysis was conducted to ascertain whether the changes in Hb, HbO₂, and oxCCO significantly deviated from their baseline values in response to variations in CPP. In the case of Hb, the *F statistic* was found to be **251.9** with a *p-value* less than **0.001**. These results suggest that the changes in Hb were significantly different from the baseline, during the ICP alteration periods. Similarly, for HbO₂, the *F statistic* was **252.9**, indicating a significant difference of HbO₂ changes from baseline values (*p* < **0.001**). Thus, the regression model for both Hb and HbO₂ is deemed statistically significant. However, in the case of oxCCO, the *F statistic* was relatively lower at **10.4** (*p* > **0.15**) and there is no significant difference between the baseline oxCCO value and changes in oxCCO.

Additionally, from the data depicted in *Figure 6A*, it is noted that the levels of tHb remain constant, showing no significant variations even as it was observed changes in the levels of its components, Hb and HbO₂.

Figure 6B & 6C show the changes in cerebral blood flow index (ΔCBFi), tissue saturation (StO_2), and cerebral perfusion pressure (ΔCPP) over time, as measured during two experimental runs in the same piglet as in *Fig. 6A*. All three parameters (ΔCPP , ΔCBFi , and StO_2) displayed quick changes during the ICP alteration. As shown in *Figure 6B & 6C*, an increase in ICP leads to a decrease in CPP, ΔCBFi , and StO_2 . Remarkably, these three parameters (ΔCPP , ΔCBFi , and StO_2) exhibited nearly identical trends in response to the increasing ICP. It is noteworthy that this pattern was consistent across all the runs within the experimental group (Appendix A-F). Moreover, multiple regression analyses were used to evaluate ΔStO_2 and ΔCBFi with ΔCPP during ICP alterations ($p < 0.001$). This low p-value suggests that the variations in StO_2 and CBFi were statistically significant relative to their baseline values (*Table 2*).

Table 2: Baseline values for all parameters

Piglet ID	Hb (μM)	HbO ₂ (μM)	StO ₂ (%)	CBFi (%)	ICP (mmHg)	CPP (mmHg)
E1	8.46 \pm 0.80	66.91 \pm 1.99	88.79 \pm 0.65	10.34 \pm 6.27	8.5 \pm 0.7	41.0 \pm 0.0
E2	8.27 \pm 0.69	65.32 \pm 3.77	86.47 \pm 3.51	4.2 \pm 8.09	12.0 \pm 4.2	36.0 \pm 7.0
E3	7.82 \pm 1.47	62.35 \pm 3.49	88.92 \pm 1.34	0.18 \pm 4.50	10.0 \pm 3.5	33.3 \pm 7.2
E4	11.97 \pm 0.17	61.15 \pm 2.19	83.63 \pm 0.58	3.92 \pm 3.06	8.3 \pm 1.2	32.7 \pm 1.5
E5	5.12 \pm 0.10	58.02 \pm 1.02	91.89 \pm 0.27	1.64 \pm 1.04	16.0 \pm 7.1	33.0 \pm 4.2
E6	8.71 \pm 0.67	68.79 \pm 0.08	88.77 \pm 0.77	3.12 \pm 6.56	11.5 \pm 2.1	30.5 \pm 3.5
E7	15.06 \pm 1.60	54.19 \pm 1.35	78.29 \pm 1.52	1.53 \pm 6.58	13.3 \pm 2.1	28.7 \pm 3.1

Table 2 presents the baseline values for various hemodynamic parameters across seven piglets in the experimental group labeled E1 through E7. The parameters studied include concentrations of Hb, HbO₂, and oxCCO in μM units. Additionally, the table provides values for StO₂ in percentage (%), CBFi also in percentage, ICP in mmHg, and CPP in the same units.

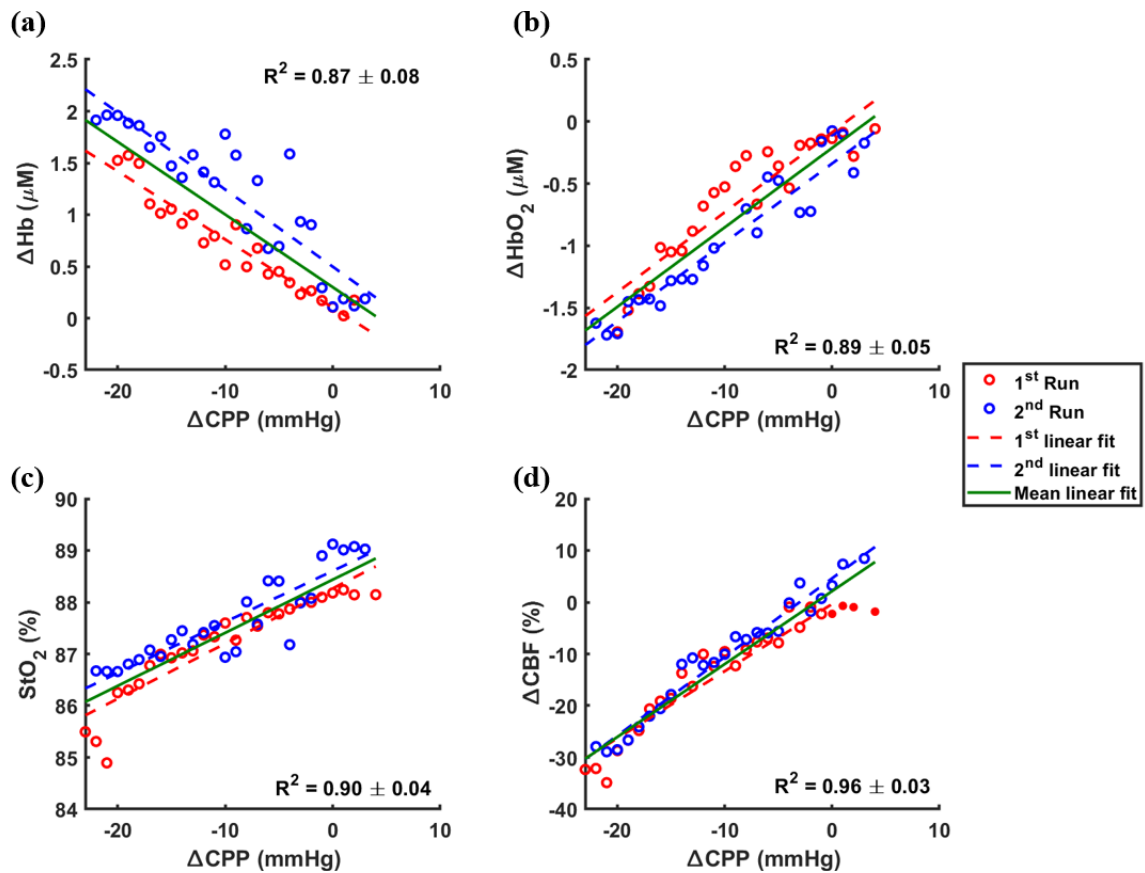


Figure 7: Correlation plots of (a) ΔHb versus ΔCPP , (b) ΔHbO_2 versus ΔCPP , (c) changes in StO_2 versus ΔCPP , (d) ΔCBFi versus ΔCPP for one piglet (E1) for three runs. The dashed lines represent the best fit of regression line, the solid green lines represent mean fitted linear line for first and second run ($p < 0.05$, $R^2 > 0.91 \pm 0.04$).

Figures 7 and Figure 8 present the results of the regression analysis for determining the correlation of the four parameters with Δ CPP during ICP alteration: (a) Δ Hb and Δ CPP, (b) Δ HbO₂ and Δ CPP, (c) Changes in StO₂ and Δ CPP, and (d) Δ CBFi and Δ CPP. The regression analyses were conducted individually for the parameters (Δ Hb, Δ HbO₂, StO₂, and Δ CBFi) derived from the experiments involving each piglet. Changes in these parameters were assessed in relation to their relevant baseline values.

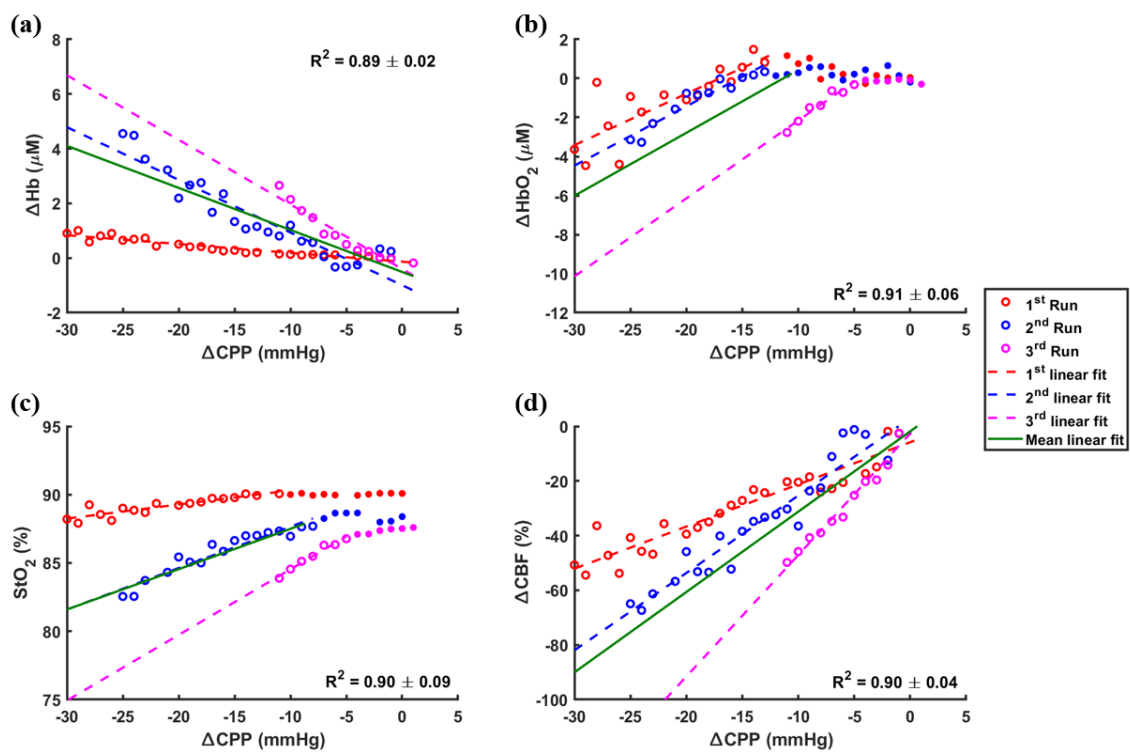


Figure 8: Correlation plots of (a) Δ Hb versus Δ CPP, (b) Δ HbO₂ versus Δ CPP, (c) Changes in StO₂ versus Δ CPP, (d) Δ CBFi versus Δ CPP for one piglet (E3) for three runs. The filled scatter dots represent the clusters' data points for the delayed response for HbO₂ and StO₂. The dashed lines represent the regression line, the solid green lines represent mean of the fitted linear lines for all there runs ($p < 0.001$, $R^2 > 0.9 \pm 0.01$).

To explore potential inter-piglet variability in physiological parameters during ICP alterations alongside CPP changes, linear regression was used to relate each physiological parameter (ΔHb , ΔHbO_2 , StO_2 and ΔCBFi) with ΔCPP . The analysis revealed a statistically significant correlation between CPP and these parameters (*Figure 7*). More specifically, there was a strong negative correlation between ΔHb and ΔCPP , and a strong positive correlation between CCP and ΔHbO_2 , StO_2 and ΔCBFi ($p < 0.001$). The data from the first piglet in the experimental group (E1) underwent Pearson correlation analysis and regression analysis to examine the relationship between changes in ΔHb , ΔHbO_2 , StO_2 , and ΔCBFi , which were fitted with a regression line. The results revealed a significant negative correlation between ΔHb and ΔCPP ($r = -0.91 \pm 0.01$, $p < 0.001$). Conversely, ΔHbO_2 ($r = 0.95 \pm 0.03$, $p < 0.001$), ΔStO_2 ($r = 0.92 \pm 0.03$, $p < 0.001$), and ΔCBFi ($r = 0.97 \pm 0.02$, $p < 0.001$) displayed a strong positive correlation with ΔCPP .

Figure 8 shows that ΔHb and ΔCBFi are strongly correlated to ΔCPP , similar to what was observed in *Figure 7*, while ΔHbO_2 and StO_2 show a delayed response to ΔCPP . Notably, panels (b) and (c) show a delayed response of ΔHbO_2 and StO_2 to decreased CPP, caused by increased ICP, for three different experimental runs of the same piglet (E3). Cluster analysis was conducted on the data that displayed delayed response and revealed the existence of two clusters: data that represent the delayed response and data that correlated linearly with CPP. The slope of the cluster for ΔHbO_2 and StO_2 that correspond to the delayed response was not significantly different from zero (i.e., it was a flat line) ($p > 0.05$). Comparisons between the two clusters (the delayed response and the correlated linearly with CPP) show significant differences in the ΔHbO_2 and StO_2 for one piglet (E3) for three runs ($p < 1e^{-7}$ and $p < 5e^{-7}$, respectively). Note that similar data for the remaining piglets of the experimental group can be found in Appendix (G-K).

Regression analysis was performed for changes in ΔHb , ΔCBFi and the clusters in ΔHbO_2 and changes in StO_2 that could be fitted with a regression line, and there was a strong negative correlation between ΔHb and ΔCPP ($p < 0.001$), while ΔHbO_2 , ΔStO_2 and ΔCBFi showed a strong positive correlation with ΔCPP ($p < 0.001$). In addition to regression analysis, Pearson correlation analysis was conducted for variations in ΔHb , ΔCBFi , and clusters in ΔHbO_2 and StO_2 that were suitable for regression line fitting. The findings showed a strong negative correlation between ΔHb and ΔCPP with a correlation coefficient “ r ” of -0.94 ± 0.02 and a highly significant p -value of less than 0.001 . On the contrary, a strong positive correlation was observed between changes in ΔHbO_2 , StO_2 , ΔCBFi , and ΔCPP . Specifically, ΔHbO_2 exhibited a correlation coefficient of 0.95 ± 0.03 with ΔCPP , StO_2 had a correlation coefficient of 0.95 ± 0.05 with ΔCPP , and ΔCBFi presented a correlation coefficient of 0.97 ± 0.02 with ΔCPP . For all these measurements, the p -value was less than 0.001 , signifying the strong statistical significance of these correlations.

Figure 9 displays the results of the regression analysis used to assess the correlation between mean changes in CBF and mean changes in CPP during the ICP alterations for all piglets in the experimental group. The mean data represents the average of the runs for each piglet. The results of the regression and Pearson correlation analyses for each piglet are presented in *Table 3*. The regression analysis showed a strong correlation between changes in CBF and CPP with a slope of 1.53 ± 0.26 and an intercept of 0.80 ± 6.50 for the experimental group. The Pearson correlation analysis also showed a significant correlation between ΔCBF and ΔCPP for all piglets in the experimental group ($r > 0.95 \pm 0.02$, $p < 0.05$, r is the Pearson correlation coefficient).

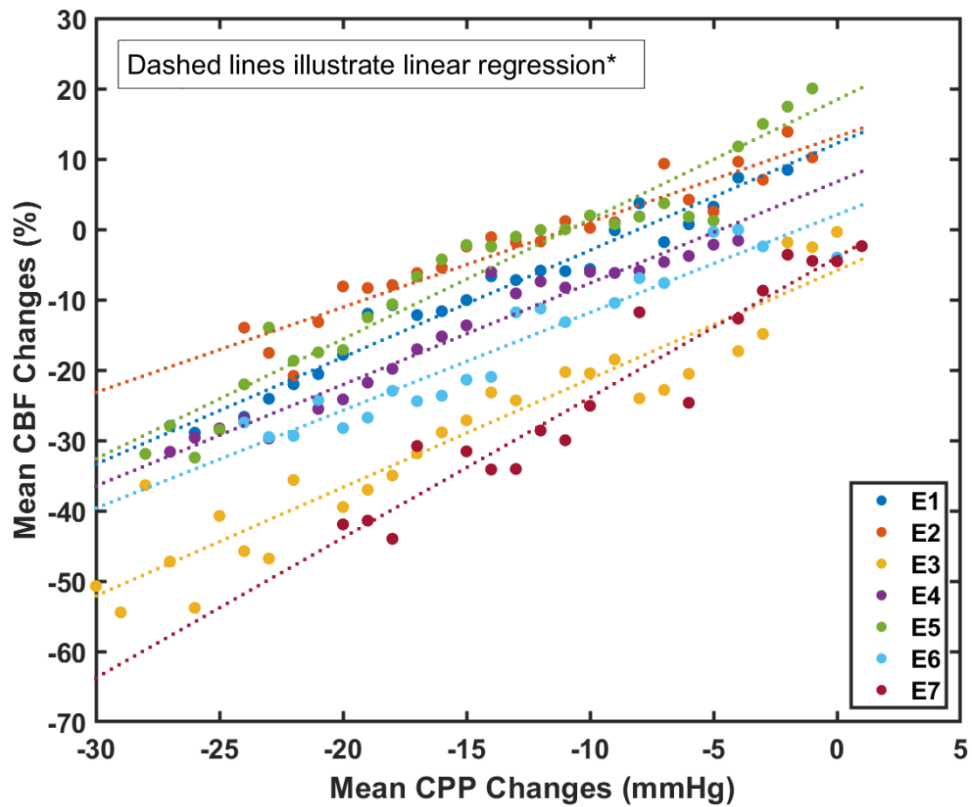


Figure 9: Correlation plot of the relationship between changes in mean CBF and CPP changes during ICP alterations for all piglets in the experimental group (Experimental group: E1, E2, E3, E4, E5, E6 and E7). The dashed lines represent the results of linear regression.

Table 3: Results of the linear regression and Pearson correlation for mean changes in CBF and CPP are presented. Linear regression: $y = \bar{a}x + \bar{b}$, \bar{a} is mean slopes across all the runs in one piglet, \bar{b} is mean intercepts and R^2 (R-squared) is the coefficient of determination. " r " represents the Pearson correlation coefficient.

Piglet ID	\bar{a}	\bar{b}	R^2	r
E1	1.52 ± 0.16	4.62 ± 3.51	0.96 ± 0.03	0.98 ± 0.02
E2	1.21 ± 0.05	7.10 ± 2.50	0.91 ± 0.04	0.94 ± 0.02
E3	1.54 ± 1.45	-5.83 ± 4.45	0.90 ± 0.04	0.97 ± 0.02
E4	1.44 ± 0.18	-0.04 ± 0.55	0.95 ± 0.02	0.94 ± 0.02
E5	1.70 ± 0.17	9.93 ± 2.64	0.94 ± 0.02	0.97 ± 0.01
E6	1.28 ± 0.11	-6.19 ± 1.41	0.89 ± 0.03	0.94 ± 0.02
E7	1.99 ± 0.20	-3.98 ± 9.17	0.92 ± 0.02	0.96 ± 0.01

2.4 Discussion

The motivation of this study was to assess the sensitivity of cerebral blood flow (CBF) and cerebral oxygenation to elevated intracranial pressure (ICP), as previous pilot clinical studies suggested that they are sensitive to hydrocephalus induced elevated ICP. This study examined the correlation between ICP, CBF, and cerebral oxygenation (i.e., hemoglobin concentration, tissue saturation, and redox state of cytochrome c oxidase) in a neonatal piglet model using a hybrid optical technique that combines continuous wave hyperspectral near-infrared spectroscopy (CW *h*-NIRS) and diffuse correlation spectroscopy (DCS). Using a multiplexing shutter approach^{4-6,34} allowed quasi-simultaneously acquisition of CW *h*-NIRS and DCS measurements. The findings of the study support our initial hypothesis that optical measurements of CBF and cerebral oxygenation are sensitive to changes in ICP. Further, it is worth noting that the thickness of the extra-cerebral layers in neonatal piglets measures approximately 2-3 mm⁴⁶, their brain can be examined through the utilization of a source-detector distance exceeding 2 cm. Therefore, source-detector distances of 28 mm for CW *h*-NIRS and 25 mm for DCS were selected in order to investigate the piglet brain while ensuring suitable signal-to-noise ratio.

Although tissue oxygen saturation (StO₂) continue to be widely used a biomarker of cerebral health, its sensitivity to brain injury remains limited²⁴. Consequently, recent advancements in non-invasive neuromonitoring have expanded the scope of cerebral monitoring to include CBF, cerebral metabolism, and oxygenation. Monitoring changes in CBF and metabolism can provide insights into clinically significant changes potentially impacting tissue viability. Moreover, monitoring CBF and StO₂ in response to elevated ICP may aid in determining whether the alterations in hemodynamic parameters reported in previous pilot clinical studies were indeed a result of hydrocephalus-induced high ICP.

The hybrid CW *h*-NIRS/DCS system provided continuous monitoring of cerebral blood flow index (CBFi) with the DCS and using the CW *h*-NIRS to measure changes in the deoxygenated hemoglobin (Hb), oxygenated hemoglobin (HbO₂), the oxidation state of cytochrome c oxidase (oxCCO) and tissue oxygen saturation (StO₂). As anticipated, both the experimental (n=7) and control groups (n=2) showed no significant changes in deoxygenated hemoglobin (Hb), oxygenated hemoglobin (HbO₂), the oxidation state of

cytochrome c oxidase (oxCCO), and CBF during periods of stable, normal ICP (i.e., at the baseline ICP=9±3 mmHg; *Figure 5*). When examining the findings of the control group, it is evident that changes in CBFi were relatively larger compared to other parameters such as Hb, HbO₂, and oxCCO. Additionally, it was observed that DCS data of one of the piglets in the control group exhibited noise. This piglet underwent only 2 experimental runs during DCS measurements, while the other piglet in the control group underwent 6 experimental runs. As a result, the averaged CBFi data for the piglet with fewer experiments were slightly larger and noisier compared to the other parameters. However, despite these minor fluctuations, it is clear that the CBFi values remain constant with the unchanged ICP, similar to the other parameters. This suggests that the variations observed in the CBFi data may be attributed to experimental factors rather than changes in ICP. This finding confirms the stability of the optical measurements under stable physiological conditions, which is consistent with previous studies involving a similar optical neuromonitor^{19,20,30}.

An investigation of the physiological responses to ICP alterations was conducted by directly injecting saline into the ventricle of the piglets in the experimental group. The study findings suggest that increases in ICP, achieved through saline infusion, led to increased Hb and decreases HbO₂. Conversely, oxCCO levels showed a remarkable stability throughout the ICP alteration period (*Figure 6A*). This pattern was consistently observed across all piglets in the experimental group (Appendix A-F). These changes are indicative of a shift in the balance of oxygen delivery and demand, possibly due to reduced CBF as a response to increased ICP as discussed later. The findings are in agreement with previous studies that demonstrated that elevated ICP could result in compromised CBF and subsequent alterations in oxygen availability^{2,5}. On the other hand, oxCCO levels were found to be largely unaltered during changes in ICP. As oxCCO is closely related to the mitochondrial ATP generation in the electron transport chain²⁵, and the stability of oxCCO levels suggests that cerebral energy metabolism remained relatively unchanged despite increased ICP. Additionally, as changes in oxCCO could be associated with metabolic stress, the stability of oxCCO may indicate that changes in ICP did not cause metabolic dysfunction. This aligns with existing literature that has suggested the presence of compensatory mechanisms allowing cerebral energy demands to be sustained even during

reductions in CBF and cerebral oxygenation, possibly through increased oxygen extraction^{5,6}.

Table 2 elucidates the baseline physiological metrics for seven distinct piglets in the experimental group, laying the groundwork for a robust analysis of the impact of any experimental interventions. These baseline figures are of paramount importance as they act as a foundational reference, allowing for a normalized comparison when observing any deviations or alterations in the recorded parameters. The range and standard deviations presented in the table, for metrics such as Hb, HbO₂, oxCCO, StO₂, CBFi, ICP, and CPP, not only convey the inherent variability among the piglets but also highlight the breadth of physiological responses that can be expected within a population.

Figure 6A shows that total hemoglobin (tHb), which is the sum of Hb and HbO₂, remained constant. Although tHb is not shown in the figure, the changes seen in Hb and HbO₂ indicate that tHb has not changed. This constancy is observed despite noted increases in Hb levels and simultaneous decreases in HbO₂ levels, suggesting fluctuations in the hemoglobin components. This interesting observation suggests a compensatory mechanism that prioritizes the maintenance of a stable oxygen-carrying capacity in the bloodstream. Such dynamics indicate that as the level of Hb rises, there is a corresponding decrease in the HbO₂ level, and vice versa. This mutual adjustment ensures that the overall tHb remains unchanged. Even when levels of Hb and HbO₂ show variability, the total potential oxygen-carrying capacity of the blood remains stable⁴⁷. This compensatory mechanism ensures that when there is a surge in the oxygen demand of the blood the metabolism compensates by increasing the amount of oxygen-rich HbO₂. Conversely, when there's ample oxygen or reduced demand, there's a rise in the Hb levels. This constant level of tHb illustrates the body's impressive ability to ensure a steady capacity for oxygen transport, despite changing conditions⁴⁸. The stability of tHb is maintained through various mechanisms. For example, the body can adjust the levels of Hb and HbO₂ to compensate for changes in oxygen demand and supply⁴⁷.

Regulation of cerebral perfusion pressure (CPP) is critical to maintaining CBF and consequently cerebral oxygenation^{21,34,49,50}. High ICP can elicit compensatory responses in

mean arterial pressure (MAP) and CPP. In instances where MAP decreases, compensatory vasodilation takes place, leading to an augmentation in cerebral blood volume and subsequent increasing in ICP⁵¹. Understanding the relationship between ICP and CPP is pivotal in comprehending cerebral autoregulation. Elevated ICP can induce a reduction in CPP, potentially impeding cerebral perfusion^{15,52}. In this study, the correlation of CBFi and StO₂ with CPP was investigated. As shown in *Figure 6B & C*, an important finding from this study was that CPP, CBFi and StO₂ displayed synchronous and rapid changes at the onset and termination of ICP alteration, with increases in ICP leading to decreases in these parameters. Remarkably, changes in CPP, CBFi, and StO₂ displayed nearly identical trends in response to the increasing ICP. This trends were consistent across all piglets in the experimental group as shown in Appendix A-F. A decrease in CPP and CBFi is indicative of the reduced driving force for blood flow and perfusion, respectively, consequent to increased ICP. The simultaneous decrease in StO₂ signifies a reduced oxygen delivery at the tissue level. These three parameters exhibited nearly identical trends in response to the increasing ICP, emphasizing the interplay between ICP, perfusion pressure, blood flow, and tissue oxygenation in maintaining cerebral homeostasis.

The alterations in ICP precipitated rapid and dynamic changes in CPP, CBFi and StO₂. Notably, the experimental findings underscored the distinct individual physiological responses in terms of oxygenation, blood flow, and metabolism (as illustrated in *Figures 6B & C*). These changes emphasize the importance of incorporating all measures - StO₂, hemoglobin concentrations, and CBFi - to attain a comprehensive understanding of the extensive physiological effects of hydrocephalus-induced elevated ICP. Specifically, StO₂, hemoglobin concentrations, and CBF could allow for monitoring of the effects of the elevated ICP with hydrocephalus. Collectively, these different physiological parameters could reflect the cerebral hemodynamics and metabolic environment that precedes brain injury.

The results presented in *Figure 7* and *Figure 8* show regression analysis of all four parameters (ΔHb , ΔHbO_2 , StO₂, ΔCBFi) against ΔCPP during ICP alterations. The analysis showed strong correlations between ΔHb , ΔHbO_2 , StO₂, ΔCBFi , and ΔCPP during ICP alterations. Notably, an increase in ICP was linked with a decrease in ΔCPP , ΔCBFi , and

StO₂ across all piglets in the experimental group (Appendix G-K). Additionally, as Δ CPP decreased during ICP alterations, Δ Hb increased whereas Δ HbO₂, StO₂ and Δ CBFi decreased, exhibiting a similar trend (*Figure 7*). The strong correlations between Δ Hb, Δ HbO₂, StO₂, Δ CBFi and Δ CPP observed during ICP alterations signify that ICP alterations can result in a concurrent and systematic changes in multiple physiological parameters, a relationship that can be harnessed for non-invasive optical neuro-monitoring^{10,31}. Particularly, the strong positive correlation observed between Δ HbO₂, StO₂, and Δ CBFi with Δ CPP and the strong negative correlation between Δ Hb and Δ CPP emphasizes the strong interplay between cerebral blood flow, oxygenation, and perfusion pressure.

Figure 8 provides valuable insights into the relationships between Δ CPP and associated Δ Hb, Δ HbO₂, StO₂, and Δ CBFi. It's noteworthy that Δ Hb and Δ CBFi were found to be closely linked with Δ CPP during ICP alterations. This indicates a significant connection between perfusion pressure, blood volume, and cerebral flow dynamics, underlining the interplay between these key physiological factors in the context of hydrocephalus induced elevated ICP. Interestingly, a delayed but still significant correlation was observed for Δ HbO₂ and StO₂. This implies that changes in oxygenation and tissue saturation may not immediately mirror changes in perfusion pressure, potentially indicating a delay in the brain's metabolic response to altered cerebral blood flow. This delay could be an important factor to consider in clinical settings, as it suggests a window of opportunity for intervention before the onset of irreversible brain injury. To further explore these delayed responses, a cluster analysis of the data was conducted. The analysis divided the data into a cluster representing the delayed response and another cluster that was best fit by a regression line. Further regression analyses were performed on latter cluster (*Figures 7b & c*). This process revealed a strong negative correlation between Δ Hb and Δ CPP and a positive correlation between Δ HbO₂, StO₂, and Δ CBFi with Δ CPP. This outcome is consistent with the findings in *Figure 7*, highlighting the critical links between cerebral perfusion, oxygenation and, blood flow dynamics in the context of hydrocephalus-induced elevated ICP.

In the seven piglets with ICP alterations, the decrease of ΔHbO_2 and changes in StO_2 were delayed in comparison to ΔCBFi (Appendix G-K). Nevertheless, all experiments demonstrated a clear correlation between the decrease in ΔCPP and the changes in ΔHb , ΔCBFi , as well as the delayed responses of ΔHbO_2 or StO_2 . Presumably, the decline in CBF triggers an increase in oxygen extraction as a compensatory mechanism to maintain oxidative metabolism, which aligns with previously reported correlations between elevated ICP and CBF/ StO_2 in infants²¹. This compensatory mechanism may account for the delayed changes observed in HbO_2 and StO_2 responses. Cerebral autoregulation plays a key role in maintaining stable CBF despite fluctuations in CPP^{52,53}. When ICP changes, these autoregulatory mechanisms work to maintain oxygen delivery to brain tissues. Therefore, a delay in the response of oxygenation parameters might reflect the time these mechanisms take to react to changes in CPP. Moreover, the level of HbO_2 in the brain is largely dictated by a delicate balance between the delivery of oxygen and its consumption by brain tissues. Any changes in CPP will first affect the CBF and then, after a certain delay, the oxygen extraction from the blood, and finally the level of HbO_2 ^{54,55}. Oxygen diffusion from blood vessels to brain tissues may also take some time⁵⁴, which is consistent with the delay in ΔHbO_2 and ΔStO_2 responses seen in the study.

Monitoring CPP and CBF is crucial for detecting high ICP and assessing the status of cerebral oxygenation^{56,57}. In the context of preterm infants, monitoring CPP and CBF can be particularly valuable for detecting possible hydrocephalus-induced high ICP. The potential of DCS to estimate the critical closing pressure (CrCP), a parameter directly related to ICP, has been demonstrated in ischemic stroke patients, providing evidence for the use of DCS as a noninvasive method for monitoring CBF and detecting changes in ICP⁵⁹. Applying similar techniques, to monitor CPP and CBF in preterm infants, could help identify early signs of hydrocephalus induced high ICP and guide appropriate interventions to prevent further brain injury. This study investigated the correlation between CPP and CBF during increasing ICP, and *Figure 9* displays the correlation plot between changes in CBF changes and CPP changes during ICP alterations for all piglets in the experimental group. Further, *Table 3* shows the values coefficients of the linear regression and Pearson correlation for *Figure 9*. These findings revealed a strong positive correlation between CPP and CBF, as demonstrated by a regression analysis of 7 piglets (*Figure 9*). The correlation

coefficient yielded a steep slope ($\bar{a} = 1.53 \pm 0.26$), indicating that even slight changes in CPP have a significant impact on CBF, which further substantiates the role of CPP as a vital determinant of CBF. This correlation supports the notion that maintaining an adequate CPP is crucial for ensuring optimal CBF and cerebral oxygenation. The observed increase in CPP with increasing ICP suggests that compensatory mechanisms are activated to maintain CBF in the face of elevated ICP. These findings are consistent with previous research highlighting the critical role of CPP in regulating CBF and underscore the importance of monitoring CBF in clinical practice. By establishing this correlation, our study contributes to the understanding of cerebral hemodynamics and provides valuable insights into the dynamics of cerebral perfusion under conditions of increased ICP. These findings support the notion that continuous monitoring of CPP and CBF is not only essential for detecting high ICP but also holds potential for detecting specific conditions such as hydrocephalus in preterm infants.

The findings of the present study add valuable insights to the body of research utilizing optical techniques, especially the hybrid optical systems, for monitoring cerebral blood flow, metabolism, and oxygenation, particularly in conditions of hydrocephalus induced elevated ICP^{4-6,18,20}. The use of the CW *h*-NIRS and DCS, allowing for non-invasive, continuous, and real-time assessments of vital physiological parameters, could improve neonatal care, particularly in patients with high susceptibility to brain injuries.

In conclusion, this study demonstrates the potential utility of hybrid optical technique (CW *h*-NIRS/DCS) in monitoring high ICP induced alterations in physiological parameters such as CBF and cerebral oxygenation. The findings show that changes in ICP are associated with alterations in the cerebral hemodynamic parameters, as evidenced by the changes in Hb, HbO₂, StO₂, and CBF_i. This could have implications for non-invasive neuromonitoring in clinical settings, particularly in preterm neonates who are highly susceptible to brain injuries. The findings of the present study suggest that CBF and cerebral oxygenation are sensitive to elevated ICP and could be used as early indicators of elevated ICP that may result in brain injury. However, it's worth noting that this study has certain limitations, including use of an animal model. On the other hand, one may question the reliability of the method employed to ascertain the direct infusion of saline into the ventricle, such as

the occurrence of cerebrospinal fluid leakage accompanied by blood during catheter insertion. Nevertheless, the achievement of targeted ICP changes during the study suggests that the saline was successfully administered into the ventricle. For future studies, to enhance the reliability and accuracy of this procedure, it is suggested that an imaging technique be incorporated during the placement of the ventricular catheter. These imaging techniques such as ultrasonography or computed tomography would provide real-time guidance during the catheter placement, confirming that the catheter is correctly inserted into the ventricle and thus ensuring the accuracy of the ICP changes induced by saline infusion. Further, the effect of anesthesia on the hemodynamic parameters and the use of a controlled ICP altering model limits the generalizability of the study. Hence, future work will aim to validate these findings on clinical neonatal populations in the neonatal intensive care units, and explore other factors that could potentially influence these relationships, such as age and other underlying conditions that could compound the effects of high ICP.

2.5 References

1. (CIHI) CI for HI. Giving Birth in Canada. doi:10.12/SORTING/DATETIME-MOMENT.JS
2. McCrea HJ, Ment LR. The Diagnosis, Management and Postnatal Prevention of Intraventricular Hemorrhage in the Preterm Neonate. *Clin Perinatol.* 2008;35(4):777. doi:10.1016/J.CLP.2008.07.014
3. Bassan H. Intracranial hemorrhage in the preterm infant: understanding it, preventing it. *Clin Perinatol.* 2009;36(4):737-762. doi:10.1016/J.CLP.2009.07.014
4. Rajaram A, Bale G, Kewin M, et al. Simultaneous monitoring of cerebral perfusion and cytochrome c oxidase by combining broadband near-infrared spectroscopy and diffuse correlation spectroscopy. *Biomed Opt Express.* 2018;9(6):2588. doi:10.1364/BOE.9.002588
5. Rajaram A, Milej D, Suwalski M, et al. Assessing cerebral blood flow, oxygenation and cytochrome c oxidase stability in preterm infants during the first 3 days after birth. *Scientific Reports 2022 12:1.* 2022;12(1):1-10. doi:10.1038/s41598-021-03830-7
6. Rajaram A, Yip LCM, Milej D, et al. Perfusion and Metabolic Neuromonitoring during Ventricular Taps in Infants with Post-Hemorrhagic Ventricular Dilatation. *Brain Sci.* 2020;10(7):1-13. doi:10.3390/BRAINSCI10070452
7. Simon TD, Riva-Cambrin J, Srivastava R, Bratton SL, Dean JM, Kestle JRW. Hospital care for children with hydrocephalus in the United States: Utilization, charges, comorbidities, and deaths. *J Neurosurg Pediatr.* 2008;1(2):131-137. doi:10.3171/PED/2008/1/2/131
8. El-Dib M, Limbrick DD, Inder T, et al. Management of Post-hemorrhagic Ventricular Dilatation in the Preterm Infant. *J Pediatr.* 2020;226:16. doi:10.1016/J.JPEDI.2020.07.079
9. Klinger G, Osovsky M, Boyko V, et al. Risk factors associated with post-hemorrhagic hydrocephalus among very low birth weight infants of 24–28 weeks gestation. *Journal of Perinatology 2016 36:7.* 2016;36(7):557-563. doi:10.1038/jp.2016.18
10. Kestle JRW. Intraventricular hemorrhage and posthemorrhagic hydrocephalus. *J Neurosurg Pediatr.* 2012;9(3):239-240. doi:10.3171/2011.11.PEDS11412
11. Donnelly J, Czosnyka M, Harland S, et al. Cerebral haemodynamics during experimental intracranial hypertension. *Journal of Cerebral Blood Flow and Metabolism.* 2017;37(2):694-705. doi:10.1177/0271678X16639060
12. Petersen LG, Petersen JCG, Andresen M, Secher NH, Juhler M. Postural influence on intracranial and cerebral perfusion pressure in ambulatory neurosurgical patients. *Am J Physiol Regul Integr Comp Physiol.* 2016;310(1):R100-R104. doi:10.1152/AJPREGU.00302.2015/ASSET/IMAGES/LARGE/ZH60231588780002.JPEG

13. Vella MA, Crandall ML, Patel MB. Acute Management of Traumatic Brain Injury. *Surgical Clinics of North America*. 2017;97(5):1015-1030. doi:10.1016/J.SUC.2017.06.003
14. Nakagawa K, Serrador JM, LaRose SL, Sorond FA. Dynamic cerebral autoregulation after intracerebral hemorrhage: A case-control study. *BMC Neurol*. 2011;11(1):1-8. doi:10.1186/1471-2377-11-108/FIGURES/3
15. Armstead WM. Cerebral Blood Flow Autoregulation and Dysautoregulation. *Anesthesiol Clin*. 2016;34(3):465. doi:10.1016/J.ANCLIN.2016.04.002
16. Ferriero DM. Neonatal brain injury. *N Engl J Med*. 2004;351(19):1985-1995. doi:10.1056/NEJMRA041996
17. Ment LR, Bada HS, Barnes P, et al. Practice parameter: Neuroimaging of the neonate: [RETIRED]. *Neurology*. 2002;58(12):1726-1738. doi:10.1212/WNL.58.12.1726
18. Kishimoto J, Lee DSC, Diop M, Toronov V, Lawrence K St. Development of a combined broadband near-infrared and diffusion correlation system for monitoring cerebral blood flow and oxidative metabolism in preterm infants. *Biomedical Optics Express, Vol 6, Issue 10, pp 3907-3918*. 2015;6(10):3907-3918. doi:10.1364/BOE.6.003907
19. Ko TS, Catennacio E, Shin SS, et al. Advanced Neuromonitoring Modalities on the Horizon: Detection and Management of Acute Brain Injury in Children. *Neurocritical Care* 2023 38:3. 2023;38(3):791-811. doi:10.1007/S12028-023-01690-9
20. Bale G, Mitra S, Tachtsidis I. Metabolic brain measurements in the newborn: Advances in optical technologies. *Physiol Rep*. 2020;8(17). doi:10.14814/PHY2.14548
21. Flanders TM, Lang SS, Ko TS, et al. Optical Detection of Intracranial Pressure and Perfusion Changes in Neonates With Hydrocephalus. *J Pediatr*. 2021;236:54-61.e1. doi:10.1016/J.JPEDS.2021.05.024
22. L H, WB B, D M, et al. Noninvasive continuous optical monitoring of absolute cerebral blood flow in critically ill adults. *Neurophotonics*. 2018;5(4):1. doi:10.1117/1.NPH.5.4.045006
23. Kim MN, Durduran T, Frangos S, et al. Noninvasive measurement of cerebral blood flow and blood oxygenation using near-infrared and diffuse correlation spectroscopies in critically brain-injured adults. *Neurocrit Care*. 2010;12(2):173-180. doi:10.1007/S12028-009-9305-X
24. Boas DA, Franceschini MA. Haemoglobin oxygen saturation as a biomarker: the problem and a solution. *Philos Trans A Math Phys Eng Sci*. 2011;369(1955):4407. doi:10.1098/RSTA.2011.0250
25. Bale G, Elwell CE, Tachtsidis I. From Jöbsis to the present day: a review of clinical near-infrared spectroscopy measurements of cerebral cytochrome-c-oxidase. *J Biomed Opt*. 2016;21(9):091307. doi:10.1117/1.JBO.21.9.091307

26. Bapat R, Narayana PA, Zhou Y, Parikh NA. Magnetic Resonance Spectroscopy at Term-Equivalent Age in Extremely Preterm Infants: Association With Cognitive and Language Development. *Pediatr Neurol.* 2014;51(1):53. doi:10.1016/J.PEDIATRNEUROL.2014.03.011
27. Buckley EM, Parthasarathy AB, Grant PE, Yodh AG, Franceschini MA. Diffuse correlation spectroscopy for measurement of cerebral blood flow: future prospects. *Neurophotonics.* 2014;1(1):011009. doi:10.1117/1.NPH.1.1.011009
28. Tgavalekos K, Sassaroli A, Pham T, Blaney G, Fantini S. Quantitative measurements of cerebral blood flow with near-infrared spectroscopy. *Biomedical Optics Express, Vol 10, Issue 4, pp 2117-2134.* 2019;10(4):2117-2134. doi:10.1364/BOE.10.002117
29. Durduran T, Zhou C, Buckley EM, et al. Optical measurement of cerebral hemodynamics and oxygen metabolism in neonates with congenital heart defects. <https://doi.org/10.1117/13425884>. 2010;15(3):037004. doi:10.1117/1.3425884
30. Durduran T, Yodh AG. Diffuse correlation spectroscopy for non-invasive, microvascular cerebral blood flow measurement. *Neuroimage.* 2014;85(0 1):51. doi:10.1016/J.NEUROIMAGE.2013.06.017
31. Chiarelli AM, Mahmoudzadeh M, Low KA, et al. Assessment of cerebrovascular development and intraventricular hemorrhages in preterm infants with optical measures of the brain arterial pulse wave. *Journal of Cerebral Blood Flow and Metabolism.* 2019;39(3):466-480. doi:10.1177/0271678X17732694/ASSET/IMAGES/LARGE/10.1177_0271678X17732694-FIG6.JPEG
32. Steiner T, Diringner MN, Schneider D, et al. Dynamics of intraventricular hemorrhage in patients with spontaneous intracerebral hemorrhage: Risk factors, clinical impact, and effect of hemostatic therapy with recombinant activated factor VII. *Neurosurgery.* 2006;59(4):767-773. doi:10.1227/01.NEU.0000232837.34992.32
33. Ishiguro A. Perfusion monitoring and intraventricular hemorrhage in preterm infants. *Pediatr Int.* 2017;59(7):759-763. doi:10.1111/PED.13317
34. Rajaram A, Rajaram A, Milej D, et al. Optical monitoring of cerebral perfusion and metabolism in adults during cardiac surgery with cardiopulmonary bypass. *Biomedical Optics Express, Vol 11, Issue 10, pp 5967-5981.* 2020;11(10):5967-5981. doi:10.1364/BOE.404101
35. Mawdsley L. Using Hyperspectral Near-Infrared Spectroscopy and Diffuse Correlation Spectroscopy to Monitor the Effects of Phenylephrine in the Microcirculation. *Electronic Thesis and Dissertation Repository.* Published online September 28, 2021. Accessed June 18, 2023. <https://ir.lib.uwo.ca/etd/8294>
36. Verdecchia Mamadou Diop Ting-Yim Lee Keith St Lawrence K, Verdecchia K, Diop M, Lee TY, St Lawrence K. Quantifying the cerebral metabolic rate of oxygen by combining diffuse correlation spectroscopy and time-resolved near-infrared

- spectroscopy. <https://doi.org/10.1117/1.JBO.18.2.027007>. 2013;18(2):027007. doi:10.1117/1.JBO.18.2.027007
37. Diop M, Verdecchia K, Lee TY, Lawrence KS. Calibration of diffuse correlation spectroscopy with a time-resolved near-infrared technique to yield absolute cerebral blood flow measurements. *Biomed Opt Express*. 2011;2(7):2068. doi:10.1364/BOE.2.002068
 38. O'Donnell JC, Browne KD, Kvint S, et al. Multimodal Neuromonitoring and Neurocritical Care in Swine to Enhance Translational Relevance in Brain Trauma Research. *Biomedicines* 2023, Vol 11, Page 1336. 2023;11(5):1336. doi:10.3390/BIOMEDICINES11051336
 39. Rajaram A. NNeMo (Neonatal NeuroMonitor) - a hybrid optical system to characterize perfusion and metabolism in the newborn brain. *Electronic Thesis and Dissertation Repository*. Published online March 16, 2021. Accessed June 18, 2023. <https://ir.lib.uwo.ca/etd/7677>
 40. Diop M, Wright E, Toronov V, Lee TY, St. Lawrence K. Improved light collection and wavelet de-noising enable quantification of cerebral blood flow and oxygen metabolism by a low-cost, off-the-shelf spectrometer. *J Biomed Opt*. 2014;19(5):057007. doi:10.1117/1.JBO.19.5.057007
 41. Gratton E, Franceschini MA, Fantini S. Semi-infinite-geometry boundary problem for light migration in highly scattering media: a frequency-domain study in the diffusion approximation. *JOSA B, Vol 11, Issue 10, pp 2128-2138*. 1994;11(10):2128-2138. doi:10.1364/JOSAB.11.002128
 42. Jacques SL. Optical properties of biological tissues: a review. *Phys Med Biol*. 2013;58(11). doi:10.1088/0031-9155/58/11/R37
 43. Wyatt JS, Cope M, Delpy DT, et al. Measurement of optical path length for cerebral near-infrared spectroscopy in newborn infants. *Dev Neurosci*. 1990;12(2):140-144. doi:10.1159/000111843
 44. Fantini S, Hueber D, Franceschini MA, et al. Non-invasive optical monitoring of the newborn piglet brain using continuous-wave and frequency-domain spectroscopy. *Phys Med Biol*. 1999;44(6):1543-1563. doi:10.1088/0031-9155/44/6/308
 45. Brun NC, Moen A, Børch K, Saugstad OD, Greisen G. Near-infrared monitoring of cerebral tissue oxygen saturation and blood volume in newborn piglets. *Am J Physiol*. 1997;273(2 Pt 2). doi:10.1152/AJPHEART.1997.273.2.H682
 46. Diop M, Elliott JT, Tichauer KM, Lee TY, St. Lawrence K. A broadband continuous-wave multichannel near-infrared system for measuring regional cerebral blood flow and oxygen consumption in newborn piglets. *Review of Scientific Instruments*. 2009;80(5):54302. doi:10.1063/1.3123347/282427
 47. Jensen FB. Red blood cell pH, the Bohr effect, and other oxygenation-linked phenomena in blood O₂ and CO₂ transport. *Acta Physiol Scand*. 2004;182(3):215-227. doi:10.1111/J.1365-201X.2004.01361.X

48. Ramadan R, Geyer H, Jeka J, Schöner G, Reimann H. A neuromuscular model of human locomotion combines spinal reflex circuits with voluntary movements. *Scientific Reports* 2022 12:1. 2022;12(1):1-23. doi:10.1038/s41598-022-11102-1
49. Mount CA, Das JM. Cerebral Perfusion Pressure. *StatPearls*. Published online April 5, 2022. Accessed June 2, 2023. <https://www.ncbi.nlm.nih.gov/books/NBK537271/>
50. Miller JD, Stanek A, Langfitt TW. Concepts of cerebral perfusion pressure and vascular compression during intracranial hypertension. *Prog Brain Res*. 1972;35(C):411-432. doi:10.1016/S0079-6123(08)60102-8
51. Kim MO, Adji A, O'Rourke MF, et al. Principles of cerebral hemodynamics when intracranial pressure is raised: Lessons from the peripheral circulation. *J Hypertens*. 2015;33(6):1233-1241. doi:10.1097/HJH.0000000000000539
52. Rangel-Castilla L, Gasco J, Nauta HJW, Okonkwo DO, Robertson CS. Cerebral pressure autoregulation in traumatic brain injury. *Neurosurg Focus*. 2008;25(4):E7. doi:10.3171/FOC.2008.25.10.E7
53. Svedung Wettervik T, Fahlström M, Enblad P, Lewén A. Cerebral Pressure Autoregulation in Brain Injury and Disorders—A Review on Monitoring, Management, and Future Directions. *World Neurosurg*. 2022;158:118-131. doi:10.1016/J.WNEU.2021.11.027
54. Masamoto K, Tanishita K. Oxygen transport in brain tissue. *J Biomech Eng*. 2009;131(7). doi:10.1115/1.3184694
55. Patel S, Jose A, Mohiuddin SS. Physiology, Oxygen Transport And Carbon Dioxide Dissociation Curve. *StatPearls*. Published online March 27, 2023. Accessed June 28, 2023. <https://www.ncbi.nlm.nih.gov/books/NBK539815/>
56. Ainslie PN, Duffin J. Integration of cerebrovascular CO₂ reactivity and chemoreflex control of breathing: mechanisms of regulation, measurement, and interpretation. *Am J Physiol Regul Integr Comp Physiol*. 2009;296(5). doi:10.1152/AJPREGU.91008.2008
57. Svedung Wettervik T, Howells T, Lewén A, Ronne-Engström E, Enblad P. Temporal Dynamics of ICP, CPP, PRx, and CPPopt in High-Grade Aneurysmal Subarachnoid Hemorrhage and the Relation to Clinical Outcome. *Neurocrit Care*. 2021;34(2):390-402. doi:10.1007/S12028-020-01162-4/TABLES/3
58. Bragin DE, Bush RC, Müller WS, Nemoto EM. High Intracranial Pressure Effects on Cerebral Cortical Microvascular Flow in Rats. <https://home.liebertpub.com/neu>. 2011;28(5):775-785. doi:10.1089/NEU.2010.1692
59. Wu KC, Sunwoo J, Sheriff F, et al. Validation of diffuse correlation spectroscopy measures of critical closing pressure against transcranial Doppler ultrasound in stroke patients. <https://doi.org/10.1117/1JBO263036008>. 2021;26(3):036008. doi:10.1117/1.JBO.26.3.036008

Chapter 3

3 Conclusions

This concluding chapter offers a review of the thesis's objectives and encapsulates the key findings of the study. It also highlights the study's limitations while suggesting potential remedies. Furthermore, this chapter explores the possible implications of these results and delves into discussions on prospective research avenues.

3.1 Research Objectives

Prematurely born infants, defined as those born before 37 weeks of gestational age, have a higher chance of developing neurological complications^{1,2}. The extent of this risk is directly proportionate to the brevity of the gestation period and the birth weight of the infant³. Clinical studies have shown that the underdeveloped cerebral vascular system in premature infants, particularly those with very low birth weights (VLBW, < 1500 g), is prone to alterations in cerebral blood flow (CBF)². This vulnerability, compounded by birth-related complications, increases the risk of intraventricular hemorrhage (IVH)⁴. IVH, characterized by bleeding into cerebral ventricles, has a prevalence of 15-20% in VLBW infants within the first 72 hours of life and this is due to poor cerebral autoregulation and susceptibility to hemodynamic instability. These instabilities hinder appropriate cerebral blood flow and oxygenation, leading to potential brain injuries³. IVH often leads to hydrocephalus, an abnormal cerebral spinal fluid (CSF) build-up in the brain that elevates intracranial pressure (ICP), further increasing the risk of brain injuries⁵.

High ICP can have compensatory effects on mean arterial pressure (MAP) and cerebral perfusion pressure (CPP). CPP refers to the pressure gradient responsible for accelerating blood flow within the cerebral circulation to the brain and is calculated by subtracting ICP from MAP⁶. When MAP is reduced, compensatory vasodilation occurs, leading to an increase in cerebral blood volume and ICP^{7,8}. The relationship between ICP and CPP is important in understanding cerebral autoregulation. Higher ICP can lead to a reduction in CPP, which may impair cerebral autoregulation⁹. While ICP monitoring is important, CPP is considered a better marker for monitoring high ICP. Therefore, the primary focus in

managing hydrocephalus induced high ICP is active control of ICP. Currently, cranial ultrasound (cUS) is the standard non-invasive technique for diagnosing hydrocephalus¹⁰. However, its scope is limited as it can mainly identify and assess pre-existing injury, constraining its predictive capabilities. Furthermore, its ability to provide continuous, longitudinal monitoring is limited.

Biomedical optics currently provides cost-effective brain monitoring and early identification of hemodynamic and metabolic abnormalities that might cause brain injury^{4,5,11}. These optical methods provide real-time, non-invasive brain physiological parameter monitoring. These novel methods quantify cerebral hemodynamics including blood flow and oxygenation and monitor brain metabolism using light-tissue interaction^{1,12,13}. Continuous wave hyperspectral near-infrared spectroscopy (CW *h*-NIRS) capitalizes on the light absorption characteristics of tissue constituents such as oxygenated and deoxygenated hemoglobin (HbO₂ and Hb, respectively) as potential precursor biomarkers for preterm brain injury¹⁴. Further, CW *h*-NIRS can directly assess cerebral oxidative metabolism by observing alterations in the redox state of cytochrome c oxidase (oxCCO), a parameter can provide insights into the metabolic state of cells and tissues¹⁵. Diffuse correlation spectroscopy (DCS) can provide continuously monitoring CBF using near-infrared light to quantify red blood cell dynamic light scatter¹⁶.

The focus of this study was to employ a hybrid CW *h*-NIRS/DCS system to investigate the effect of increased ICP on CBF and cerebral oxygenation. The main goal of this thesis was to test the sensitivity of optical measures of CBF and oxygenation to elevated ICP in a neonatal piglet model of elevated ICP, which was achieved through two primary objectives:

3. Demonstrate the impact of elevated ICP on CBF and cerebral oxygenation.
4. Investigate the correlation between CPP, CBF and tissue saturation during ICP alterations.

3.2 Summary of Chapter 2: Assessing the Sensitivity of Cerebral Blood Flow and Oxygenation to High Intracranial Pressure with Near-Infrared Light

In this study presented in Chapter 2, the hypothesis that optical measurements of CBF and oxygenation will show high sensitivity to ICP was tested using the hybrid optical device (CW *h*-NIRS/DCS) in nine neonatal piglets, which included two animals for control group and seven animals for experimental group. The study reports no significant changes in Hb, HbO₂, oxCCO, and CBF at the baseline ICP level. However, during increased ICP, there were increases in Hb and decreases in HbO₂, indicating a shift in oxygen availability due to a potential reduction in CBF. Interestingly, the levels of oxCCO remained largely unaltered, suggesting that cerebral energy metabolism was not significantly affected by increased ICP to cause metabolic stress. The data further showed that increases in ICP led to decreases in CPP, CBF_i, and StO₂, highlighting the link between these physiological factors in maintaining cerebral homeostasis. Significant correlations were found between Δ Hb, Δ HbO₂, StO₂, Δ CBF_i, and Δ CPP during ICP alterations. An increase in ICP was associated with a decrease in CPP, CBF_i, and StO₂, and an increase in Hb, indicating that ICP changes can concurrently affect multiple physiological parameters. Notably, changes in HbO₂ and StO₂ were observed to occur with a delay compared to CPP changes, indicating a potential delay in the brain's metabolic response to altered blood flow. This delay could represent a window of opportunity for intervention before irreversible brain injury. Furthermore, the study revealed a strong positive correlation between CPP and CBF during ICP alterations across all piglets in the experimental group. The data shows that even slight shifts in CPP significantly impact CBF, highlighting the importance of CPP in managing CBF. It also suggests that the body employs compensatory mechanisms to maintain CBF during elevated ICP. This reaffirms the crucial role of CPP monitoring in clinical scenarios. Overall, this study demonstrates that optical measures of CBF and oxygenation are sensitive to elevated ICP. The findings underscore the potential of non-invasive hybrid optical techniques for real-time assessment of these critical parameters to improve detection and intervention in cases of hydrocephalus induced high ICP.

3.3 Limitations and Future Directions

Although the results of the study provide valuable insights into the potential of non-invasive optical neuromonitoring of cerebral oxygenation, and metabolism in neonatal animal model using the hybrid optical device, it is important to acknowledge its limitations. Our sample size, while sufficient for an initial finding of these relationships, was relatively small. The composition of our sample size lacked homogeneity, particularly when it came to factors such as sex and age, making our sample size unbalanced. Due to this unbalanced demographic distribution, we were unable to delve deeper into potential influential factors such as sex and age characteristics on our measurements. The conclusions and insights derived from a small cohort may not be representative of broader populations or biological diversity. As a future direction, it is thought to expand the sample size in subsequent investigations, piglet to resource availability.

This research employed a shutter multiplexing system in conjunction with the CW *h*-NIRS and DCS setup to circumvent issues of signal crosstalk. As a result, data collection from both subsystems didn't occur concurrently, but rather sequentially. During the data processing, the process of separating data, specifically at those instances when the shutters were fully open and fully closed, brought about a reduction in our sampling rate. This means that we gathered data at a slower pace than initially anticipated. The sampling rate is essential because it dictates how frequently we record data, and a higher rate generally provides a more detailed representation of the events we're studying. Nevertheless, this decrease in sampling rate wasn't entirely disadvantageous. Despite the slower pace, we could reliably capture low-frequency data.

ICP alteration in the neonatal piglet model included the use of anesthesia with isoflurane and propofol during the preparatory surgery. Furthermore, a low CRI of propofol was administered and reduced rate of isoflurane was continued during ICP alterations. Isoflurane, a commonly used anesthetic agent, has been shown to have dose-dependent effects on cerebral physiology, including CBF, blood pressure, heart rate, and cerebral metabolism¹⁷. On the other hand, propofol anesthesia has been associated with reduced cerebral blood flow, which has been attributed to reductions in cerebral metabolism and neurovascular coupling¹⁸. The fact that the use of isoflurane and propofol during anesthesia

and ICP alterations effect cerebral metabolism, cerebral blood flow, and oxygenation in animal models, and the sudden changes and fluctuations observed in some data during ICP alterations could be attributed to the effects of anesthesia. Future studies should carefully consider the effects of anesthetic drugs.

One potential limitation in this study was the inherent sensitivity of the hybrid optical device to external light. To mitigate this, experiments were conducted under blackout covers, ensuring that the data collected remained undisturbed by any environmental light. However, during the experiments, routine half-hour blood samples were taken to monitor physiological variables, such as blood gas levels and glucose. This necessitated the removal of the light-blocking cover, particularly when accessing catheters positioned near the ears of the piglets, thereby exposing the detector of the device to external ambient light. Consequently, this could have introduced fluctuations and possible inaccuracies in some of the collected datasets. Future direction could be the development of alternative methods for physiological monitoring that do not require the frequent collection of blood samples, thereby reducing the need to disturb the controlled light conditions.

Another potential limitation was associated with the technique of altering ICP using a syringe pump connected to an intraventricular catheter to inject saline directly into the ventricle. While the pump's rate was typically set at 0.2 ml/min for most piglets, the actual time taken for ICP changes to manifest varied across different piglets due to inter-piglet variability. As a result, the saline infusion rate had to be increased for certain piglets when no immediate ICP changes were observed. This occasionally resulted in abrupt ICP changes, at which point the saline infusion was stopped to avoid excessive fluctuation in ICP. Consequently, this may have contributed to inconsistent ICP changes in some runs. For future studies, the application of adaptive control systems, which adjust the rate of saline infusion in real time based on monitored ICP changes, could provide more consistent and smooth alterations of ICP. By addressing this limitation, the study could lead to improved accuracy in ICP alterations, contributing to more reliable and reproducible experimental results.

The use of an animal model, while instrumental in allowing controlled alterations of ICP, may not fully capture the complex interplay of factors present in preterm infants suffering from conditions leading to elevated ICP. Translation of these findings to clinical practice will require validation in a more diverse preterm infants cohort. In view of this limitation, the findings from this animal model study need to be replicated and validated in preterm infant populations to enhance their translatability. Given the complexities involved in neonatal care and the unique physiological responses seen in preterm infants, cerebral hemodynamics, oxygenation, and cerebral blood flow alterations need to be explored further in clinical settings. This will help establish the validity and utility of these parameters as sensitive biomarkers in preterm infants with conditions leading to hydrocephalus induced-elevated ICP.

3.4 Conclusion

To conclude, this study provides new insights into the sensitive interplay between cerebral blood flow, oxygenation, and high intracranial pressure as measured by an innovative hybrid optical device which combined both continuous-wave hyperspectral near-infrared spectroscopy (CW *h*-NIRS) and diffuse correlation spectroscopy (DCS). It sheds light specifically on the impact of these dynamics in a neonatal animal model of high ICP.

The hybrid CW *h*-NIRS/DCS technology offers a unique, cutting-edge method to simultaneously monitor important hemodynamic parameters. As evidenced in this research, it serves as an invaluable tool for continuous *in vivo* monitoring, providing real-time insights into the physiological changes occurring in the preterm infants' brain during increased ICP. The findings from this research highlight the sensitivity of cerebral blood flow and oxygenation to increases in ICP. These findings potentially pave the way for early detection of elevated ICP that could lead to brain injury, thereby enabling timely intervention. Given its non-invasive nature, safety, and portability, the hybrid CW *h*-NIRS/DCS system could be conveniently employed for bedside monitoring in a neonatal setting, particularly for preterm infants^{5,11,19}. The system is capable of detecting critical alterations in cerebral metabolism, oxygenation, and blood flow immediately following

birth. It holds promise for identifying signs of high ICP, including conditions such as hydrocephalus.

This study, therefore, not only propels the understanding of neonatal cerebral hemodynamics under high ICP but also provides a promising tool for early detection and prevention of related brain injuries. Future research will extend the use of the hybrid CW *h*-NIRS/DCS system to a wider and more diverse cohort, including preterm infants, to further validate and optimize its potential for clinical applications.

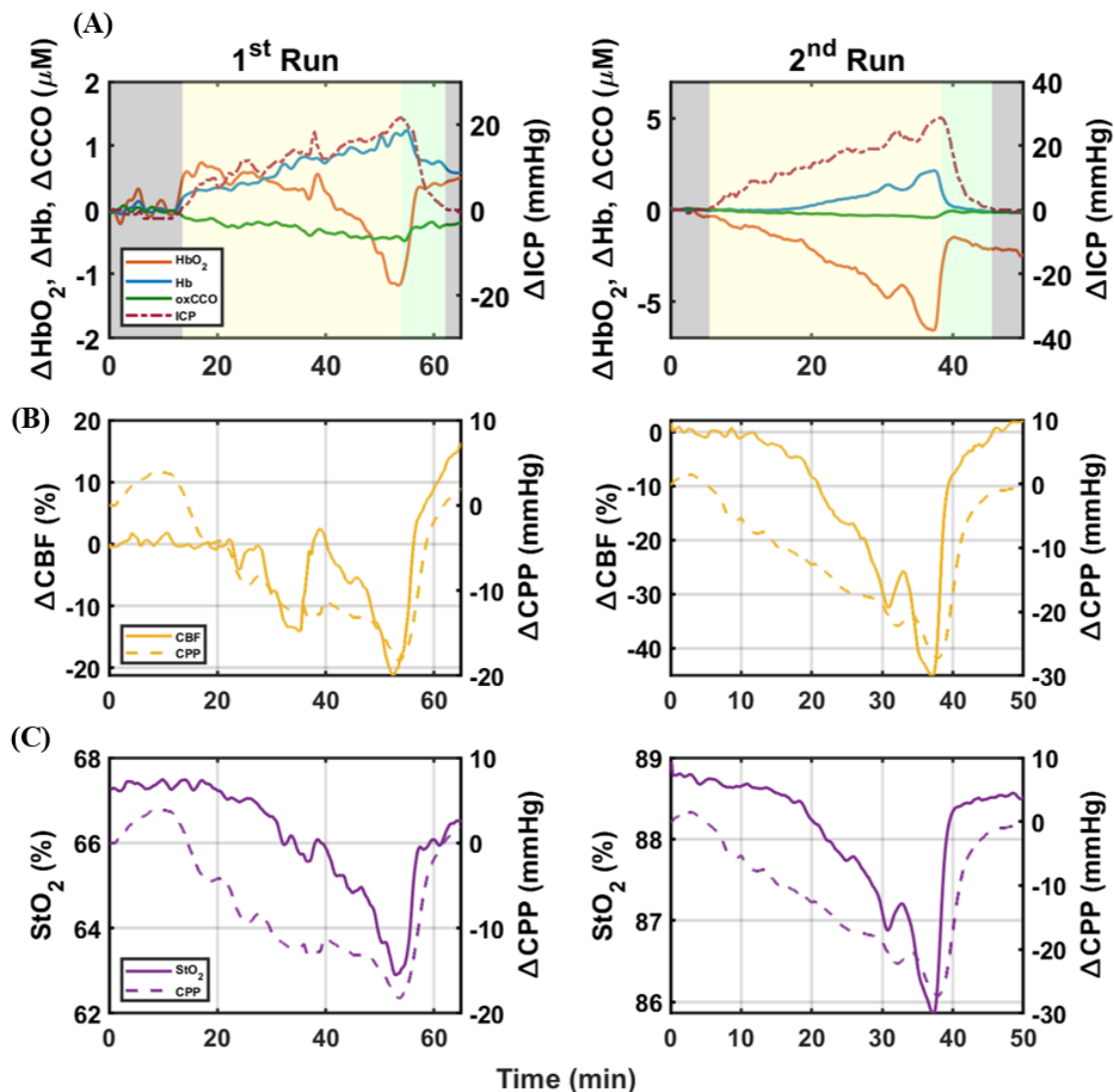
3.5 References

1. Flanders TM, Lang SS, Ko TS, et al. Optical Detection of Intracranial Pressure and Perfusion Changes in Neonates With Hydrocephalus. *J Pediatr.* 2021;236:54-61.e1. doi:10.1016/J.JPEDI.2021.05.024
2. McCrea HJ, Ment LR. The Diagnosis, Management and Postnatal Prevention of Intraventricular Hemorrhage in the Preterm Neonate. *Clin Perinatol.* 2008;35(4):777. doi:10.1016/J.CLP.2008.07.014
3. Bassan H. Intracranial hemorrhage in the preterm infant: understanding it, preventing it. *Clin Perinatol.* 2009;36(4):737-762. doi:10.1016/J.CLP.2009.07.014
4. Rajaram A, Bale G, Kewin M, et al. Simultaneous monitoring of cerebral perfusion and cytochrome c oxidase by combining broadband near-infrared spectroscopy and diffuse correlation spectroscopy. *Biomed Opt Express.* 2018;9(6):2588. doi:10.1364/BOE.9.002588
5. Rajaram A, Yip LCM, Milej D, et al. Perfusion and Metabolic Neuromonitoring during Ventricular Taps in Infants with Post-Hemorrhagic Ventricular Dilatation. *Brain Sci.* 2020;10(7):1-13. doi:10.3390/BRAINSCI10070452
6. Vella MA, Crandall ML, Patel MB. Acute Management of Traumatic Brain Injury. *Surgical Clinics of North America.* 2017;97(5):1015-1030. doi:10.1016/J.SUC.2017.06.003
7. Oddo M, Crippa IA, Mehta S, et al. Optimizing sedation in patients with acute brain injury. *Crit Care.* 2016;20(1):1-11. doi:10.1186/S13054-016-1294-5/FIGURES/1
8. Armstead WM. Cerebral Blood Flow Autoregulation and Dysautoregulation. *Anesthesiol Clin.* 2016;34(3):465. doi:10.1016/J.ANCLIN.2016.04.002
9. Nakagawa K, Serrador JM, LaRose SL, Sorond FA. Dynamic cerebral autoregulation after intracerebral hemorrhage: A case-control study. *BMC Neurol.* 2011;11(1):1-8. doi:10.1186/1471-2377-11-108/FIGURES/3
10. Ment LR, Bada HS, Barnes P, et al. Practice parameter: Neuroimaging of the neonate: [RETIRED]. *Neurology.* 2002;58(12):1726-1738. doi:10.1212/WNL.58.12.1726
11. Rajaram A, Milej D, Suwalski M, et al. Assessing cerebral blood flow, oxygenation and cytochrome c oxidase stability in preterm infants during the first 3 days after birth. *Scientific Reports 2022 12:1.* 2022;12(1):1-10. doi:10.1038/s41598-021-03830-7
12. L H, WB B, D M, et al. Noninvasive continuous optical monitoring of absolute cerebral blood flow in critically ill adults. *Neurophotonics.* 2018;5(4):1. doi:10.1117/1.NPH.5.4.045006
13. Bale G, Mitra S, Tachtsidis I. Metabolic brain measurements in the newborn: Advances in optical technologies. *Physiol Rep.* 2020;8(17). doi:10.14814/PHY2.14548

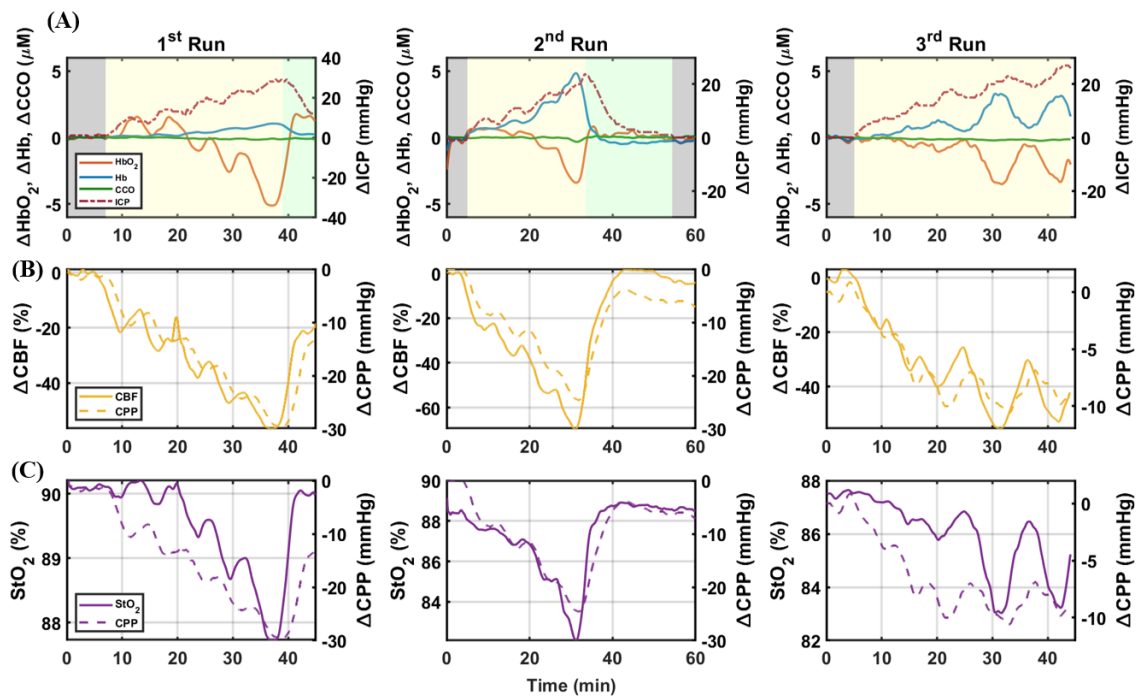
14. Boas DA, Franceschini MA. Haemoglobin oxygen saturation as a biomarker: the problem and a solution. *Philos Trans A Math Phys Eng Sci.* 2011;369(1955):4407. doi:10.1098/RSTA.2011.0250
15. Bale G, Elwell CE, Tachtsidis I. From Jöbsis to the present day: a review of clinical near-infrared spectroscopy measurements of cerebral cytochrome-c-oxidase. *J Biomed Opt.* 2016;21(9):091307. doi:10.1117/1.JBO.21.9.091307
16. Buckley EM, Parthasarathy AB, Grant PE, Yodh AG, Franceschini MA. Diffuse correlation spectroscopy for measurement of cerebral blood flow: future prospects. *Neurophotonics.* 2014;1(1):011009. doi:10.1117/1.NPH.1.1.011009
17. Li CX, Zhang X. Effects of Long-Duration Administration of 1% Isoflurane on Resting Cerebral Blood Flow and Default Mode Network in Macaque Monkeys. <https://home.liebertpub.com/brain>. 2017;7(2):98-105. doi:10.1089/BRAIN.2016.0445
18. Skytjoti M, Elstad M, Søvik S. Internal Carotid Artery Blood Flow Response to Anesthesia, Pneumoperitoneum, and Head-up Tilt during Laparoscopic Cholecystectomy. *Anesthesiology.* 2019;131(3):512-520. doi:10.1097/ALN.0000000000002838
19. Rajaram A, Rajaram A, Milej D, et al. Optical monitoring of cerebral perfusion and metabolism in adults during cardiac surgery with cardiopulmonary bypass. *Biomedical Optics Express, Vol 11, Issue 10, pp 5967-5981.* 2020;11(10):5967-5981. doi:10.1364/BOE.404101

Appendices

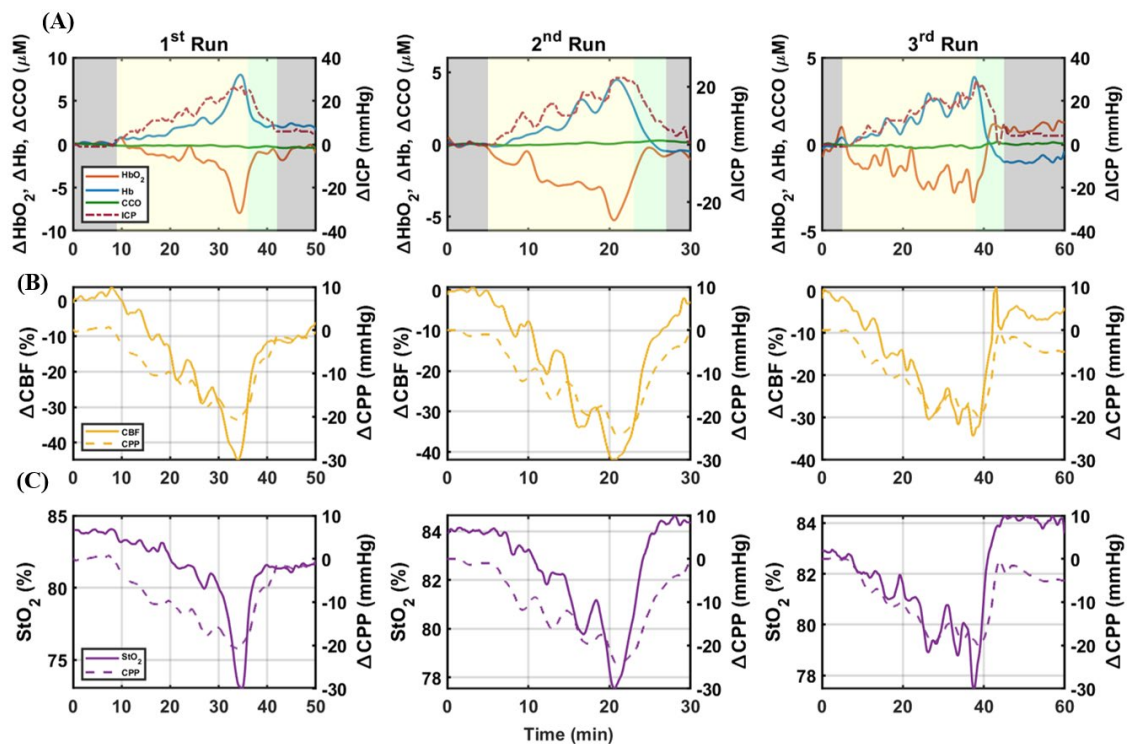
Appendix A: (A) Time dependent changes in ΔHb , ΔHbO_2 and ΔoxCCO with ΔICP from second piglet in the experimental group (E2) for the two runs. The orange lines represent ΔHbO_2 , the blue lines represent ΔHb , the green lines represent ΔoxCCO in μM , and the dark red lines represent ΔICP in mmHg. In panel (A), the grey box illustrates the baseline ICP period, the yellow box illustrates the increased ICP period, and the green box illustrates the decreased ICP period. (B) and (C) Time-dependent changes in ΔCBFi and StO_2 with changes in CPP (ΔCPP) from same piglet (E2) for two runs in (%), respectively.



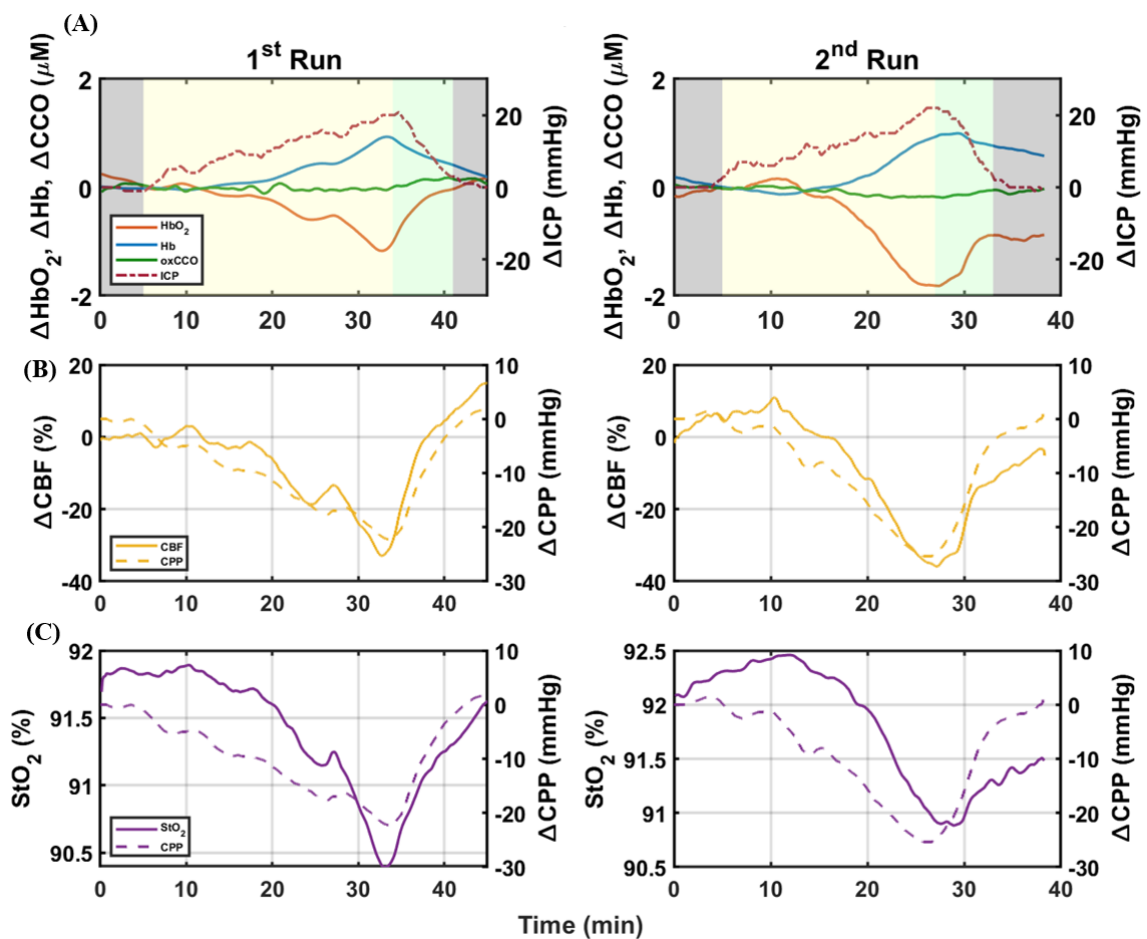
Appendix B: (A) Time dependent changes in ΔHb , ΔHbO_2 and ΔoxCCO with ΔICP from third piglet in the experimental group (E3) for the three runs. The orange lines represent ΔHbO_2 , the blue lines represent ΔHb , the green lines represent ΔoxCCO in μM , and the dark red lines represent ΔICP in mmHg. In panel (A), the grey box illustrates the baseline ICP period, the yellow box illustrates the increased ICP period, and the green box illustrates the decreased ICP period. (B) and (C) Time-dependent changes in ΔCBFi and StO_2 with changes in CPP (ΔCPP) from same piglet (E3) for three runs in (%), respectively.



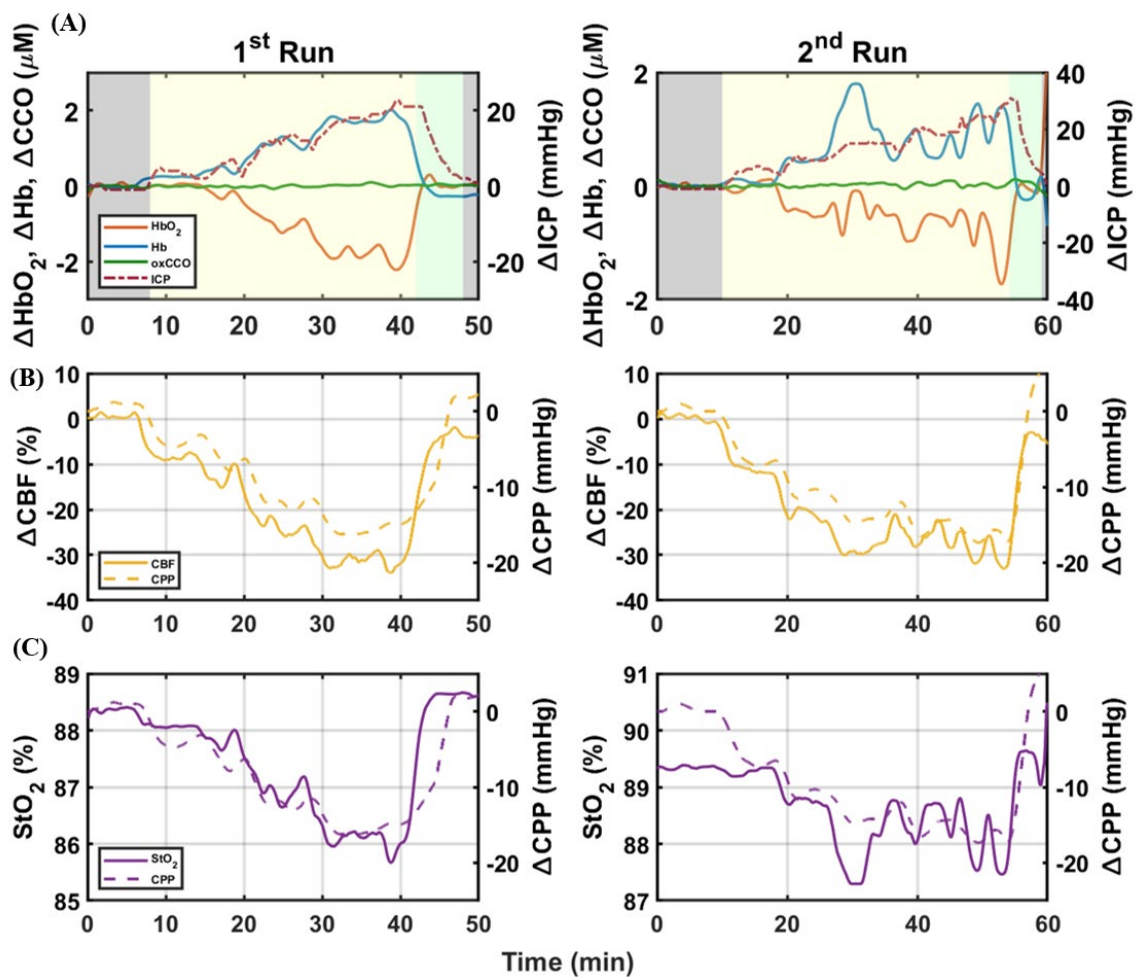
Appendix C: (A) Time dependent changes in ΔHb , ΔHbO_2 and ΔoxCCO with ΔICP from fourth piglet in the experimental group (E4) for the three runs. The orange lines represent ΔHbO_2 , the blue lines represent ΔHb , the green lines represent ΔoxCCO in μM , and the dark red lines represent ΔICP in mmHg. In panel (A), the grey box illustrates the baseline ICP period, the yellow box illustrates the increased ICP period, and the green box illustrates the decreased ICP period. (B) and (C) Time-dependent changes in ΔCBFi and StO_2 with changes in CPP (ΔCPP) from same piglet (E4) for three runs in (%), respectively.



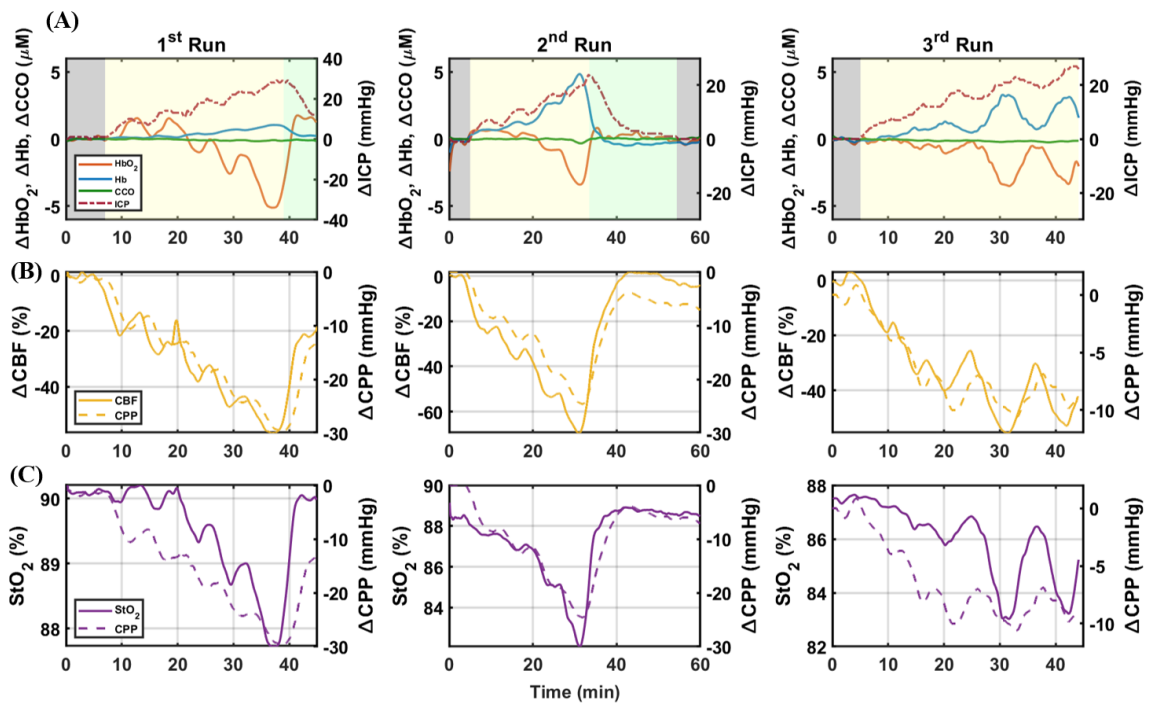
Appendix D: (A) Time dependent changes in ΔHb , ΔHbO_2 and ΔoxCCO with ΔICP from fifth piglet in the experimental group (E5) for the two runs. The orange lines represent ΔHbO_2 , the blue lines represent ΔHb , the green lines represent ΔoxCCO in μM , and the dark red lines represent ΔICP in mmHg. In panel (A), the grey box illustrates the baseline ICP period, the yellow box illustrates the increased ICP period, and the green box illustrates the decreased ICP period. (B) and (C) Time-dependent changes in ΔCBFi and StO_2 with changes in CPP (ΔCPP) from same piglet (E5) for two runs in (%), respectively.



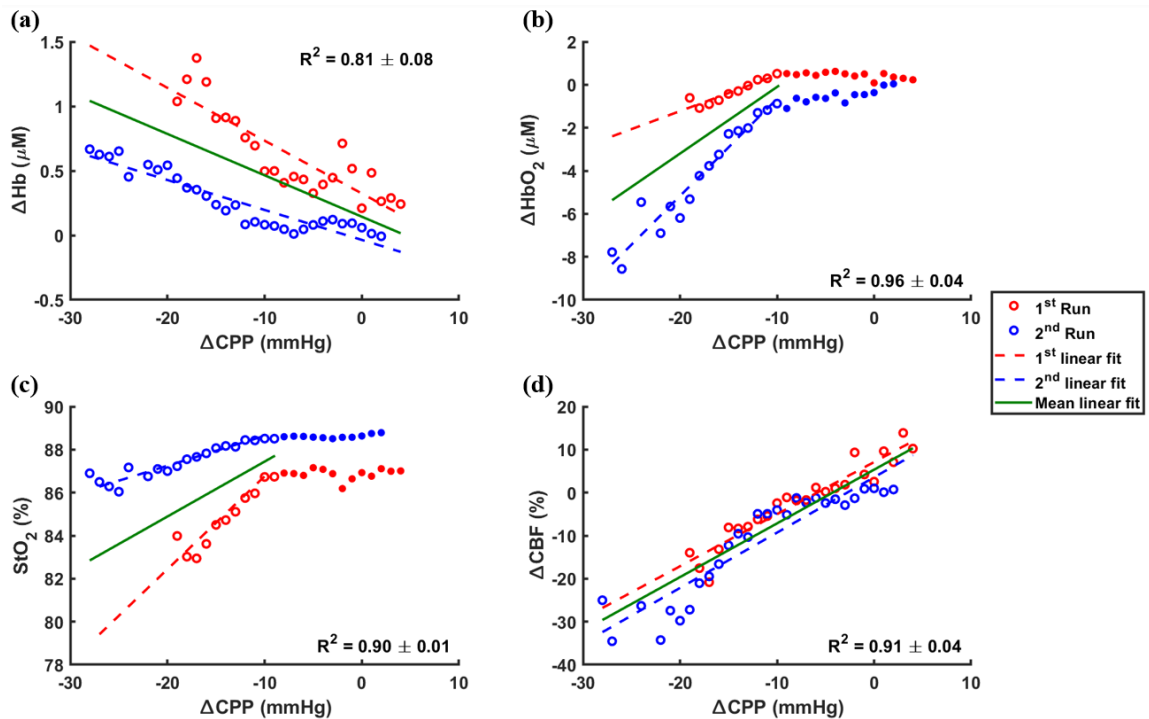
Appendix E: (A) Time dependent changes in ΔHb , ΔHbO_2 and ΔoxCCO with ΔICP from sixth piglet in the experimental group (E6) for the two runs. The orange lines represent ΔHbO_2 , the blue lines represent ΔHb , the green lines represent ΔoxCCO in μM , and the dark red lines represent ΔICP in mmHg. In panel (A), the grey box illustrates the baseline ICP period, the yellow box illustrates the increased ICP period, and the green box illustrates the decreased ICP period. (B) and (C) Time-dependent changes in ΔCBFi and StO_2 with changes in CPP (ΔCPP) from same piglet (E6) for two runs in (%), respectively.



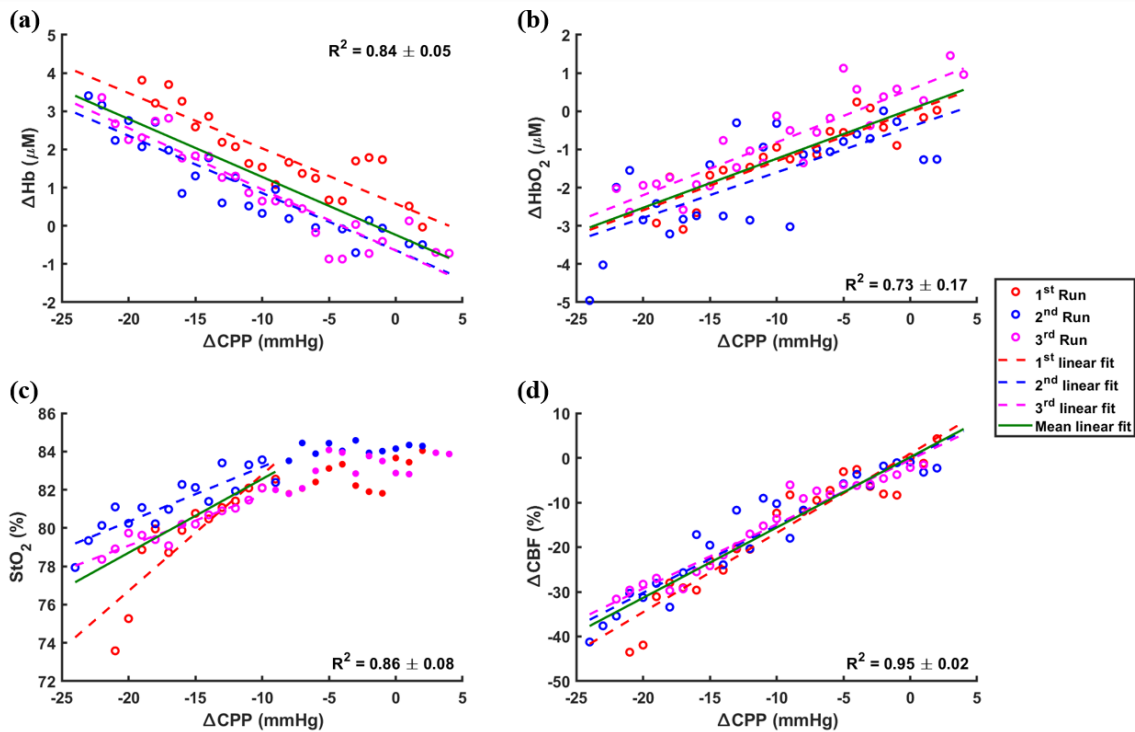
Appendix F: (A) Time dependent changes in ΔHb , ΔHbO_2 and ΔoxCCO with ΔICP from seventh piglet in the experimental group (E7) for the two runs. The orange lines represent ΔHbO_2 , the blue lines represent ΔHb , the green lines represent ΔoxCCO in μM , and the dark red lines represent ΔICP in mmHg. In panel (A), the grey box illustrates the baseline ICP period, the yellow box illustrates the increased ICP period, and the green box illustrates the decreased ICP period. (B) and (C) Time-dependent changes in ΔCBFi and StO_2 with changes in CPP (ΔCPP) from same piglet (E7) for two runs in (%), respectively.



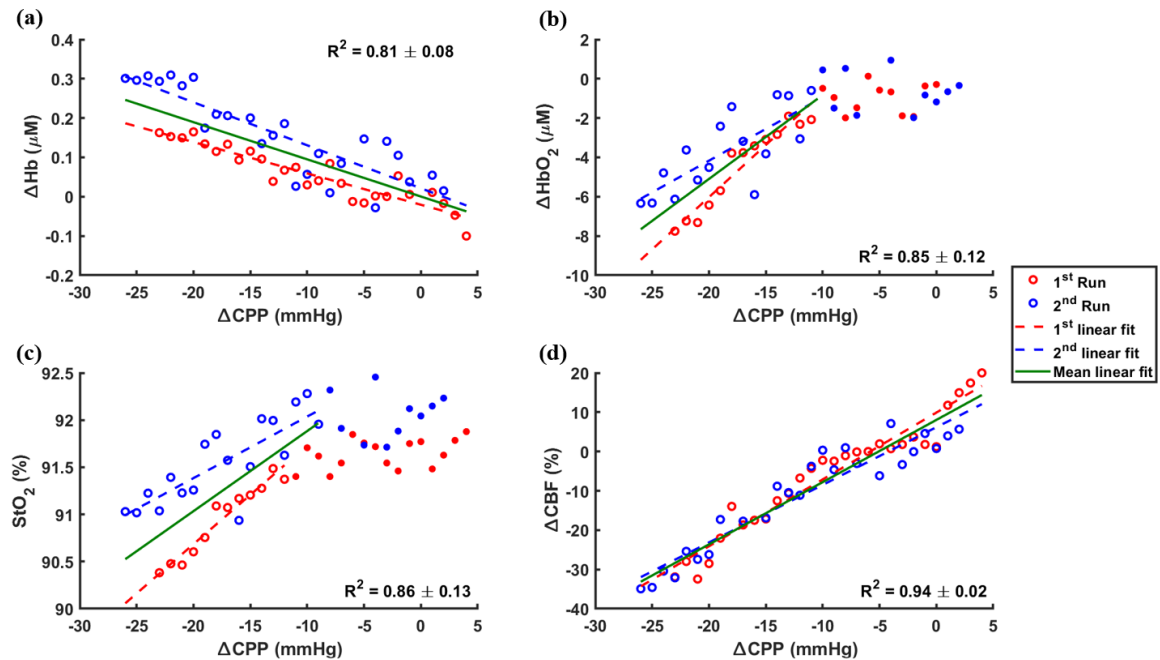
Appendix G: Correlation plots of (a) ΔHb vs ΔCPP , (b) ΔHbO_2 vs ΔCPP , (c) StO_2 vs ΔCPP , (d) ΔCBFi vs ΔCPP for second piglet (E2) mean values for all runs; indicates significant correlations for ΔHb and ΔCBFi and significant correlations with delaying for ΔHbO_2 and StO_2 . The filled scatter dots represent the delaying clusters' data points. The dashed lines represent the regression line, the solid green lines represent mean fitted linear line for all runs ($p < 0.05$, $R^2 > 0.90 \pm 0.06$).



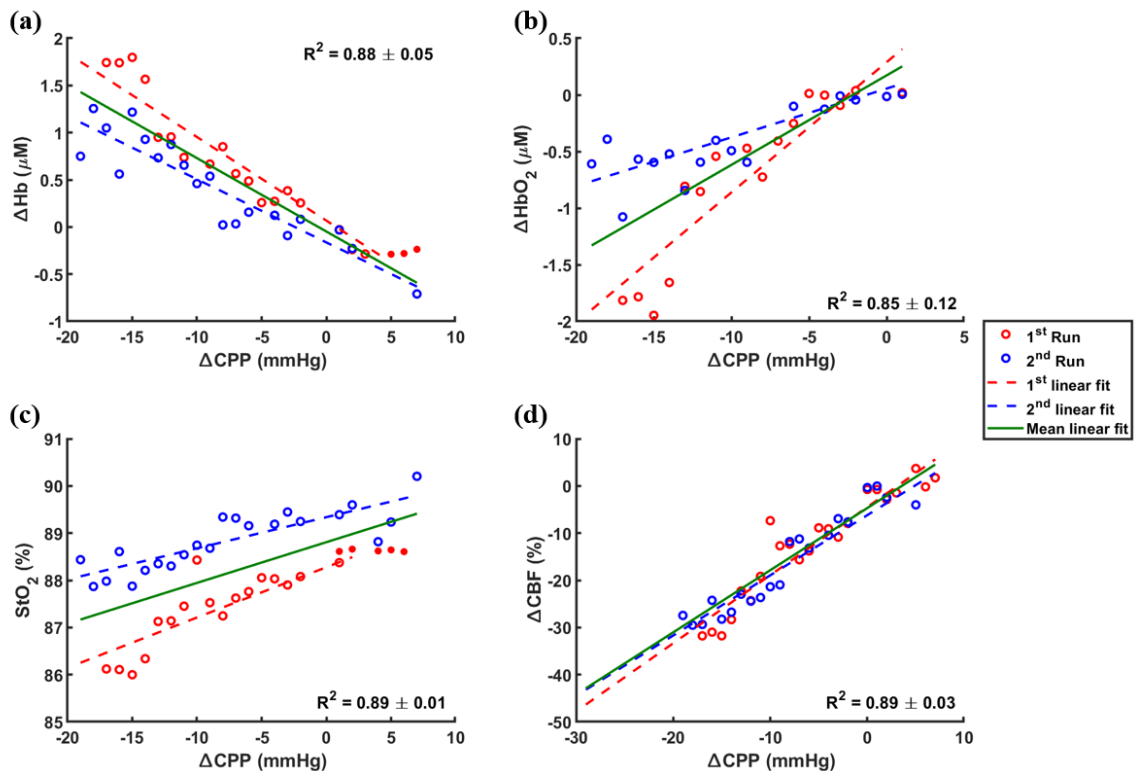
Appendix H: Correlation plots of (a) ΔHb vs ΔCPP , (b) ΔHbO_2 vs ΔCPP , (c) StO_2 vs ΔCPP , (d) ΔCBFi vs ΔCPP for fourth piglet (E4) mean values for all runs; indicates significant correlations for ΔHb and ΔCBFi and significant correlations with delaying for ΔHbO_2 and StO_2 . The filled scatter dots represent the delaying clusters' data points. The dashed lines represent the regression line, the solid green lines represent mean fitted linear line for all runs ($p < 0.05$, $R^2 > 0.85 \pm 0.09$).



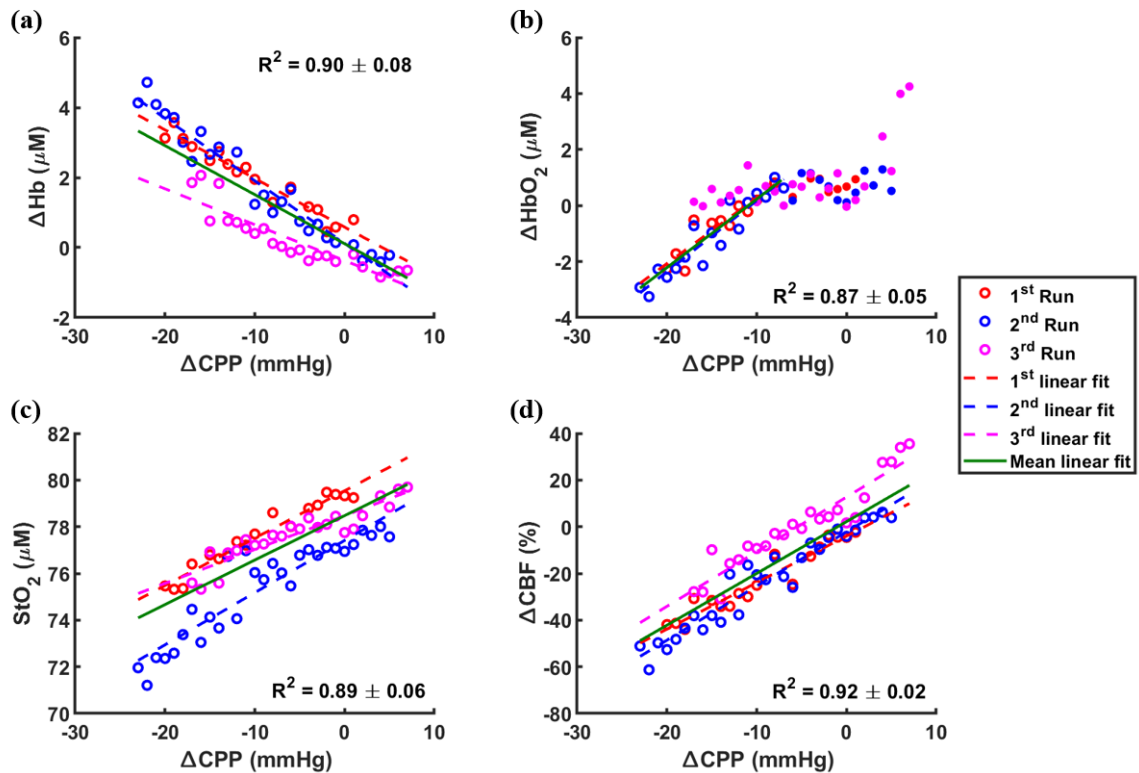
Appendix I: Correlation plots of (a) ΔHb vs ΔCPP , (b) ΔHbO_2 vs ΔCPP , (c) ΔStO_2 vs ΔCPP , (d) ΔCBFi vs ΔCPP for fifth piglet (E5) mean values for all runs; indicates significant correlations for ΔHb and ΔCBFi and significant correlations with delaying for ΔHbO_2 and StO_2 . The filled scatter dots represent the delaying clusters' data points. The dashed lines represent the regression line, the solid green lines represent mean fitted linear line for all runs ($p < 0.05$, $R^2 > 0.87 \pm 0.09$).



Appendix J: Correlation plots of ΔHb vs ΔCPP , ΔHbO_2 vs ΔCPP , StO_2 vs ΔCPP , ΔCBFi vs ΔCPP for seventh piglet (E6) mean values for all runs: ΔHb vs ΔCPP , ΔHbO_2 vs ΔCPP , StO_2 vs ΔCPP , ΔCBFi vs ΔCPP for sixth piglet (E6) mean value for all runs. The dashed lines represent the best fit of regression line, the solid green lines represent mean fitted linear line for all runs ($p < 0.05$, $R^2 > 0.88 \pm 0.02$).



Appendix K: Correlation plots of ΔHb vs ΔCPP , ΔHbO_2 vs ΔCPP , StO_2 vs ΔCPP , ΔCBFi vs ΔCPP for seventh piglet (E7) mean values for all runs; indicates significant correlations for ΔHb , StO_2 and ΔCBFi , and significant correlations with delaying for ΔHbO_2 . The filled scatter dots represent the delaying clusters' data points. The dashed lines represent the regression line, the solid green lines represent mean fitted linear line for all runs ($p < 0.05$, $R^2 > 0.90 \pm 0.02$).



Curriculum Vitae

- Name:** Sule Karagulleoglu-Kunduraci
- Post-secondary Education and Degrees:** Hacettepe University, Physics Engineering
Ankara, Turkey
2009-2014 B.Sc.
- Hacettepe University, Bioengineering
Ankara, Turkey
2014-2019 M.Sc.
- The University of Western Ontario, Medical Biophysics
London, Ontario, Canada
2021-2023 M.Sc.
- Honours and Awards:** Western Graduate Scholarship (WGRS)
2021-2023
- Study Abroad Scholarship Program of the Ministry of National Education
Master's Programme
2020-2023
- Related Work Experience** Project Engineer in Master's Degree Project
Bilkent University, UNAM
Ankara, Turkey
2016-2017
- Publications:**
- Kunduraci, Sule Karagulleoglu,** and Mamadou Diop. "Sensitivity of cerebral blood flow and oxygenation to high-intracranial pressure." *Optical Tomography and Spectroscopy of Tissue XV*. Vol. 12376. SPIE, 2023.
- Conference Publications:**
- Kunduraci, Sule Karagulleoglu,** and Mamadou Diop. "Sensitivity of cerebral blood flow and oxygenation to high-intracranial pressure." *SPIE Photonics West 2023*. Oral Presentation. San Francisco, USA.
- Kunduraci, Sule Karagulleoglu,** and Mamadou Diop. "Sensitivity of cerebral blood flow and oxygenation to high-intracranial pressure." *Neuroscience Research Day 2023*. Oral Presentation. London, Canada.

Kunduraci, Sule Karagulleoglu, and Mamadou Diop. "Sensitivity of cerebral blood flow and oxygenation to high-intracranial pressure." Imaging Network of Ontario 2023. Poster and Pitch Presentation. London, Canada.

Kunduraci, Sule Karagulleoglu, and Mamadou Diop. "Sensitivity of cerebral blood flow and oxygenation to high-intracranial pressure." London Imaging Discover Day 2023. Oral Presentation. London, Canada.

Kunduraci, Sule Karagulleoglu, Utku Yildirim, and Bora Mavis. " Setting of CaSO₄ Based Bone Cements in the Presence of Eggshell Membrane Protein." 20th International Metallurgy & Materials Congress 2021. Virtual